



TECHNICAL REPORT 3034
September 2016

**Wireless Power Control
for Tactical MANET:
Power-Rate Bounds**

Sarah Lauff
Jeffery C. Allen
David F. Schwartz

Approved for public release.

SSC Pacific
San Diego, CA 92152-5001

SSC Pacific
San Diego, California 92152-5001

K. J. Rothenhaus, CAPT, USN
Commanding Officer

C. A. Keeney
Executive Director

ADMINISTRATIVE INFORMATION

The work described in this report was performed by the Applied Electromagnetics Branch (Code 52250 and the Advanced Photonic Technologies Branch (Code 55360), Space and Naval Warfare Systems Center Pacific (SSC Pacific), San Diego, CA. Funding for this effort was provided by the SSC Pacific Naval Innovative Science and Engineering (NISE) Program (Applied Research).

Released by
R. Lu, Head
Advanced Photonic Technologies
Branch

Under authority of
C. Hendrickson, Head
Enterprise Communications
and Networks Division

This is a work of the United States Government and therefore is not copyrighted. This work may be copies and disseminated without restriction.

The citations of trade names and names of manufacturers in this document is not to be construed as official government endorsement of or approval of commercial products or services reference in this report.

MATLAB[®] is a registered trademark of The MathWorks.

EXECUTIVE SUMMARY

This report documents work performed in 2015 and 2016 under Space and Naval Warfare System Center's (SSC Pacific) Naval Innovative Science and Engineering (NISE) Program supporting the Office of Naval Research Expeditionary Warfare and Combating Terrorism Department (ONR 30) in its *Tactical Networking and Small Unit Technologies Thrust Area*.

This project quantifies performance of *wireless power control algorithms* optimizing a mobile network in a ground-based, small-unit operation sweeping through urban environments. The wireless network consists of 20 nodes or less: most nodes are battery limited, most operate at the street level, most are human mobile, a few nodes operate on rooftops, one or two nodes may be a drone supporting relay and video, urban operations guarantee the network will fragment. These wireless networks must adapt to the changing RF environment to meet the following conflicting objectives:

- Maximizing throughput
- Minimizing power
- Guarantee quality of service (QoS).

Performance of these mobile wireless is limited by their *self interference*: increasing power in one link boosts throughput in that link while simultaneously raising interference and decreasing throughput in the other links. Consequently, Wireless Power Control (WPC) is a fundamental control mode enabling mobile networks to trade power, throughput, and QoS [37], [13], [49], [72]. There are other control modes: Dynamic Spectral Access (DSA) manages the power-rate trade-offs by adaptively selecting a best channel [54], and pattern steering selects antenna patterns maximizing power-rate performance [16]. Joint optimization over combinations of these modes is possible: power and channel, or power and patterns. However, all these adaptive controllers must operate over a *distributed* network—centralized control is impractical for small-unit operations. The proposed controllers must also be compatible with legacy radios. Consequently, power-rate controllers are limited to software algorithms and control modes must be enabled by existing radios or by bolt-on hardware. Therefore, *distributed* WPC algorithms are the starting point of this project. Assessment of several distributed WPC algorithms operating in a credible tactical scenario is undertaken with two objectives:

WPC-1 Best performance bounds

WPC-2 Ranking WPC algorithms.

Best performance is the power-rate performance delivered by the perfect and centralized WPC controller. Our findings are that the distributed WPC algorithms use roughly the same power as the ideal WPC and still deliver at half the throughput—assuming system delay is small—increasing system delay causes these distributed WPC algorithms to become unstable. Indeed, “all adaptive algorithms can be broken” if the input measurements exceed the tracking rate of the algorithm. Our key finding is that a *time-delay compensation* scheme stabilizes these WPC algorithms. We conjecture this time-delay compensation is necessary for controllers that jointly optimize power with other control modes and is the basis for the next phase of research.

CONTENTS

EXECUTIVE SUMMARY	iii
1. WHY WIRELESS POWER CONTROL?	1
1.1 MESSAGING AND LATENCY.....	2
1.2 TACTICAL SCENARIOS.....	3
1.3 POWER-RATE TRADE-OFFS.....	3
1.4 EVOLUTION OF WIRELESS POWER CONTROL FOR MOBILE NETWORKS.....	4
1.5 PITFALLS OF ADAPTIVE ALGORITHMS	6
1.6 ORGANIZATION.....	7
1.7 NOTATION.....	9
2. THE NARROWBAND NETWORK MODEL	10
2.1 POWER FLOWS IN THE NETWORK.....	10
2.2 NOISE POWERS AT THE RECEIVER.....	12
2.3 SINR AND THROUGHPUT	14
2.4 CDMA CODING GAIN AND THROUGHPUT	14
3. RF PROPAGATION IN URBAN SCENARIOS	16
3.1 URBAN PROPAGATION AT 300 MHZ	20
3.2 URBAN PROPAGATION AT 1.9 GHZ.....	23
3.3 URBAN PROPAGATION AT 2.4 GHZ.....	30
4. INTERLUDE: TRADE-OFFS AND PARETO POINTS	31
5. POWER-RATE TRADE-OFFS	35
6. INTERLUDE: MATRIX INEQUALITIES	41
7. POWER-RATE TRADE-OFFS IN STATIC CHANNEL.....	43
8. POWER-RATE BASELINES FOR MOBILE TWO-LINK SCENARIOS	51
8.1 MOBILE TRACK AT 300 MHz: FIXED POWER.....	52
8.2 MOBILE TRACK AT 300 MHz: CODING GAIN	55
8.1 MOBILE TRACK AT 300 MHz: BEST PERFORMANCE	57
8.2 MOBILE TRACK AT 1.9 GHz	58
9. THE FOSCHINI AND MILJANIC (FM) ALGORITHM	62
9.1 FM TRACK PERFORMANCE AT 1.9 GHz	63
9.2 FM PERFORMANCE AGAINST DELAY	66
10. THE MODPC ALGORITHM	67
10.1 MODPC TRACK PERFORMANCE AT 1.9 GHz.....	68
10.2 MODPC PERFORMANCE AGAINST DELAY.....	70
11. INTERLUDE: KALMAN FILTER.....	71

11.1 KALMAN FILTER MODELS.....	71
11.2 CHANNEL GAIN AND INTERFERENCE	71
12. H^2 ALGORITHMS.....	73
12.1 H^2 -DPC MOBILE PERFORMANCE AT 1.9 GHz.....	76
12.2 H^2 -DPC PERFORMANCE AGAINST DELAY	78
12.3 ADAPTIVE H^2 -DPC.....	78
13. THE FM-TD ALGORITHMS	82
14. DELAY AND STABILITY	85
15. EXTENDING WIRELESS POWER CONTROL.....	90
15.1 NON-IDEAL MEASUREMENTS.....	90
15.2 CROSS-LAYER OPTIMIZATION	91
15.3 BANDWIDTH.....	91
REFERENCES.....	93
APPENDIX A: PROOF OF THE PARETO FRONT THEOREM.....	A-1

Figures

1. Transmission and interference in a two-link wireless network.	1
2. Wireless power controllers.....	2
3. Power-rate image for a two-link wireless network meeting QoS.....	4
4. Two-link network schematic.....	10
5. Power flows into the receiver: $p_{T,RF}$ transmitted signal power arriving at the antenna; $p_{N,RF}$ environmental RF noise power; $p_{I,RF}$ interference RF power; $p_{N,LO}$ internal or local noise power.	12
6. Sky temperatures T_{eq} (Kelvins) generated by background noise sources [39, page 74]....	12
7. Noise spectral density of the 10-MHz band centered at 300 MHz.	13
8. Urban propagation environment.	16
9. Top view of the two-link network.	17
10. Edge diffraction [56, Figure 2].	18
11. Top view of the 300-MHz channel from transmitter TX-1.....	20
12. Rooftop transmitter in an urban propagation environment (transmitter's height exag- gerated for clarity).	21
13. Rays emanating from the rooftop transmitter down to a street-level receiver.	22
14. Top view of the 300-MHz channel from the rooftop transmitter ($x = 75, y = 50, z = 82$ meters) down to street-level receivers.....	22
15. Top view of the mobile network; TX-2 travels along the x -axis.	23
16. Coverage of TX-2 at $x = 0$ meters.	24
17. Coverage of TX-2 at $x = 50$ meters.	24
18. Coverage of TX-2 at $x = 100$ meters.	25
19. Coverage of TX-2 at $x = 150$ meters.	25
20. Gain matrix at 1.9 GHz for the two-link mobile wireless network.....	26
21. Spatial correlation of $h_{22}(x)$ on $-20 < x < 100$ (m).	28
22. Spatial correlation of $\tilde{h}_{22}(x)$ on $150 < x$ (m).	28
23. Goodness-of-Fit for $ h_{22}(x) ^2$ on $-20 < x < 100$ (m).	29
24. Goodness-of-Fit for $ \tilde{h}_{22}(x) ^2$ on $150 < x$ (m).	29
25. Gain matrix at 2.4 GHz for the two-link mobile wireless network.....	30
26. Vertex of a cone.	31
27. A minimal element.	32
28. Pareto optimal point for the mapping $\mathbf{h} : X \subseteq \mathbb{R}^M \rightarrow \mathbb{R}^2$	32
29. Pareto front of the mapping $\mathbf{h} : X \subseteq \mathbb{R}^M \rightarrow \mathbb{R}^2$	33
30. Power-rate image for a two-link wireless network meeting QoS with the quadrant marking a Pareto point.	34
31. Two-link schematic of a generic distributed wireless power control system.....	35
32. Power control timing with the update issued at the “downbeat” of each frame.....	36
33. Two-link network performance image; the heavy green line is the Pareto front.....	38
34. Two-link network performance image with QoS. The upper green line is the Pareto front.	40
35. External constraints: SINR (left panel), throughput (right panel).....	45
36. Pre-image of the cone of feasible power vectors: $\mathbf{p}_K \in \mathbb{R}_+^2$ (left panel). Cone of feasi- ble power vectors: $\mathbf{p}_C = \mathbf{p}_{\min} + (I - F)^{-1}\mathbf{p}_K$; The grid is distorted by the dB scaling (right panel).	46
37. Network performance image; urban noise at 300 MHz is $p_N = -116$ dBW; the green dot is $\Re(\mathbf{p}_{\min})$. The heavy green line is the Pareto front.....	46

38. Network performance image; noise power $p_N = -80$ dB; the green dot is $\Re(\mathbf{p}_{\min})$. The Pareto front is the upper green line.....	48
39. Network performance image at 300 MHz with 10-dB coding gain; urban noise is $p_N = -116$ dB. The Pareto front is the upper green line.....	49
40. Network performance image at 300 MHz with 10-dB coding gain; noise power is -80 dB. The Pareto front is the upper green line.....	49
41. Network performance image at 300-MHz with 10-dB coding gain; noise power is -116 dB; the QoS is reduced to $\gamma_X = -5$ dB or $R_X = 0.396$ Mbps. The Pareto front is the upper green line.	50
42. Top view of Rosslyn, VA, showing Link 1 (TX-1 to RX-1) and Link 2 (TX-2 to RX-2); TX-2 travels along the x -axis track.	51
43. Gain matrix for moving TX-2 traveling along the x axis.	52
44. SINR for moving TX-2 traveling along the x -axis.....	53
45. Throughput for moving TX-2 traveling along the x axis.	54
46. SINR for moving TX-2 traveling along the x axis; 10-dB coding gain.	55
47. Throughput for moving TX-2 traveling along the x axis; Rosslyn at 300 MHz; 10-dB coding gain.	56
48. Throughput for moving TX-2 traveling along the x axis; 10-dB coding gain; QoS ≥ 25 kbps. The “blanks” in the plot mark where QoS failed.	57
49. Gain matrix for moving TX-2 traveling along the x axis; Rosslyn at 1.9 GHz.....	58
50. SINR for moving TX-2 traveling along the x axis; Rosslyn at 1.9 GHz; coding gain $g_C = 10$ dB; equal power $p_{T,1} = p_{T,2} = 1$ watt.....	59
51. Equal-power throughput for moving TX-2 traveling along the x axis; Rosslyn at 1.9 GHz; coding gain $g_C = 10$ dB; equal power $p_{T,1} = p_{T,2} = 1$ watt.....	60
52. Throughput for moving TX-2 traveling along the x axis; Rosslyn at 1.9 GHz; coding gain $g_C = 10$ dB; QoS $\geq R_{b,X} = 1$ Mbps. The “blanks” in the plot mark where QoS failed.	61
53. FM performance for mobile TX-2 traveling along the x axis; $R_{b,X} = 1$ Mbps; delay $\tau = 0.9$ ms; frame duration $t_F = 1$ ms; $f_C = 1.9$ GHz; Coding gain $g_C = 10$ dB. Upper Panel: Link power along the track; Lower Panel: Link rates along the track.	64
54. FM performance averaged over x -axis track; QoS $R_{b,X} = 1$ Mbps; delay $\tau = 0.9$ ms; frame rate $t_F = 1$ ms; $f_C = 1.9$ GHz; coding gain $g_C = 10$ dB.....	65
55. Average FM performance along x -axis track as a function of delay; $R_{b,X} = 1$ Mbps; frame rate $t_F = 1$ ms; $f_C = 1.9$ GHz; coding gain $g_C = 10$ dB.....	66
56. MODPC performance for mobile TX-2 traveling along the x axis; $R_{b,X} = 1$ Mbps; delay $\tau = 0.9$ ms; frame duration $t_F = 1$ ms; $f_C = 1.9$ GHz; coding gain $g_C = 10$ dB. Upper Panel: Link power along the track; Lower Panel: Link rates along the track.	68
57. MODPC performance averaged over x -axis track; QoS $R_{b,X} = 1$ Mbps; delay $\tau = 0.9$ ms; frame duration $t_F = 1$ ms; $f_C = 1.9$ GHz; coding gain $g_C = 10$ dB.....	69
58. Average MODPC performance along x -axis track as a function of delay; $R_{b,X} = 1$ Mbps; frame duration $t_F = 1$ ms; $f_C = 1.9$ GHz; coding gain $g_C = 10$ dB.....	70
59. Kalman feedback for QoS power control.	75
60. \mathcal{H}^2 -DPC performance along x -axis track; $R_{b,X} = 1$ Mbps; frame duration $t_F = 1$ ms; $f_C = 1.9$ GHz; coding gain $g_C = 10$ dB. Upper Panel: power on each link; Lower Panel: throughput on each link.	76
61. Average \mathcal{H}^2 -DPC performance along x -axis track with delay $\tau = 0.9$ ms; $R_{b,X} = 1$ Mbps; frame duration $t_F = 1$ ms; $f_C = 1.9$ GHz; coding gain $g_C = 10$ dB.....	77

62. Average \mathcal{H}^2 -DPC power-rate performance along x -axis track subjected to delays; $R_{b,X} = 1$ Mbps; frame duration $t_F = 1$ ms; $f_C = 1.9$ GHz; coding gain $g_C = 10$ dB.	79
63. Average A- \mathcal{H}^2 -DPC performance along x -axis track: $\tau = 0.9$ ms.	80
64. Average A- \mathcal{H}^2 -DPC performance along x -axis track: $\tau = 9$ ms.	81
65. Power allocation for the A- \mathcal{H}^2 -DPC along x -axis track: $\tau = 9$ ms.	81
66. Average FM-TD performance along x -axis track subjected to delays; QoS $R_{b,X} = 1$ Mbps; frame duration $t_F = 1$ ms; $f_C = 1.9$ GHz; coding gain $g_C = 10$ dB; delay is known: $\tau = \tau_F$	84
67. Average FM-TD performance along x -axis track subjected to delays; QoS $R_{b,X} = 1$ Mbps; frame duration $t_F = 1$ ms; $f_C = 1.9$ GHz; coding gain $g_C = 10$ dB; delay is approximate: $\tau_F \approx \tau$	84
68. Spectral radius of the feedback matrix x -axis track; QoS $R_{b,X} = 1$ Mbps; $f_C = 1.9$ GHz; coding gain $g_C = 10$ dB.	86
69. FM algorithm convergence along x -axis track; QoS $R_{b,X} = 1$ Mbps; $f_C = 1.9$ GHz; coding gain $g_C = 10$ dB; “blanks” mark where $\rho(F(x)) > 1$	86
70. FM algorithm against delay $\tau = 10$ ms along the x -axis track; QoS $R_{b,X} = 1$ Mbps; $f_C = 1.9$ GHz; coding gain $g_C = 10$ dB.	87
71. Single link model.	88
72. Stability of the recursion for the single-link system; maximum of roots of $z^{k+1} - z^k + (1 - \beta) = 0$	89
73. (Left) Gain matrix at 1.9 GHz. (Right) SINR at 1.9 GHz.	91

Tables

1. Selected distributed wireless power control algorithms.	6
2. Network functions.	9
3. RF functions and parameters.	9
4. Acronyms.	9
5. Urban and suburban noise levels (dBW) for selected bandwidths f_B and carrier frequencies f_C	13
6. Second-order diffraction terms.	18
7. Diffraction terms for the urban simulation.	19
8. Urban dielectrics.	19
9. Spatial correlation distance: 1.9 GHz.	27
10. Selected single-objective power control formulations.	40
11. RF and system parameters.	63
12. FM parameters.	63
13. MODPC parameters.	68
14. \mathcal{H}^2 -DPC Parameters.	76
15. Spatial correlation and convergence along the x -axis track; Transmitter TX-2 traveling at $v = 4$ m/s; frame duration $t_F = 1$ ms.	87

1. WHY WIRELESS POWER CONTROL?

Figure 1 illustrates throughput and interference conflicts in a wireless network. Link 1 boosts throughput by increasing broadcast power—thereby boosting interference on Link 2. Link 2 increases its broadcast power to overcome this interference—thereby boosting interference on Link 1. The network’s self-jamming and uncontrolled feedback forces the nodes into a power race that ends with all nodes blasting at full power. More formally [25]: “Wireless networks are fundamentally limited by the intensity of the received signals and by their inherent interference.”

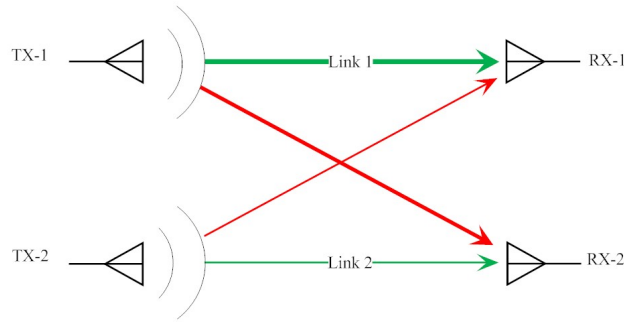


Figure 1. Transmission and interference in a two-link wireless network.

Wireless power control seeks to manage the conflict between throughput and interference while delivering optimal trade-offs between standard network objectives [41]:

- Maximize throughput
- Minimize power
- Guarantee quality of service (QoS).

The payoff from wireless power control is substantial. Douros & Polyzos observe the following [18]:

- “... power control nearly doubles the capacity of a CDMA system [26]”
- “For Mobile Ad Hoc NETWORKS (MANETS), the adoption of power control leads to an over 50% improvement to the energy expended compared to the standard IEEE 802.11 [60]”
- “[62] estimates the signal-to-interference plus noise ratio (SINR) gains from the adaption of power control exceed 10 dB”

This report seeks side-by-side comparisons of distributed wireless power control algorithms operating in tactical scenarios of interest to the Office of Naval Research (ONR). The scenarios are the mobile, ad hoc networks supporting small-unit ground forces operating in urban and rural environment (Section 1.2). These comparisons are the trade-offs between power and throughput under QoS constraints. The payoffs for ONR are an “apples-to-apples” ranking of these algorithms accompanied by best possible trade-offs (Section 1.3).

Best possible trade-offs between power and throughput are computable under the assumptions that a *centralized* controller exists with the following capabilities:

- Instantaneous and perfect measurements of the noise and interference at each receiver
- Instantaneous and perfect control of each transmitter
- Homogeneous network traffic.

The best bounds benchmark the effectiveness of wireless power control algorithms to compensate the time-varying mobile channels. The ad-hoc nature of mobile wireless networks means that mobile nodes may drop out, the wireless channels are subject to fast and slow fading, the signal-to-interference and noise ratios (SINR) can only be estimated at each node, and the network traffic is not homogeneous. Thus, wireless power control algorithms must maximize throughput and minimize energy while operating from noisy, time-delayed measurements, noisy, time-delayed power control messages, and time-varying network traffic demands.

1.1 MESSAGING AND LATENCY

Wireless power control requires messaging for power control. Figure 2 compares *centralized* against *distributed* messaging for a two-link wireless network. Centralized control requires that receivers broadcast their estimated quality of service to a central node. The central node computes an optimal power-rate trade-off for the entire network and broadcasts the new power commands to the transmitters. Centralized control is not practical for mobile wireless networks [13]: “the implementation of a centralized solution is not plausible in practice due to the signaling overhead and high computational complexity.” Distributed control is the focus of this report and only requires the feedback from the receiver to its transmitter.

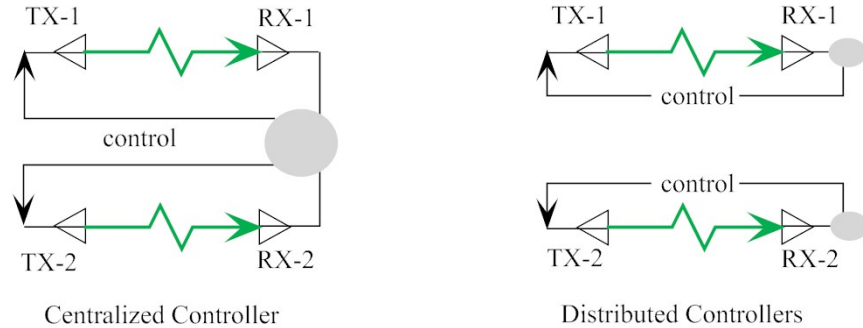


Figure 2. Wireless power controllers.

Upper and lower bounds on distributed power control are determined by maximal centralized and local control. Maximal centralized control is equivalent to all-knowing network “genie” having access to perfect measurements and instantaneously selects best possible power-rate trade-offs. Local control typically assigns transmit power *before* the deployment and thereby provides a lower bound on power-rate trade-offs. Distributed algorithms must outperform local control to justify the additional overhead. Those distributed algorithms that come close the centralized control are the candidates for development.

1.2 TACTICAL SCENARIOS

“Tactical” is in the title of this report. Tactical mobile wireless networks serving small-unit ground forces operate with different requirements than commercial systems:

- Radios are single transceivers
- Hardware upgrades are unlikely
- Frequencies differ from commercial systems
- Avoiding detection may force extreme noise levels
- Battery power is always a problem
- Jamming will be intelligent and hostile
- Nodes routinely drop out
- Messaging priorities vary
- Throughput requirements are increasing
- Centralized control is impractical.

These limitations point to software-only solutions operating on the existing radio hardware. Assessing performance of these algorithms in tactical RF scenarios is a basic task to quantify their performance. Power and throughput are basic tactical network performance metrics. Well-designed wireless control algorithms lead to optimal power-rate trade-offs [37]. Best possible bounds on the power-rate trade-offs in tactical RF scenarios provide absolute benchmarks to rank system performance and guide development in these challenging RF scenarios.

1.3 POWER-RATE TRADE-OFFS

The geometry of the power-rate image shows best possible trade-offs between throughput and power that any wireless power control algorithm can deliver in a given tactical RF scenario. These optimal power-rate trade-offs are computed for a two-link tactical scenario to benchmark distributed wireless power control algorithms operating with delayed and noisy measurements.

Figure 3 shows the power-rate image for a two-link wireless network operating over a noisy narrow-band channel at 300 MHz subject to QoS constraints. This image shows all possible power and rates that an “all-knowing” network genie delivers while meeting QoS. Here, “all-knowing” means the genie has perfect channel measurements and implements power control without delays. The genie sets the powers p_1 and p_2 for the two-link wireless network to meet the QoS. The QoS constraint requires the throughputs on both links to exceed a minimum:

$$R_{b,1}, R_{b,2} \geq 1.58 \text{ [Mbps]}.$$

Equivalently, the SINR both links must exceed 3 dB. The horizontal axis is the total network power: $p_\Sigma = p_1 + p_2$. The vertical axis is total network throughput: $R_\Sigma = R_{b,1} + R_{b,2}$. Section 7 details the explicit parameterization of this image.

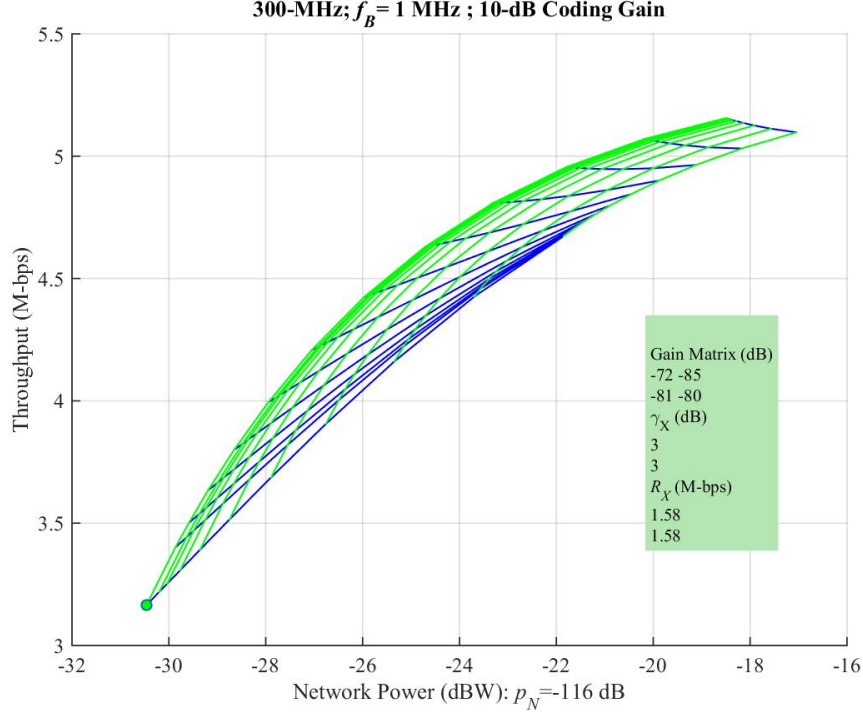


Figure 3. Power-rate image for a two-link wireless network meeting QoS.

Vertical and horizontal “slices” of the power-rate image correspond to power-allocation modes. If the total network power is fixed, the network genie seeks to maximize total network throughput. Equivalently, the optimal power allocation is the top of a vertical “slice” of the power-rate image. If the total network throughput is fixed, the network genie seeks to minimize the total network power. Equivalently, the optimal power allocation is the left end-point of horizontal “slice” of the power-rate image. This geometric approach is not in the wireless literature—to the best of our knowledge [75], [79]. Computation of this Pareto front supplies the best bound on any wireless power-control algorithm.

1.4 EVOLUTION OF WIRELESS POWER CONTROL FOR MOBILE NETWORKS

The literature on wireless power control is extensive: surveys from the last two decades include [32], [53], [66], [41], [11]. This section discusses wireless power control algorithms applicable to the mobile, ad hoc networks used by small-unit ground forces operating in urban and rural environments. The emphasis is on distributed algorithms operating in the physical layer—there is no centralized controller, joint power control and scheduling [54], joint power control and channel selection [54], cross-layer optimization [42], [6], cognitive radios [38], or cognitive networking [80].

The seminal wireless power control algorithm was authored in 1993 by Gerad J. Foschini and Zoran Miljanic [22]: *A Simple Distributed Autonomous Power Control Algorithm and its Convergence*. The Foschini & Miljanic (FM) algorithm updates the power $p_l(t)$ on each link ($l = 1, \dots, L$) so that the measured SINR $\gamma_{M,l}(t)$ tracks the external SINR $\gamma_{X,l}$ set by networking requirements:

$$\bar{p}_l(t_{n+1}) = \bar{p}_l(t_n) + \overbrace{(1 - \beta)}^{\text{stepsize}} (\bar{\gamma}_{X,l} - \bar{\gamma}_{M,l}(t_n)) .$$

The overline is the standard dB notation

$$\bar{p}(t) = 10 \times \log_{10}(p(t)).$$

The FM algorithm seeks to deliver a target QoS during communication along each link. Descendants of this algorithm are listed in the first line of Table 1. One highlight is a multiobjective version of the FM algorithm that trades power against QoS [20]. All wireless power control algorithms suffer from the following:

- Noisy measurements in both the SINR and in the control systems
- Feasibility—there may be no power allocation delivering the requested QoS
- Time delays in both the measurements and the control systems.

Noisy Measurements: Idealized systems provide instantaneous measurements of the SINR. Practical systems typically measure the only received signal power—the sum of the signal power, the interference and the noise—to make indirect estimates the SINR. Shoarinejad, Speyerm, and Pottie [68] produced an excellent paper showing how Kalman filtering delivers improved predictions of SINR. This report assumes ideal SINR measurements.

Feasibility: One solution to the feasibility problem are the *Opportunistic Power Control* algorithms that adapt the QoS to a range rather than a fixed number [12]: When the channel does support a QoS, the QoS can be increased; when the channel does not support the QoS, the QoS is decreased. Such Kalman filtering algorithms update the power $p_l(t)$ on each link so that the improved SINR measurement $\hat{\gamma}_{M,l}(t)$ tracks the time-varying “target” SINR $\gamma_{T,l}(t)$:

$$\bar{p}_l(t_{n+1}) = \bar{p}_l(t_n) + (1 - \beta) \left(\bar{\gamma}_{T,l}(t_n) - \bar{\gamma}_{M,l}(t_n) \right).$$

Selected Kalman filtering schemes are listed in the second line of Table 1. Limitations of the Kalman filter are observed in [84]:

- “... power control schemes using the Kalman filter are effective only if the ... channel variation and measurement noise are Gaussian distributed.”
- “Traditional power control schemes using power iterations ... are not appropriate to compensate Rayleigh channel fading because all the schemes require a long time to converge.”

The H^2 , H^∞ , and H^2/H^∞ algorithms drop the Gaussian assumption by assuming channel variations and measurement noises are bounded. Selected H^∞ algorithms are listed in the third line of Table 1.

Time Delay: All adaptive algorithms will fail if the updates arrive too slowly to compensate for the changes in the system. Informally, the measurements are “stale” or that the time delays are not spanned by the system models. The significant time delay in wireless power control are caused by the signal processing and messaging—not in the over-the-air travel time. Figure 31 details that the receiver must measure the power, estimate the SINR, undertake a control computation, message the power control command back to the transmitter, the transmitter must receive the message, extract the power command, and reset the power. This process consumes several milliseconds. Such delays will cause the wireless power control algorithms to fail depending on the channel correlation and the update times. Campos-Delgado & Luna-Rivera observe [7]:

“Therefore, the main challenge in distributed power control is to compensate the time-varying profiles of the channel gains and interactions among all active users to achieve the objective SINR’s and to counteract the effect of time delays induced by the QoS measurements.”

One approach to accommodate time delays in the Kalman, H^2 , and the H^∞ filters is to expand the state vector [48], [45], [48]. Another approach, similar to the PID controller [2], models the time delay itself without increasing the dimension of the state vector—the paper by Subramanian and Sayed is a masterful exposition of this approach [73].

Gunnarsson, Guustafsson, and Blom produced a superb analysis of time-delay (TD) effects and offer an effective *time-delay compensation* of the FM algorithm that takes the form [29]:

$$\bar{p}_l(t_{n+1}) = \bar{p}_l(t_n) + (1 - \beta) (\bar{\gamma}_{X,l} - \bar{\gamma}_{M,l}(t_n)),$$

where $\bar{\gamma}_{M,l}(t_n)$ is an estimate of the delayed SINR. Table 1 lists this FM-TD algorithm in the fourth line along with other references specializing Smith control, H^∞ control, and Kalman filtering to time-delay compensation.

Table 1. Selected distributed wireless power control algorithms.

1990–1999	2000–2010	2011–2015	Algorithm
[22], [82], [23], [83]	[20], [1], [12] [36], [68], [70], [72] [48], [84] [29], [64], [72], [48], [2]	[81] [40] [13], [49], [34] [31]	FM Kalman H^2/H^∞ Delay compensation

1.5 PITFALLS OF ADAPTIVE ALGORITHMS

If multiple transmitters are updating broadcast power based on noisy and delayed signals adapting to time-varying channels—where the time variation is determined by the speed of the mobile network—network-level questions arise regarding the algorithm performance with respect to

- Stability
- Donvergence
- Latency effects
- Measurement errors and control errors.

The point is that every adaptive algorithm can be broken—either the time-variations of the channel exceed the scope of the control algorithm or the measurements are too corrupted by noise.

This report assumes perfect measurements and controls to focus algorithm performance when adapting to the urban channels and system delays exceeding the update rate. The selected algorithms show relatively similar performance at moderate system delays but fail upon exceeding a delay threshold. The payoff of this report is the introduction of a time-delay compensation scheme that extends the FM algorithm to handle larger delays.

1.6 ORGANIZATION

Section 2 lays out the signal, interference, and noise models for a narrowband wireless network. The upshot is that a wireless power control is governed by the channel gain matrices, the noise level, and the system delays.

Section 3 describes the RF propagation in a three-dimensional urban environment. The gain matrices rule the mobile wireless network performance. The simulated channels exhibit *slow fading* caused by building-size shadowing and *fast fading* caused by multipath interference [68] at 300 MHz, 1.9 GHz, and 2.4 GHz.

Section 5 describes a wireless power control *system* and its consequent model of network performance. This model of a wireless power control system is the common operational framework for the forthcoming distributed wireless power control algorithms. This common operational framework permits comparisons without getting entangled in system-specific implementations.

Section 6 reviews selected results in matrix inequalities. Section 7 uses these matrix inequalities to compute power allocations for a static channel. Equivalently, this section describes the power-rate image shown in Figure 3.

Section 8 describes the simplest possible mobile network: two links with only one mobile node that travels along the x -axis track. This network determines baseline scenarios. The simplest possible power control simply assigns constant power to both transmitters. The best possible power control assumes an all-knowing network “genie” capability of perfect measurements and instantaneous control. Good power control algorithms will have performance closing in on the best possible power control but must outperform the simplest power control. The mobile links were baselined at 300 MHz, 1.9 GHz, and 2.4 GHz. The frequency band at 1.9 GHz was selected to test the algorithms. The associated bandwidth of 1.3 MHz implies the wireless link operate with a frame duration of one millisecond. This frame rate is the update rate used for all the wireless power algorithms. That is, each wireless power control algorithm travels along the same mobile track, updates power every millisecond, measures the same noise power, is given perfect interference measurements, and is subject to the same system delays. These constraints enable side-by-side comparisons of the algorithms.

Section 9 applies the fundamental Foschini and Miljanic (FM) algorithm [22] to the mobile network at 1.9 GHz using a 1.3-MHz bandwidth. Each link $l = 1, \dots, L$ updates its power control command as

$$p_{C,l}(t_{n+1}) = p_{C,l}(t_n) \left(\frac{\gamma_X}{\gamma_{M,l}(t_n)} \right)^{1-\beta}.$$

The power updates by the ratio of the requested SINR γ_X to the measured SINR $\gamma_M(t_n)$. If the FM algorithm converges ($\gamma_M(t_n) \rightarrow \gamma_X$), the power settles to a steady state ($p_{C,l}(t_n) \rightarrow \text{constant}$). The convergence rate is controlled by the stepsize β . The FM algorithm handles delays out to 8 frames as the mobile network traveled along its x -axis track. In comparison to the best possible performance delivered by the network “genie,” the FM algorithm requires roughly the same power but suffers a 50% reduction in throughput. This loss of throughput is the “cost-of-business” associated with a distributed algorithm versus the idealized centralized controller. However, the FM algorithm breaks down when delay exceed 8 frames. Increasing delays cause power to increase and throughput to decrease.

Section 10 applies Multiple Objective Distributed Power Control Algorithm (MODPC) of Elumrati, Jäntti, and Koivo [20] to this mobile simulation. The MODPC algorithms seeks a trade-off between the

two objectives of power consumption and QoS. The MODPC power control is [20, Equation 7]

$$p_{C,l}(t_{n+1}) = p_{C,l}(t_n) \frac{\lambda_P p_{\min} + \lambda_Q \gamma_X}{\lambda_P p_{C,l}(t_n) + \lambda_Q \gamma_{M,l}(t_n)}; \quad \lambda_P, \lambda_Q \geq 0; \lambda_P + \lambda_Q = 1,$$

where the $\lambda_P \approx 1$ weights the trade-off for power savings while $\lambda_Q \approx 1$ seeks QoS. This solution contains the FM algorithm for $\lambda_P = 0$. The MODPC algorithm, even when weighted for QoS, still only handles delays out to 8 frames. When delays exceed 8 frames, the MODPC algorithm breaks down like the FM algorithm—power increases while throughput drops to zero.

Section 11 reviews the Kalman filter as a special case of the H^2 algorithms. Section 12 assesses two H^2 algorithms along the same mobile network. Average power-rate performance is simulated for the mobile network at moderate delays. Both H^2 algorithms breakdown when system delay exceeds 8 frames.

The preceding sections show the limitations of the FM algorithm, Kalman filtering, and the H^∞ algorithms that model time delay as a noise source or external disturbance. Section 13 applies a *time-delay compensation* scheme to produce a simple extension of the FM algorithm. The key idea is to record the power history and estimate the “stale” power with an approximation from the past. This simple extension allows the FM algorithm to handle delays out to 20 frames.

Section 14 analyzes the effect of the delay on the FM algorithm. Even in the simplest network, consisting of exactly one link, system delays cause instabilities. Stepsize selection enforces stability but only handles a limited range of delays and also reduces the adaptive speed of the FM algorithm. Thus, the significance of the time-delay compensation scheme is the stabilization of the FM algorithm without reducing its adaptive speed.

Section 15 assesses the simulations. The side-by-side comparison of these distributed wireless power control algorithms operating in a tactical RF environment reveal similar performance across all algorithms: near-optimal performance at moderate delays but a breakdown at longer delays, time-delay compensation stabilizes the FM algorithm. There are several points-of-departure based these findings.

Section 15.1 points out that the wireless power control algorithms operated using ideal measurements and synchronized updates. Therefore, assessments should encompass non-ideal limited measurements available from current radios and asynchronous updates.

Section 15.2 points out that wireless power control algorithms only controlled power. Performance will be enhanced by optimizing power with other control modes: beamforming, channel selection, scheduling, and routing. The payoff from these extra control “knobs” may be substantial but exacerbates system delay and instability. The mobile wireless simulations can assess both the performance and the stability under the assumption of perfect cross-layer communication. If the proposed algorithms deliver significant performance shifts over the power-only control, consideration of the messaging complexity is the next step to assess the feasibility of these other control modes.

Section 15.3 points out that the wireless power control algorithms operated over a narrowband channel. Section 15.3 presents a 20-MHz channel centered at 1.9 GHz from the mobile simulations. This channel is frequency selective. Although the preceding wireless power control algorithms can operate over such channels, the current approaches point to an OFDM-CDMA waveform to handle this channel. Regardless of the waveform, the wideband mobile wireless simulations can compare performance and the stability of both the narrowband algorithms against the OFDM-CDMA approaches under ideal measurements. If the OFDM-CDMA approaches algorithms deliver significant performance shifts over the narrowband algorithms, robustness of the OFDM-CDMA approaches is the next step for assessment.

1.7 NOTATION

The real and complex numbers are denoted by \mathbb{R} and \mathbb{C} , respectively. Likewise, the corresponding L -dimensional vector spaces are denoted \mathbb{R}^L and \mathbb{C}^L , respectively. The *transpose* of $\mathbf{x} \in \mathbb{R}^L$ is

$$\mathbf{x}^T = [x_1, \dots, x_L].$$

The *Hermitian* of $\mathbf{x} \in \mathbb{C}^L$ is

$$\mathbf{x}^H = [\bar{x}_1, \dots, \bar{x}_L],$$

where the overline denotes the complex conjugate. A matrix $A \in \mathbb{R}^{M \times N}$ then A is said to have size $M \times N$.

Table 2. Network functions.

Notation	Description
$\mathbf{p}_T(t)$	Transmitted power vector (W)
$\mathbf{p}_R(t)$	Received power vector (W)
$\mathbf{p}_N(t)$	Noise power vector (W)
$\mathbf{p}_I(t)$	Interference power vector (W)
$\mathbf{p}_C(t)$	Control power vector (W)
$\gamma_M(t)$	Measured SINR vector
$\gamma_X(t)$	External SINR vector
$R_X(t)$	External throughput vector
$\Delta t_U(t)$	Uplink delay (m-sec)
$\Delta t_D(t)$	Downlink delay (m-sec)

Table 3. RF functions and parameters.

Notation	Description
f_C	Carrier frequency (MHz)
f_B	Bandwidth (MHz)
G	Channel gain matrix
G_S	Channel signal matrix: $G_S = \text{diag}(G)$
G_I	Channel interference matrix: $G_I = G - G_S$
R_b	Bit rate (bps)
$\mathbf{s}_T(t)$	Transmitted signal vector (V)
$\mathbf{s}_R(t)$	Received signal vector (V)
t_F	Frame duration (ms)

Table 4. Acronyms.

	Description
BPSK	Binary Phase-Shift Keying
CDMA	Code Division Multiple Access
TDMA	Time Division Multiple Access
SINR	Signal-to-Noise and Interference Ratio

2. THE NARROWBAND NETWORK MODEL

This section presents the signal, interference, and noise models for a narrowband wireless network. The gain matrix models the signal power and the network's self-interference. The noise power is set by the external RF noise. The networks's signal-to-interference and noise ratio (SINR) determines an upper bound on the throughput. Thus, the network performance, as measured by the power and rate, are determined by the gain matrix and the noise.

2.1 POWER FLOWS IN THE NETWORK

Figure 4 is a schematic of a two-link network. Each transmitter is assigned a designated receiver defined by the link (green lines). All links share the same frequency band and all broadcast at the same time. These simultaneous broadcasts constitute the interference (red lines) exacerbating the additive in-band noise also impinging upon each receiver. For a general network, let the links be indexed $l = 1, \dots, L$.

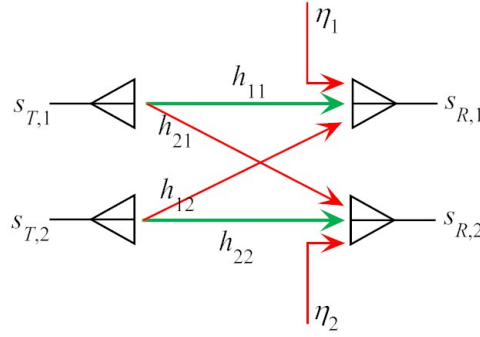


Figure 4. Two-link network schematic.

Assume the receivers intercept the transmitter's signals according to the following *narrowband model*:

$$\begin{bmatrix} s_{R,1}(t) \\ \vdots \\ s_{R,L}(t) \end{bmatrix} = \begin{bmatrix} h_{11}(t) & h_{12}(t) & \dots & h_{1L}(t) \\ h_{21}(t) & h_{22}(t) & \dots & h_{2L}(t) \\ \vdots & \vdots & \ddots & \vdots \\ h_{L1}(t) & h_{L2}(t) & \dots & h_{LL}(t) \end{bmatrix} \begin{bmatrix} s_{T,1}(t) \\ \vdots \\ s_{T,L}(t) \end{bmatrix} + \begin{bmatrix} \eta_1(t) \\ \vdots \\ \eta_L(t) \end{bmatrix}.$$

In the notation of Table 3, the *channel matrix* $H(t)$ links the transmitted signal vector to the received signal vector:

$$\mathbf{s}_R(t) = H(t)\mathbf{s}_T(t) + \boldsymbol{\eta}(t). \quad (1)$$

Signal power and interference power are computed from Equation (1). The received power is

$$\begin{aligned} p_{R,l}(t) &= E[|s_{R,l}(t)|^2] \\ &= E \left[\sum_{m=1}^L \sum_{m'=1}^L \overline{h_{lm}(t)s_{T,m}(t)} h_{lm'}(t)s_{T,m'}(t) \right] \\ &\quad + E \left[\sum_{m=1}^L 2\Re \left(\overline{h_{lm}(t)s_{T,m}(t)} \eta_l(t) \right) \right] + E[|\eta_l(t)|^2]. \end{aligned}$$

Assume the channel is independent of the signals and the noise. Assume the noise is independent of the signals and is zero mean. Then the cross terms vanish and the received power simplifies as

$$p_{R,l}(t) = \sum_{m=1}^L \sum_{m'=1}^L E [\overline{h_{lm}(t)} h_{lm'}(t)] E [\overline{s_{T,m}(t)} s_{T,m'}(t)] + p_{N,l}(t).$$

If the signals are uncorrelated, their cross terms vanish and the received power exposes the signal, interference, and noise as follows:

$$\begin{aligned} p_{R,l}(t) &= \sum_{m=1}^L E [|h_{lm}(t)|^2] E [|s_{T,m}(t)|^2] + p_{N,l}(t) \\ &= \sum_{m=1}^L g_{lm}(t) p_{T,m}(t) + p_{N,l}(t) \\ &= \underbrace{g_{ll}(t) p_{T,l}(t)}_{\text{signal}} + \underbrace{\sum_{m \neq l} g_{lm}(t) p_{T,m}(t)}_{\text{interference}} + \underbrace{p_{N,l}(t)}_{\text{noise}}. \end{aligned} \quad (2)$$

Consequently, the network performance is governed by *gain matrix* G and the noise level:

$$\mathbf{p}_R(t) = \begin{bmatrix} p_{R,1}(t) \\ \vdots \\ p_{R,L}(t) \end{bmatrix} = \begin{bmatrix} g_{11}(t) & \dots & g_{1L}(t) \\ \vdots & \ddots & \vdots \\ g_{L1}(t) & \dots & g_{LL}(t) \end{bmatrix} \begin{bmatrix} p_{T,1}(t) \\ \vdots \\ p_{T,L}(t) \end{bmatrix} + \begin{bmatrix} p_{N,1}(t) \\ \vdots \\ p_{N,L}(t) \end{bmatrix} = G(t) \mathbf{p}_T(t) + \mathbf{p}_N(t). \quad (3)$$

Equation (3) is the basis for the wireless power control algorithms. This equation is based on the following assumptions:

Assumptions 1 *Narrowband Network Model*

NB-1 Links transmit simultaneously in the same frequency band (no TDMA)

NB-2 Link assignments do not change (no handoffs)

NB-3 Channels are narrowband (multiplicative gain matrix)

NB-4 Channels are independent of the signals

NB-5 Channels are independent of the additive link noise

NB-6 Noise is zero mean, Gaussian, and spectrally flat

NB-7 Noise is uncorrelated with the signals

NB-8 Signals are uncorrelated between the links

NB-9 Signals “occupy” the entire band with approximately flat spectra.

These assumptions do not include the time delays associated with the measurements and signal processing necessary to support the wireless power control systems. The generalization of Equation (3) to include time delays is discussed in Section 5. The signal power, the interference power, and the noise power determine the SINR. The SINR sets an upper bound on link capacity and is reviewed in Section 2.3. The noise is modeled in the next subsection.

2.2 NOISE POWERS AT THE RECEIVER

The noise level in the receiver should be set at the detector of the receiver. A standard noise model at the input of the detector assumes the noise is the sum of the external RF noise observed through the receiver and the receiver's internal noise. Figure 5 illustrates the power flows arriving at the receiver's antenna and into its detector. The RF signal, the external RF noise, and the interference all travel through the receiver's RF chain. This report assumes the external RF noise dominates the receiver's noise. Therefore, the external SINR at the antenna input is the same as the SINR at the input to the detector.

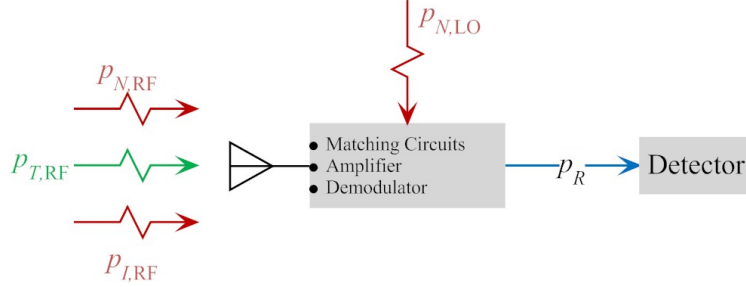


Figure 5. Power flows into the receiver: $p_{T,RF}$ transmitted signal power arriving at the antenna; $p_{N,RF}$ environmental RF noise power; $p_{I,RF}$ interference RF power; $p_{N,LO}$ internal or local noise power.

The external RF noise is modeled as zero-mean, complex-valued Gaussian with flat spectrum across the frequency band (see NB-6). As such, only the variance or, equivalently, in-band power level $p_{N,RF}$, is required to model this Gaussian noise. This noise level is modeled as [39, page 76]

$$p_{N,RF} = \kappa_B T_{eq} f_B, \quad (4)$$

where Boltzmann's constant is $\kappa_B = 1.38 \times 10^{-23} \text{ (W} \cdot \text{K}^{-1} \cdot \text{Hz}^{-1})$, T_{eq} is the effective operating temperature (K), and f_B is the bandwidth (Hz). Figure 6 plots T_{eq} as a function of frequency for selected RF noise sources. Equation (4) models the narrowband noise or, equivalently, assumes a flat spectrum.

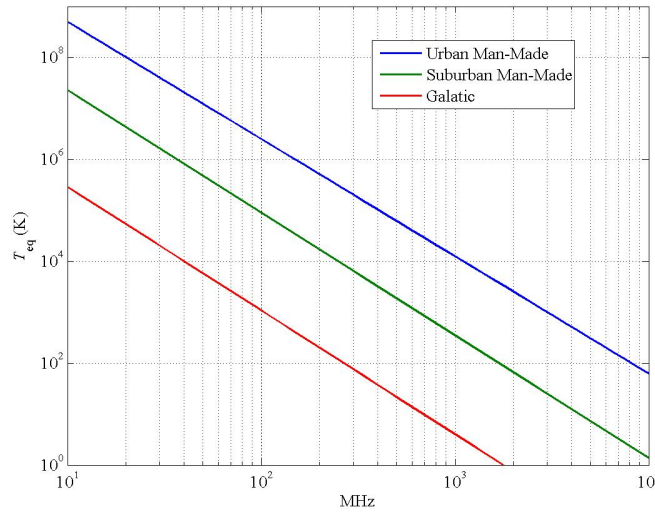


Figure 6. Sky temperatures T_{eq} (Kelvins) generated by background noise sources [39, page 74].

Wideband noise is modeled by integrating the noise spectral density [39, page 76]:

$$\rho_N(f) = \kappa_B T_{\text{eq}}(f) \quad [\text{watts} \cdot \text{Hz}^{-1}]$$

over the frequency band

$$p_N = \int_{f_C - f_B/2}^{f_C + f_B/2} \rho_N(f) df \quad [\text{dBW}].$$

Figure 7 plots the urban noise spectral density centered at $f_C = 300$ MHz over the frequency band $f_B = 10$ MHz. The plot shows near-constant noise density generates in-band noise power of $p_N \approx -106$ [dBW]. Therefore, the flat-spectrum of Assumption NB-6 is credible for relative bandwidths

$$\frac{f_B}{f_C} = \frac{10}{300} \approx 3\%.$$

For convenience, the noise levels used in the forthcoming network simulations are listed in Table 5.

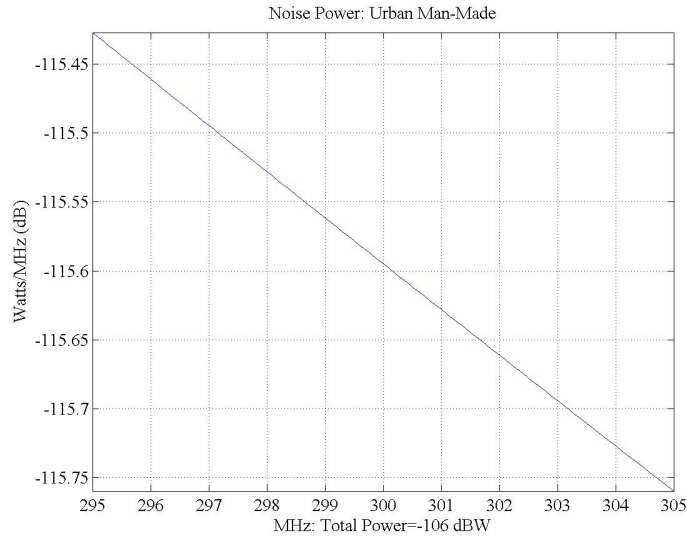


Figure 7. Noise spectral density of the 10-MHz band centered at 300 MHz.

Table 5. Urban and suburban noise levels (dBW) for selected bandwidths f_B and carrier frequencies f_C .

Frequency	Bandwidth	Urban Power	Suburban Power
300 MHz	25 kHz	-132	-147
300 MHz	1 MHz	-116	-131
300 MHz	10 MHz	-106	-121
1.9 GHz	1.3 MHz	-133	-149
1.9 GHz	10 MHz	-124	-140
2.4 GHz	10 MHz	-126	-142
2.4 GHz	20 MHz	-123	-139

2.3 SINR AND THROUGHPUT

Assumptions 1 model the received power on the l -th link by Equation (2) and repeated here for convenience:

$$p_{R,l}(t) = \overbrace{g_{ll}(t)p_{T,l}(t)}^{\text{signal}} + \sum_{m \neq l} \overbrace{g_{lm}(t)p_{T,m}(t)}^{\text{interference}} + \overbrace{p_{N,l}(t)}^{\text{noise}}.$$

Definition 1 (SINR) *Under Assumptions 1, the signal-to-interference-and-noise ratio (SINR) measured on the l -th link is*

$$\gamma_{M,l}(t) := \frac{g_{ll}(t)p_{T,l}(t)}{p_{N,l}(t) + \sum_{m \neq l} g_{lm}(t)p_{T,m}(t)}.$$

The *signal-to-interference-and-noise ratio* (SINR) governs the throughput for specific waveforms and also the maximum capacity or Shannon capacity that a link can support. This report uses the Shannon capacity to bound best possible performance shifts that wireless power control algorithms deliver rather than getting entangled with specific waveforms, detection schemes, estimation issues, and hardware limitations. The Shannon capacity for a single link that is ruled by the signal-to-noise ratio (SNR) [27, Equation 4.1]

$$R_b = f_B \log_2(1 + \text{SNR}),$$

provided the noise is zero-mean, flat spectrum, Gaussian that is uncorrelated with the signal. If the interfering signals “look like” this flat-spectrum Gaussian noise and are also uncorrelated with the link’s signal, the capacity generalizes from the SNR to the SINR.

Definition 2 (Narrowband Throughput) *Under Assumptions 1, the throughput on the l -th link is the Shannon capacity integrated across the common bandwidth*

$$R_{b,l}(t) := f_B \log_2(1 + \gamma_{M,l}(t)).$$

Thus, the network performance—power and throughput—is ruled by the gain matrix $G(t)$ and the noise power $\mathbf{p}_N(t)$. The diagonal of the gain matrix determines the signal power. The off-diagonal terms of the gain matrix determine the interference. Networks using Code-Division Multiple Access (CDMA) suppress interference. Roughly speaking, CDMA “coding gain” divides the interference. The next section details this coding gain for use in the wireless simulations.

2.4 CDMA CODING GAIN AND THROUGHPUT

The gain matrix controls the signal and interference. Coding gain suppresses the interference and boosts the SINR and throughput. Code-Division Multiple Access (CDMA) is one approach using signal-processing to boost the SINR [52]: “In a CDMA system, all users transmit information over the same time and frequency, and each user signal is recovered through a particular code sequence.” The received signal on l -th link adapts from [6, Equation 2] as follows:

$$s_{R,l}(\mathbf{p}_T; t) = \sum_{k=1}^L h_{l,k} \sqrt{p_{T,k}} b_k \mathbf{s}_l. \quad (5)$$

Under Assumptions 1, the channel matrix H determines the gain matrix $G = E[|H|^2]$ and includes the physical RF channel, the transmit antenna, the receive antenna, and the processing losses. For Binary Phase-Shift Keying (BPSK), the information bit is $b_k \in \{-1, 1\}$. The symbol vector \mathbf{s}_k typically derives from a pseudo-noise sequence. For example, if the receiver on the l -th link uses a decision vector \mathbf{d}_l , the SINR adapts from [6, Equation 7] as follows:

$$\gamma_l(\mathbf{p}_T) = \frac{g_{ll} \langle \mathbf{d}_l, \mathbf{s}_l \rangle p_{T,l}}{p_{N,l} \|\mathbf{d}_l\|^2 + \sum_{k \neq l} g_{lk} \langle \mathbf{d}_l, \mathbf{s}_k \rangle p_{T,k}}.$$

If $\mathbf{d}_l = \mathbf{s}_l$, the SINR simplifies to

$$\gamma_l(\mathbf{p}_T) = \frac{g_{ll} p_{T,l}}{p_{N,l} + \sum_{k \neq l} g_{lk} \langle \mathbf{s}_l, \mathbf{s}_k \rangle p_{T,k}}.$$

Denote the lower bound

$$g_C := \min\{|\langle \mathbf{s}_l, \mathbf{s}_k \rangle| : k, l \in \{1, \dots, L\}\}.$$

The SINR admits the bound [27, Equation 14.5]:

$$\gamma_l(\mathbf{p}_T) \leq \frac{g_{ll} p_{T,l}}{p_{N,l} + g_C^{-1} \sum_{k \neq l} g_{lk} p_{T,k}}. \quad (6)$$

In terms of the gain matrix

$$G = G_S + G_I; \quad G_S = \begin{bmatrix} g_{11} & 0 & \dots & 0 \\ 0 & g_{22} & \dots & 0 \\ \vdots & \vdots & \ddots & \vdots \\ 0 & 0 & \dots & g_{LL} \end{bmatrix}; \quad G_I = G - G_S,$$

coding gain reduces the interference by changing the gain matrix:

$$G \leftarrow G_S + \frac{1}{g_C} G_I.$$

Simulations that list “coding gain” imply that Equation (6) bounds the SINR.

For the throughput, the capacity equation must be specialized to BPSK-CDMA coding. Assume each network transmits CDMA symbol vectors consisting of N_c chips of duration T_c . The network bandwidth is

$$f_B = \frac{1}{T_c},$$

each symbol vector has duration $T_{\text{sym}} = N_c \times T_c$, and the symbol rate is

$$R_{\text{sym}} = \frac{1}{T_{\text{sym}}} = \frac{1}{N_c \times T_c} = \frac{f_B}{N_c}.$$

The throughput specialized for BPSK-CDMA is adapted from [6, Equation 5]. Each symbol vector carries one information bit by Equation (5):

$$R_b = R_{\text{sym}} \times (1 - \exp(-\gamma_M))^{N_c} = \frac{f_B}{N_c} \times (1 - \exp(-\gamma_M))^{N_c} \quad [\text{bps}]. \quad (7)$$

This adaptation assumes no overhead symbols ($L = 1$) and the standard efficiency function [6]. This BPSK-CDMA throughput is dominated by the standard capacity equation. Therefore, whenever coding gain is invoked, throughput can be computed using the BPSK-CDMA rate of Equation (7) or throughput can be bounded by the standard capacity equation. The simulations that invoke the coding gain bound of shown in Equation (6) also bound the throughput by standard capacity equation—not the BPSK-CDMA rate of Equation (7).

3. RF PROPAGATION IN URBAN SCENARIOS

Figure 8 shows the three-dimensional urban environment where the mobile wireless networks operate. Figure 9 is the top view of a two-link network operating in this urban area. Both transmitters and one receiver are at street level. The second receiver is located on the rooftop 80 meters above the street. The transmitter on Link 2 will travel along the x -axis. The view shows transmitter TX-2 at the origin. This two-link network is the smallest and simplest mobile wireless network simulation. This simulation is the common operating environment to assess the forthcoming wireless power control algorithms.

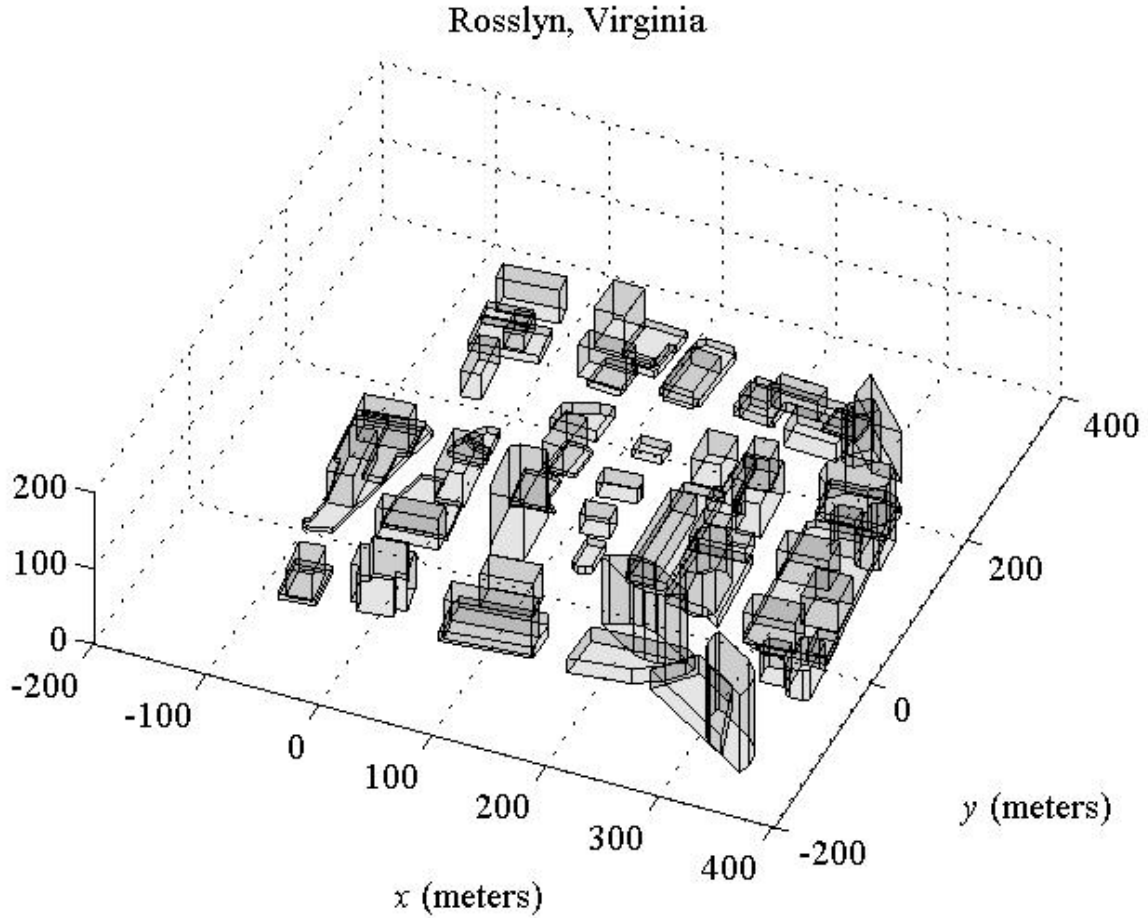


Figure 8. Urban propagation environment.

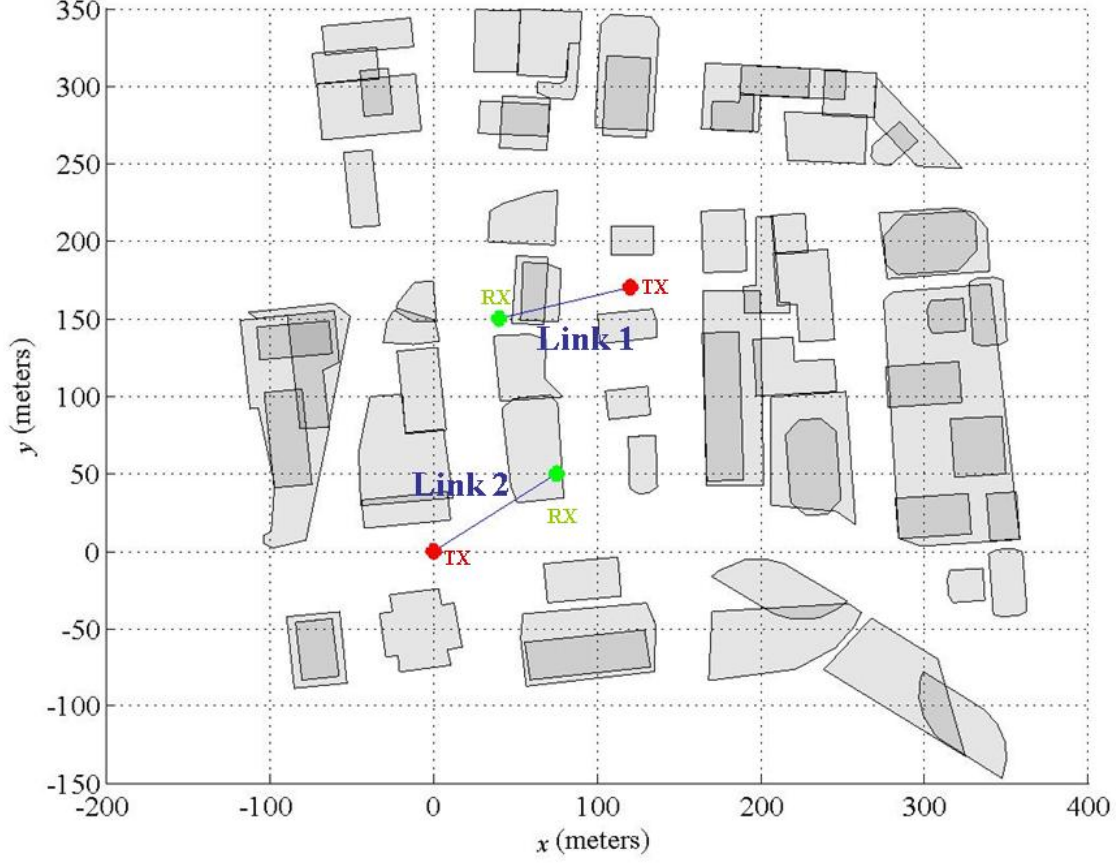


Figure 9. Top view of the two-link network.

RF propagation in this simulated 3-D environment is governed by the wave equation [24, Chapter 3]. Approximate solutions to the wave equation are computed by *Numerical Electromagnetics Code-Basic Scattering Code* (NEC-BSC) [55]. NEC-BSC approximates the electric and magnetic field solutions to the 3-D wave equation by reflection and diffraction models. The approximation for the electric field generated by a source sums the rays' interaction with the 3-D environment to arrive at a position \mathbf{r} :

$$\mathbf{E}(\mathbf{r}) = \mathbf{E}_{\text{inc}} + \sum_{r \in \mathcal{P}(\mathbf{r})} \mathbf{E}^p(\mathbf{q}_r) + \sum_{e \in \mathcal{E}(\mathbf{r})} \mathbf{E}^e(\mathbf{q}_e) + \sum_{v \in \mathcal{V}(\mathbf{r})} \mathbf{E}^v(\mathbf{q}_v) + \text{higher-order terms.}$$

The first term is the incident electric field \mathbf{E}_{inc} produced by the direct path from the source to position \mathbf{r} , provided there is no blockage. The second term sums each electric field generated by the ray traveling from the source, reflecting off a plate at position \mathbf{q}_r , and arriving at position \mathbf{r} . Each plate reflection models the dielectric of the plate and consequent spreading factor after reflection. The third term sums each electric field generated by the ray traveling from the source, diffracting on an edge at position \mathbf{q}_e , and arriving at position \mathbf{r} . Figure 10 shows the diffraction cone geometry for an edge. Each edge diffraction models the dielectric of the edge and consequent spreading factor after diffraction. The edge diffraction terms correct for the discontinuities in the incident and plate reflected fields. The fourth term sums each electric field caused by rays traveling from the source, diffracting at vertex \mathbf{q}_v , and arriving position \mathbf{r} .

Each edge diffraction models the dielectric of the vertex and consequent spreading factor after diffraction. The vertex diffraction terms correct for the discontinuities in the edge-diffracted fields.

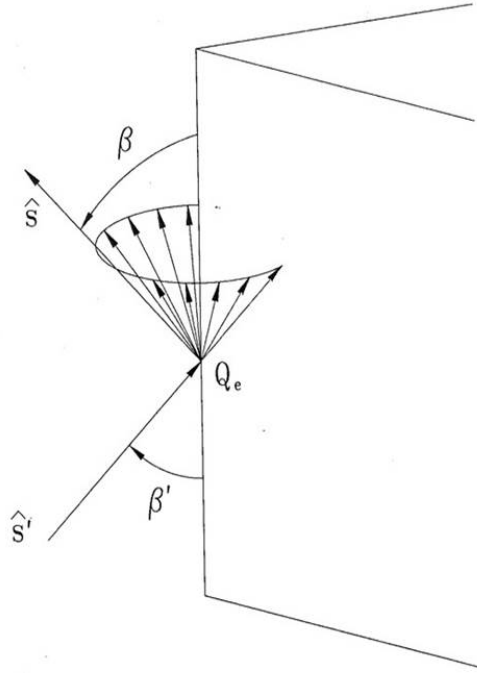


Figure 10. Edge diffraction [56, Figure 2].

NEC-BSC differs from other ray tracing programs by modeling not only the plate reflections but also including the diffraction terms. The diffraction modeling in NEC-BSC, even at the ray level, also differs from other ray tracing programs. Diffraction coefficients are derived from the high-frequency asymptotic solutions of canonical problems. These asymptotic approximations are more accurate as the associated “large parameters” increases. The “large parameters” are generally a function of the distances from the source to the diffraction point and from the diffraction point to the position \mathbf{r} . Multiple interactions between flat faces, edges and vertices are needed for complex environments. Cascading these high-frequency asymptotic solutions determine these higher-order interactions. Complex environments have an infinite number of higher-order interactions. Higher-order terms compensate discontinuities in first-order and other lower-order terms. Table 6 lists the second-order terms.

Table 6. Second-order diffraction terms.

Plate-to-plate	Edge-to-plate	Vertex-to-plate
Plate-to-edge	Edge-to-edge	Vertex-to-edge
Plate-to-vertex	Edge-to-vertex	Vertex-to-vertex

Third-order terms follow a similar pattern (e.g., Plate-to-plate-to-plate, Plate-to-plate-to-edge, ...). A correct application of NEC-BSC requires that the dominant terms in an environment be determined to guarantee accuracy of the solution. Such a convergence study was undertaken to support the propagation in [63]. Table 7 lists the diffraction terms necessary to approximate the electric field to 30-dB accuracy. The dominant terms were limited to plate and edge interactions.

Table 7. Diffraction terms for the urban simulation.

Order	Terms
0	Incident
1	Plate, edge
2	Plate-to-plate, Edge-to-plate, Edge-to-edge

The reflections and diffractions require the dielectrics of the building and the ground. Table 8 describes the modeling. The buildings are modeled with roofs and sides as concrete slabs 0.3 meters thick. Windows, iron reinforcements, or rooftop materials are not modeled. The ground plane is modeled as a half-plane of wet earth. Variations in elevation are not modeled. The wet-earth dielectric was selected to match the modeling in Daly [15]. Wet earth absorbs more RF energy than the asphalt listed for comparison.

Table 8. Urban dielectrics.

	Slab thickness	Relative Permittivity	Conductivity	References
Buildings	0.3 (m)	6.0	0.01	[15]
Wet earth	Half space	25	0.005	[15]
Asphalt	Half space	2.56	0.0011	[65, 4-30]

This simple 3-D urban modeling produces *representative* RF environments. These RF environments model large-scale multipath behaviors rather than absolute levels [63]. As such, these simulations are best employed to reveal *relative* performance shifts between the wireless power control algorithms.

Performance of any wireless power control algorithm is ruled by the gain matrix. Section 3.1 starts the discussion by introducing the channels generated by the Transmitter TX-1 broadcasting at 300 MHz (Figure 9). Section 3.2 shows how the channel plots vary as Transmitter TX-2 travels through the urban environment along the x -axis while broadcasting at 1.9 GHz. The channel plots are then combined to produce the gain matrix for the wireless network generated by the mobile wireless network with TX-2 traveling along the x -axis track. Section 3.3 provides the associated gain matrix at 2.4 GHz. Although the 3-D urban model is simple, the gain matrices show large-scale variations caused by the street geometry (large-scale shadowing) and fine-scale variation (fast fading) caused by the local diffraction effects. Any wireless power control algorithm must adapt to both types of fading.

3.1 URBAN PROPAGATION AT 300 MHZ

Figure 11 is a top view looking down on the street-level propagation produced by transmitter TX-1 broadcasting at 300 MHz or with a wavelength of 1 meter. The color map is the channel gain from TX-1 to street-level receivers produced by a NEC-BSC simulation. Both the transmitter and receiver operate with a half-wavelength vertical dipole. Both the transmitter and receiver are “street level” or that their antennas are placed 2 meters above the ground plane ($z = 2$).

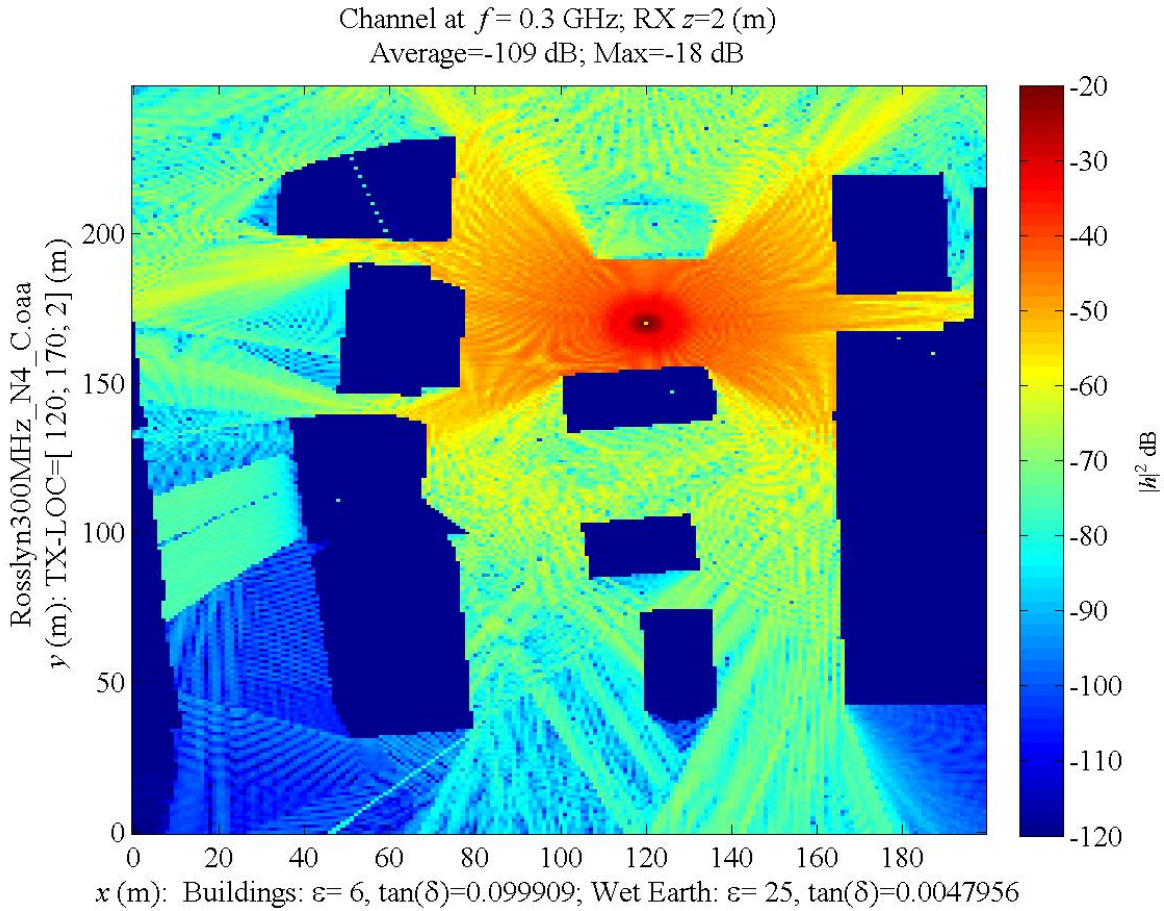


Figure 11. Top view of the 300-MHz channel from transmitter TX-1.

Even in this simple 3-D model, the channel gain shows detailed interference patterns near the transmitter. The plot also shows RF energy diffracting around the buildings and the resulting shadow zones caused by each building. In these low-power shadow zones, the discontinuities caused by using only the second-order model (Table 8) are visible. The low-power fields could be smoothed by adding higher-order terms—incurring a massive computational expense—to approximate the gain down to 50 dB rather than 30 dB.

The next three figures display the effect of placing a transmitter or, equivalently, a receiver to a rooftop. Figure 12 shows the 3-D urban environment with a transmitter on the rooftop that is 80 meters above the street. The transmitter's antenna is 2 meters above the rooftop. Figure 13 shows the rays computed by NEC-BSC that link the rooftop transmitter to a street-level receiver. Close examination shows that most of the ray paths include a diffraction off a building edge.

Figure 14 is a top view looking down on the street-level propagation produced by the rooftop transmitter broadcasting at 300 MHz down to street-level receivers. The transmitter is located at $x = 75$, $y = 50$, and $z = 82$ meters. Both transmitters and receivers employ a half-wavelength vertical dipole. The color map uses a different scale than Figure 11 to better show the relative uniform coverage, or equivalently, the tactical communication advantage that this location offers.

Although the channels in Figure 14 are computed using the rooftop transmitter to a street-level receiver, reciprocity implies this plot also shows the channels from street-level transmitters to the rooftop receiver RX-2 of the two-link network shown in Figure 9. In particular, this simulation models street-level transmitters traveling through this environment whose signal is intercepted by RX-2. The next section examines specific channels along the track followed by TX-2.

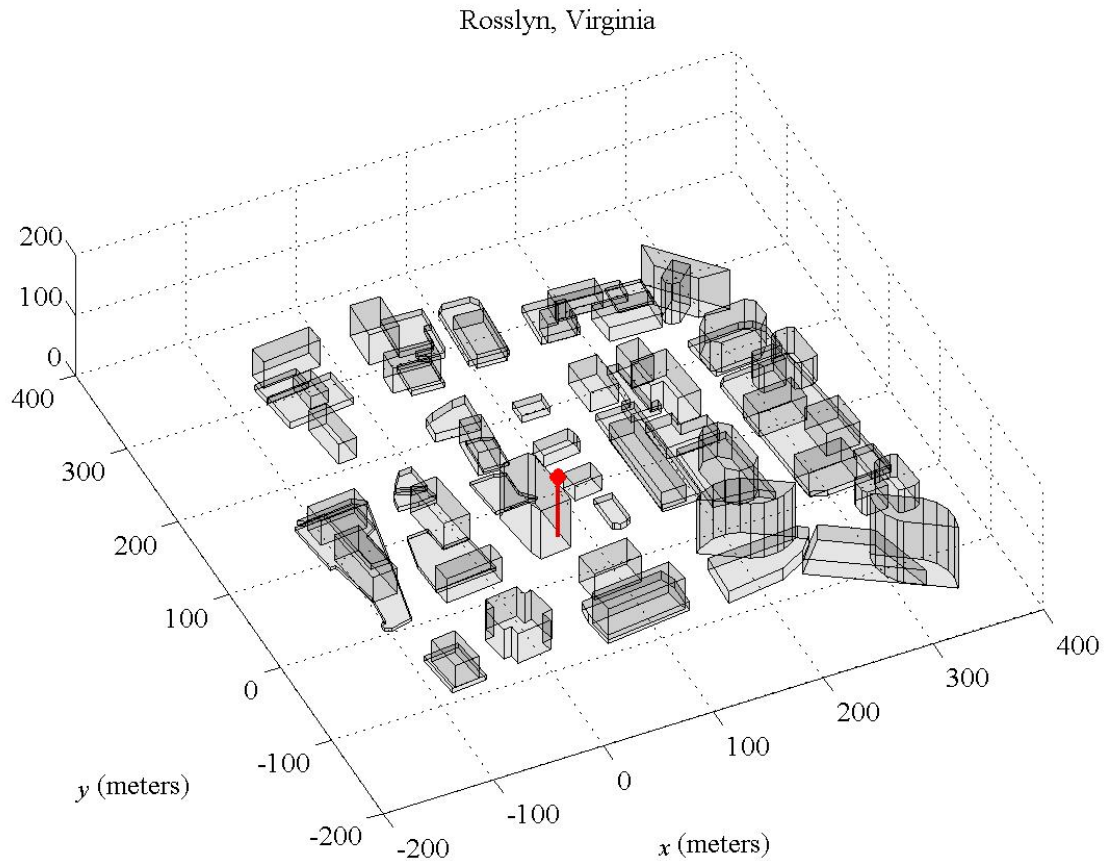


Figure 12. Rooftop transmitter in an urban propagation environment (transmitter's height exaggerated for clarity).

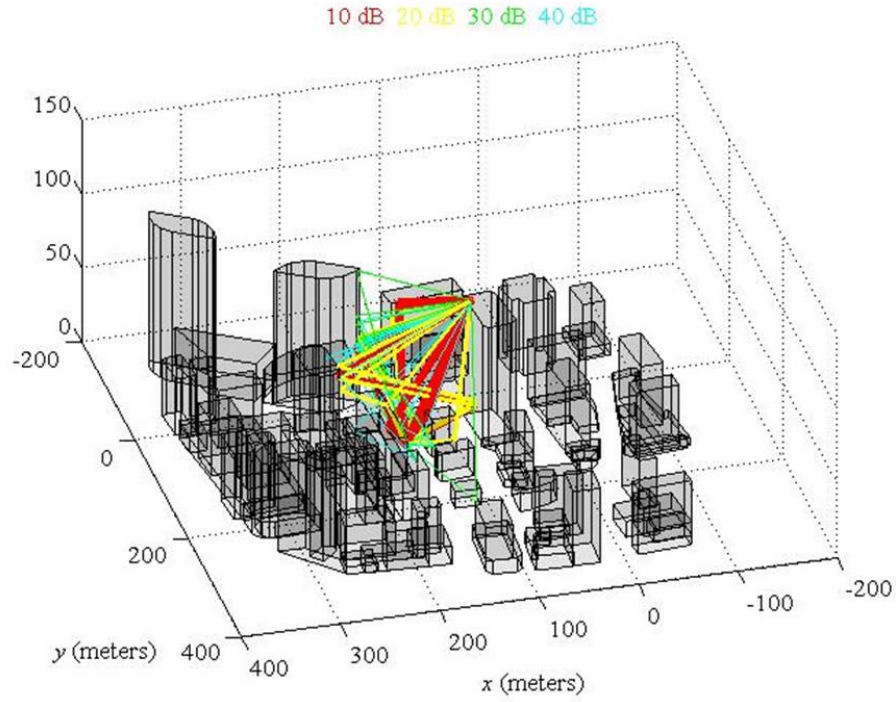


Figure 13. Rays emanating from the rooftop transmitter down to a street-level receiver.

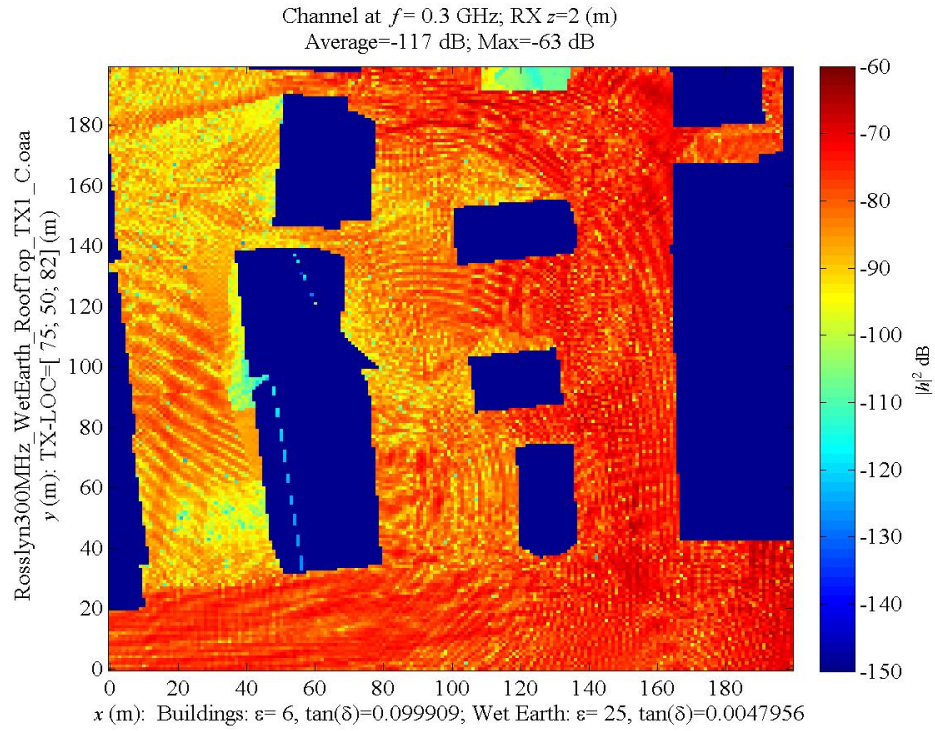


Figure 14. Top view of the 300-MHz channel from the rooftop transmitter ($x = 75$, $y = 50$, $z = 82$ meters) down to street-level receivers.

3.2 URBAN PROPAGATION AT 1.9 GHZ

Figure 15 shows the smallest and simplest possible mobile wireless network consisting of four nodes or two links and only one mobile node. The mobile node carries transmitter TX-2 along the x -axis track. All nodes employ half-wavelength vertical dipole antennas.

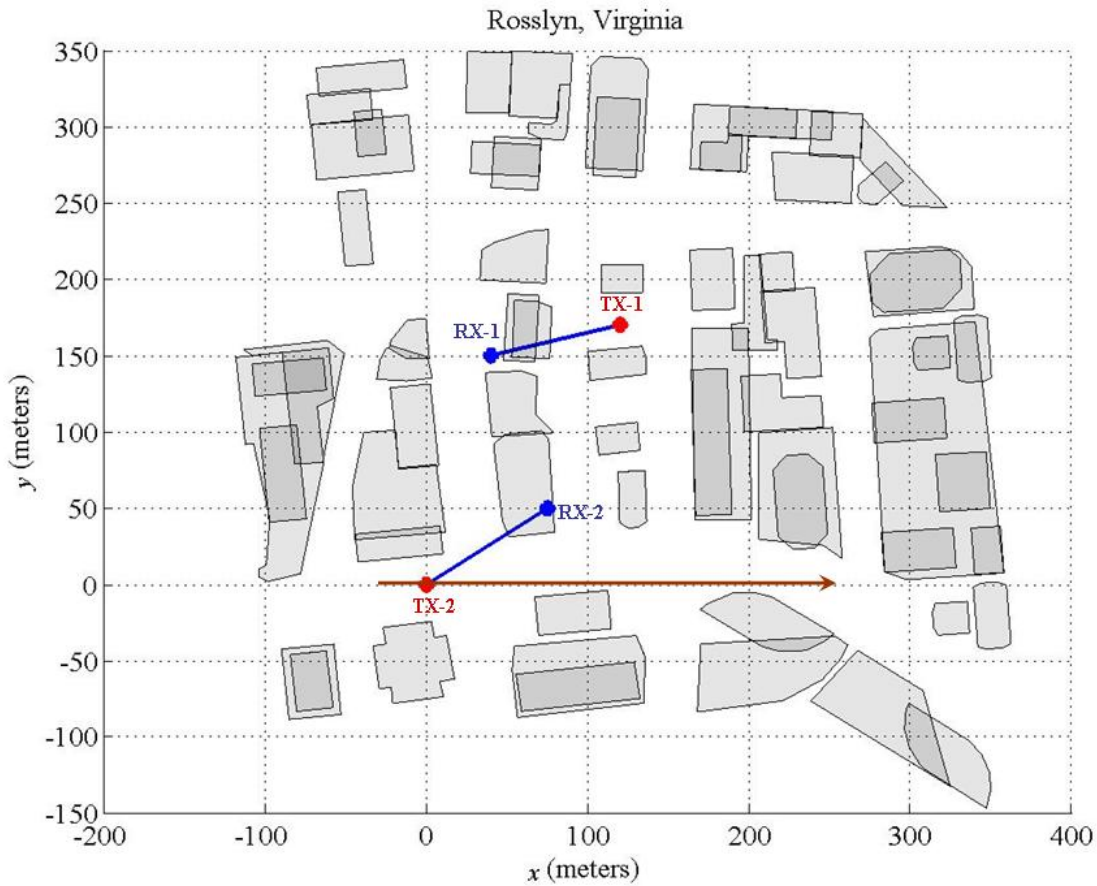


Figure 15. Top view of the mobile network; TX-2 travels along the x -axis.

The next four plots show the channel generated by TX-2 at selected locations along its x -axis track: $x = 0, 50, 100$, and 150 meters. The plots show the power radiating from TX-2 flowing through the city up to second-term accuracy. Consequently, the high-gain regions are a better approximation to the gain than the low-gain regions in the narrow side streets.

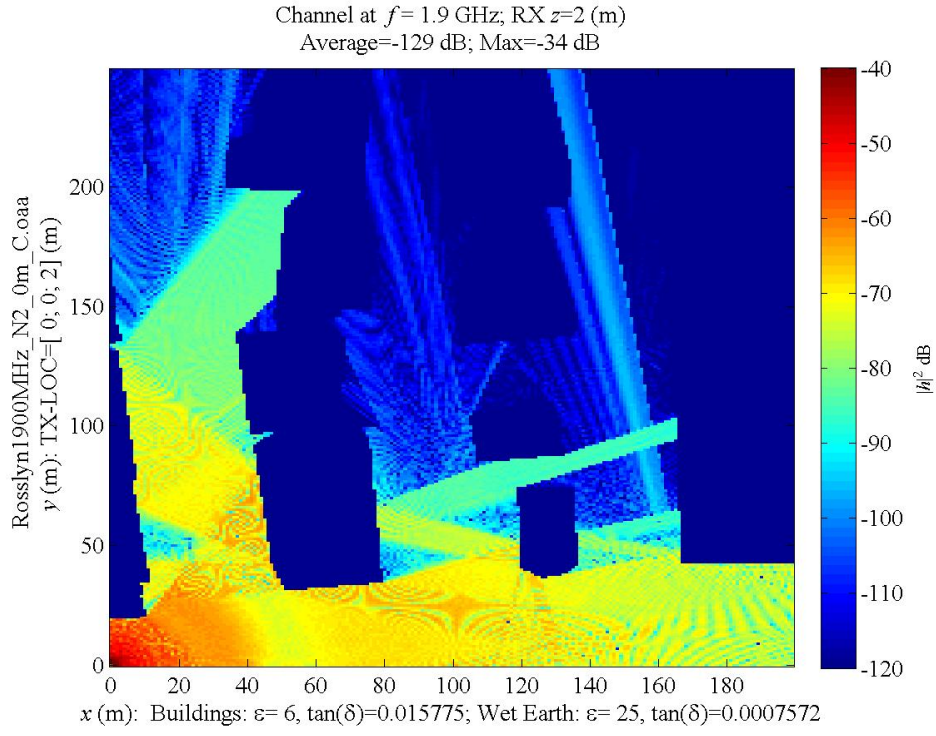


Figure 16. Coverage of TX-2 at $x = 0$ meters.

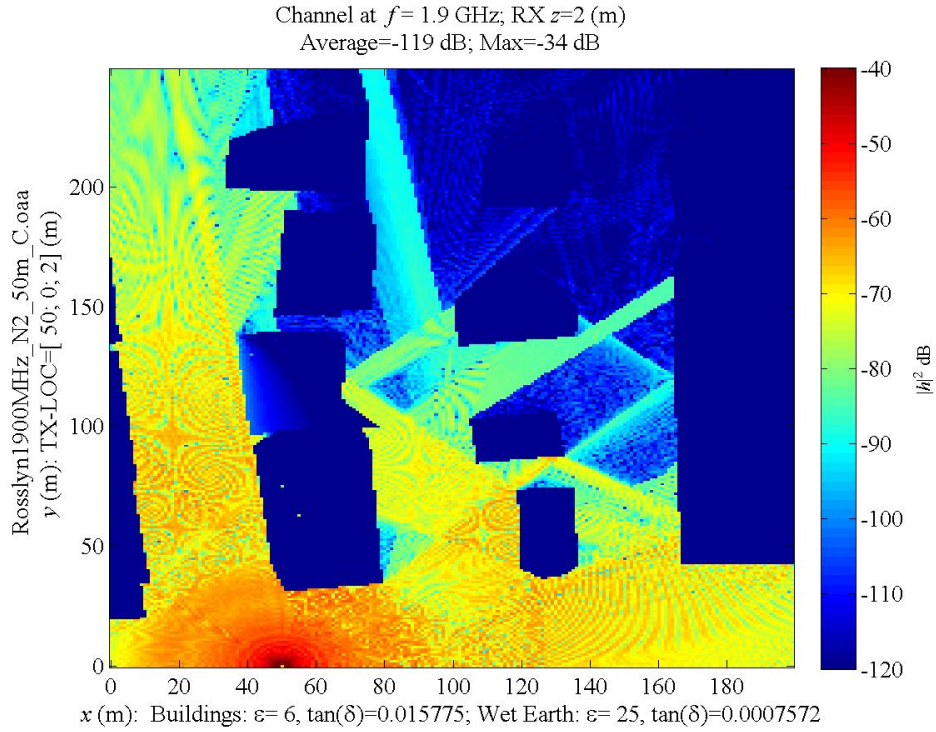


Figure 17. Coverage of TX-2 at $x = 50$ meters.

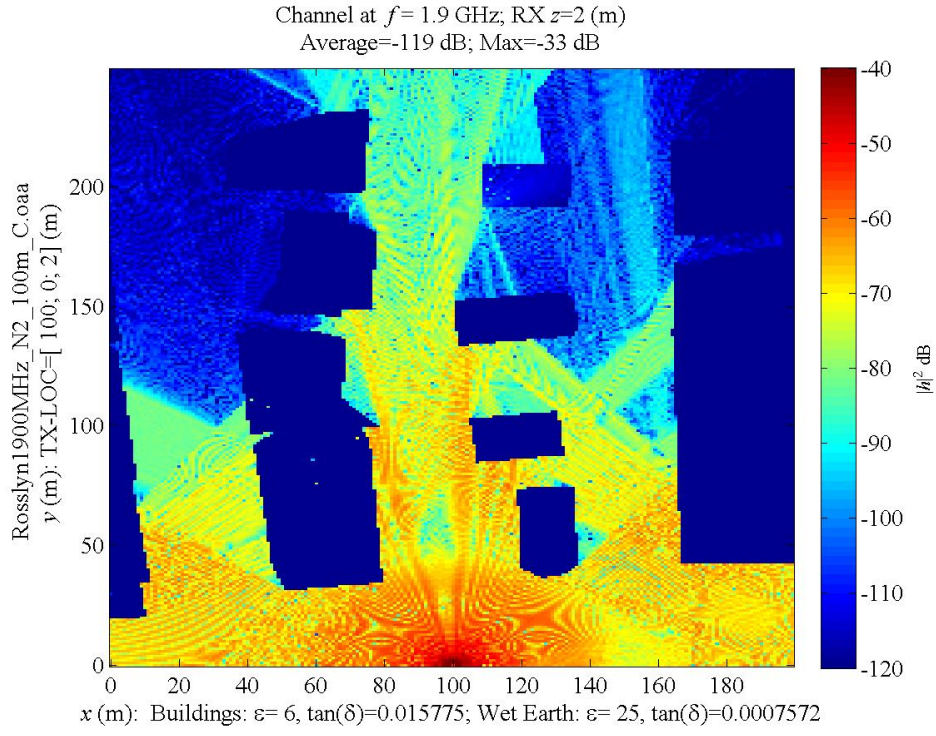


Figure 18. Coverage of TX-2 at $x = 100$ meters.

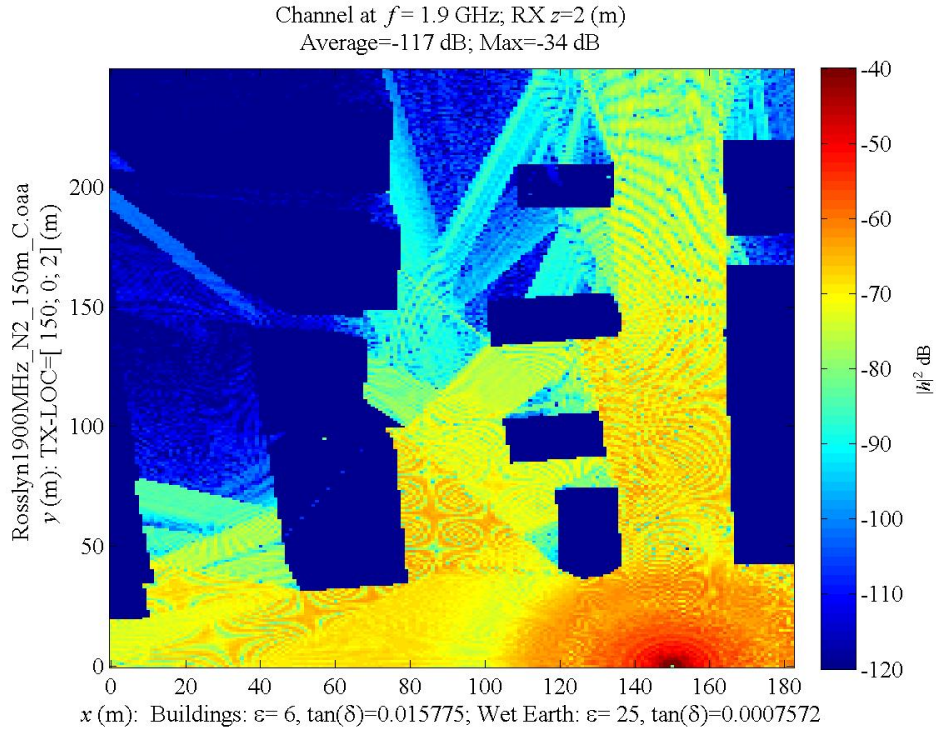


Figure 19. Coverage of TX-2 at $x = 150$ meters.

If the channels of this two-link mobile network are collected as TX-2 travels along the x axis, the resulting gain matrix has the form

$$G(x) = \begin{matrix} & \text{TX-1} & \text{TX-2} \\ \begin{matrix} \text{RX-1} \\ \text{RX-2} \end{matrix} & \begin{bmatrix} g_{11} & g_{12}(x) \\ g_{21} & g_{22}(x) \end{bmatrix} \end{matrix} = \begin{bmatrix} -102 & g_{12}(x) \\ -93 & g_{22}(x) \end{bmatrix} \text{ [dB]}.$$

The first column is constant because transmitter TX-1 and both receivers are stationary. Figure 20 plots the second column of this gain matrix showing the link $g_{22}(x)$ and interference $g_{12}(x)$ terms.

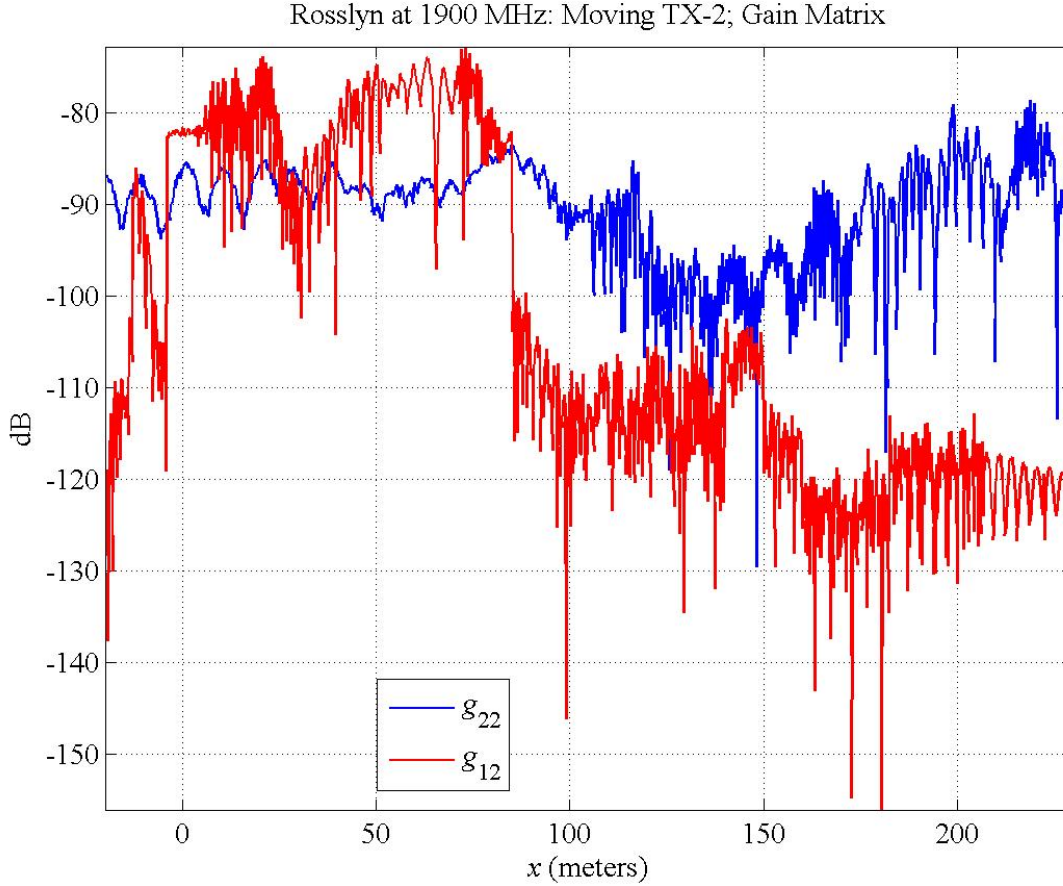


Figure 20. Gain matrix at 1.9 GHz for the two-link mobile wireless network.

The channel gain $g_{22}(x)$ models the link from the moving street-level transmitter TX-2 to its rooftop receiver RX-2. This channel is relatively flat because there is little blocking by buildings along the track (Figure 14). However, the channel gain $g_{12}(x)$ models the interference from at receiver RX-1 produced by the moving street-level transmitter TX-2. The preceding plots show that TX-2 broadcasts up the street containing RX-1 in the initial part of its track (Figures 16 and 17). Once the transmitter is past the entrance to this street, the buildings block the interference (Figures 18 and 19). Figure 20 shows the large-scale shadowing caused by the street geometry and the fast fading caused by the local diffraction effects.

Figure 20 shows the channel $h_{22}(x)$ has two distinct fading regimes:

- $x < 100$ meters: slow fading; characteristic of two-path propagation
- $150 < x$ meters: fast fading; no strong path.

Slow and fast fading affect wireless power control algorithms that allocate power based on “predicted” fading. Consequently, channels with longer spatial correlation are more amenable to prediction. The channel’s spatial correlation function is defined as [4, page 12]

$$C_{hh}(\Delta x) = \frac{R_{hh}(\Delta x)}{R_{hh}(0)}; \quad R_{hh}(\Delta x) = E[h_{22}(x)\bar{h}_{22}(x - \Delta x)].$$

The channel’s correlation distance $\Delta x(\rho)$ is defined as the first positive distance where correlation drops below the specified correlation:

$$\Delta x(\rho) = \operatorname{argmin} \{ \Delta x \geq 0 : C_{hh}(\Delta x) \leq \rho \}.$$

Figures 21 and 22 compare the estimated spatial correlation function for slow and fast fading, respectively ($\tilde{h}_{22}(x)$ in the fading estimate means that the linear trend was removed from the channel magnitude before estimating the correlation). The spatial correlation function over the slow-fading region shows typical “two-path” fading pointing to Rician fading. The slow-fading channel retains 90% correlation for almost a meter: $\Delta x(90\%) = 0.9$ meters. The fast-fading region rapidly decorrelates and has little recognizable sidelobe structure: $\Delta x(90\%) = 0.07$ meters. Table 9 compares the spatial correlation distances for both regions.

Table 9. Spatial correlation distance: 1.9 GHz.

Region	$\Delta x(50\%)$	$\Delta x(90\%)$
Slow	2.32 m	0.90 m
Fast	0.36 m	0.07 m

Figures 23 and 24 estimate the fading distribution for slow and fast fading, respectively. The slow fading registers Rician fading but identifying fast fading is more problematic. The lognormal distribution is best matched for wireless power control based on the Kalman filter. Wireless power control algorithms that adapt to multiple fading regimes promise greater performance than algorithms restricted to a single-mode fading.

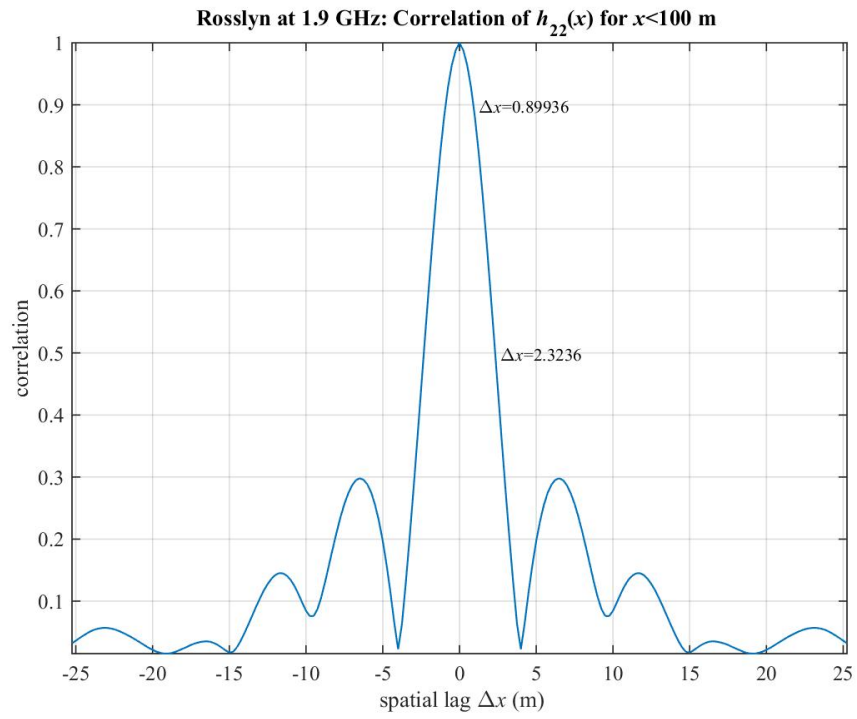


Figure 21. Spatial correlation of $h_{22}(x)$ on $-20 < x < 100$ (m).

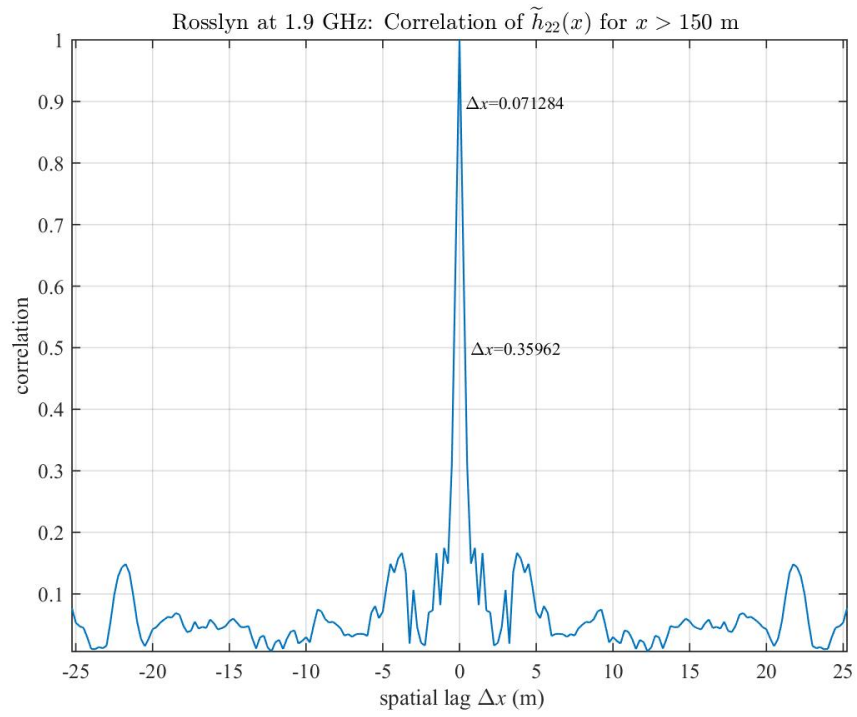


Figure 22. Spatial correlation of $\tilde{h}_{22}(x)$ on $150 < x$ (m).

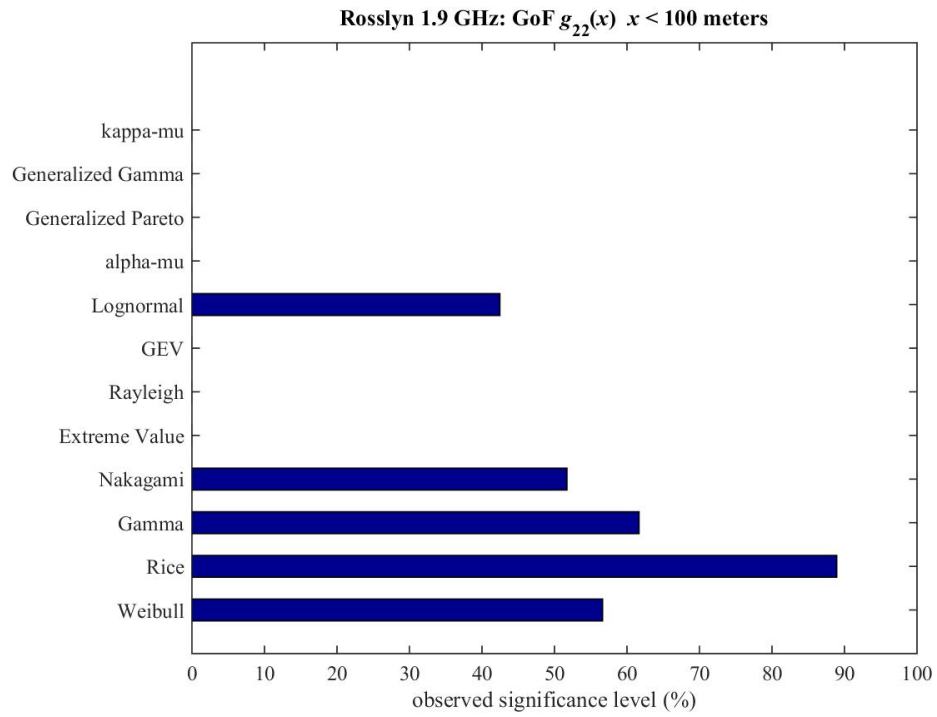


Figure 23. Goodness-of-Fit for $|h_{22}(x)|^2$ on $-20 < x < 100$ (m).

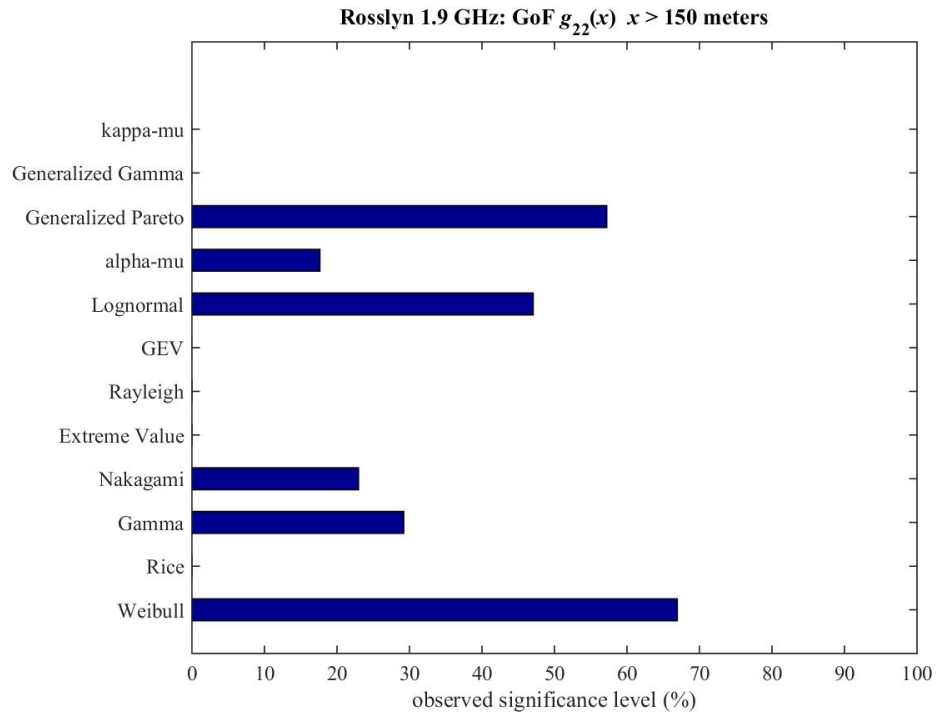


Figure 24. Goodness-of-Fit for $|\tilde{h}_{22}(x)|^2$ on $150 < x$ (m).

3.3 URBAN PROPAGATION AT 2.4 GHZ

Figure 25 shows the gain matrix at 2.4 GHz of the two-link mobile network as TX-2 travels along the x -axis. This plot is included for comparison to the 1.9-GHz gain matrix. As in the 300-MHz simulation and the 1.9-GHz simulation, both transmitters and receivers employ a half-wavelength vertical dipoles. Both plots show the same structure: large-scale shadowing caused by the street geometry and fast fading caused by the local diffraction effects. Any adaptive wireless power control algorithm must handle both types of fading.

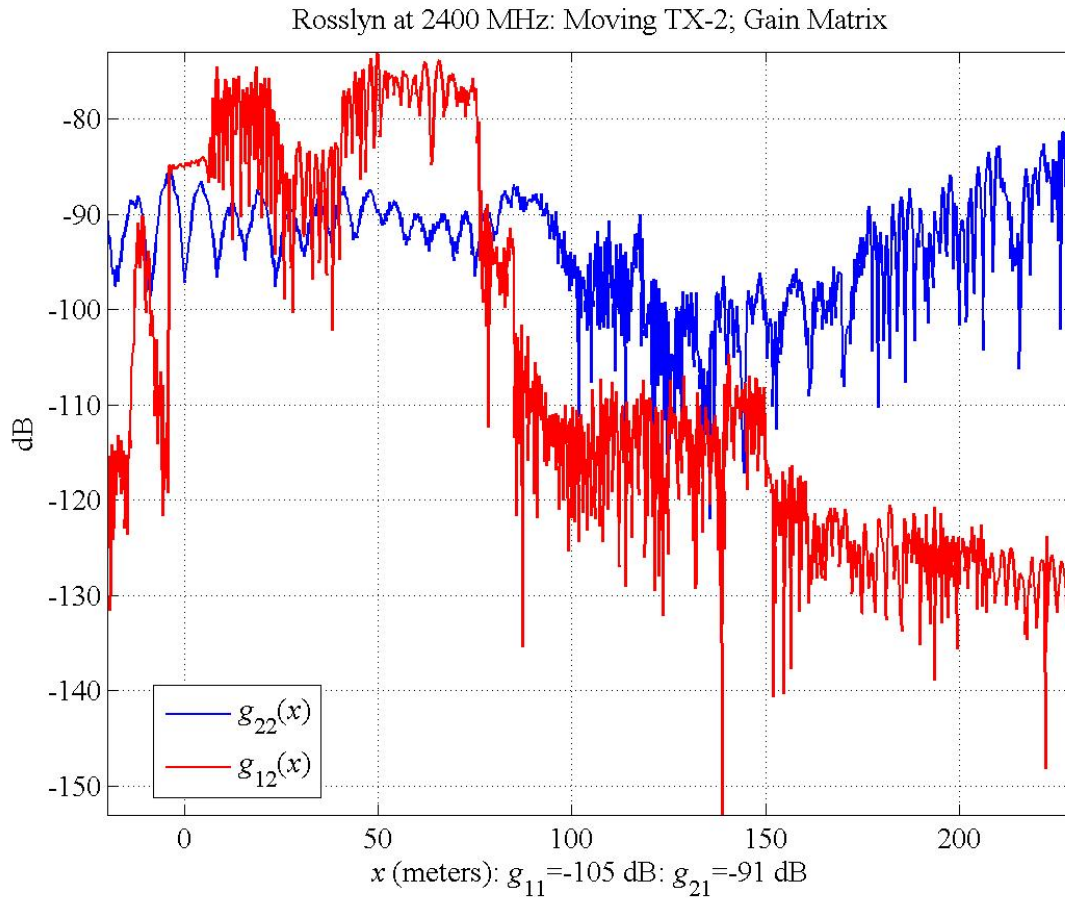


Figure 25. Gain matrix at 2.4 GHz for the two-link mobile wireless network.

4. INTERLUDE: TRADE-OFFS AND PARETO POINTS

This section reviews a few results multi-objective optimization necessary to state optimal trade-offs between competing objective. Trade-offs between competing objectives are conveniently stated using *vector inequalities*.

Definition 3 The vector $\mathbf{x} \in \mathbb{R}^N$, is said to be element-wise non-negative if no element of \mathbf{x} is negative: $x_m \geq 0$ denoted as $\mathbf{x} \geq \mathbf{0}$. If $\mathbf{y} \in \mathbb{R}^N$, the vector inequality $\mathbf{x} \leq \mathbf{y}$ means $\mathbf{y} - \mathbf{x} \geq \mathbf{0}$.

The set of all element-wise nonnegative vectors is denoted as

$$\mathbb{R}_+^N := \{\mathbf{y} \in \mathbb{R}^N : \mathbf{y} \geq \mathbf{0}\}.$$

This closed, convex orthant of \mathbb{R}^N determines the geometry of this vector inequality.

Definition 4 (Minimum) [3, page 45] Let $Y \subset \mathbb{R}^N$. A point $\mathbf{y}_{\min} \in Y$ is called the minimum of Y if and only if $\mathbf{y}_{\min} \leq \mathbf{y}$ for all $\mathbf{y} \in Y$.

Equivalently, Y is completely contained in the positive orthant \mathbb{R}_+^N located at the minimum [3, page 45]:

$$Y \subseteq \mathbf{y}_{\min} + \mathbb{R}_+^N.$$

Figure 26 shows the relation between a cone $Y \subseteq \mathbb{R}^2$ to the positive orthant \mathbb{R}_+^2 for the vertex of the cone to be the minimum of the cone. However, sets with a minimum are relatively rare. More common are the minimum elements.

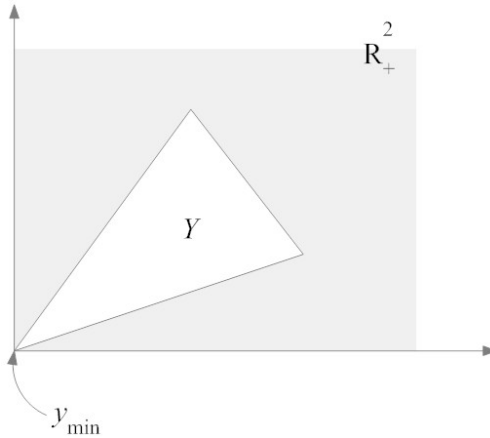


Figure 26. Vertex of a cone.

Definition 5 (Minimal Elements) A point $\mathbf{y}_{\text{ME}} \in Y$ is called a minimal element if and only if for all $\mathbf{y} \in Y$ such that $\mathbf{y} \leq \mathbf{y}_{\text{ME}} \implies \mathbf{y} = \mathbf{y}_{\text{ME}}$.

The geometry for $\mathbf{y}_{\text{ME}} \in Y$ to be a minimal element requires that the negative orthant located at \mathbf{y}_{ME} intersects Y only at the minimal element. This geometry is formalized in the Contact Theorem [77, Contact Theorem]. Figure 27 shows how the negative orthant $-\mathbb{R}_+^2$ must attach to $Y \subset \mathbb{R}^2$ for \mathbf{y}_{ME} to be a minimal element.

Theorem 1 (Contact Theorem [77]) : A point $\mathbf{y}_{\text{ME}} \in Y$ is a minimal element if and only if

$$\{\mathbf{y}_{\text{ME}}\} = (\mathbf{y}_{\text{ME}} - \mathbb{R}_+^N) \cap Y.$$

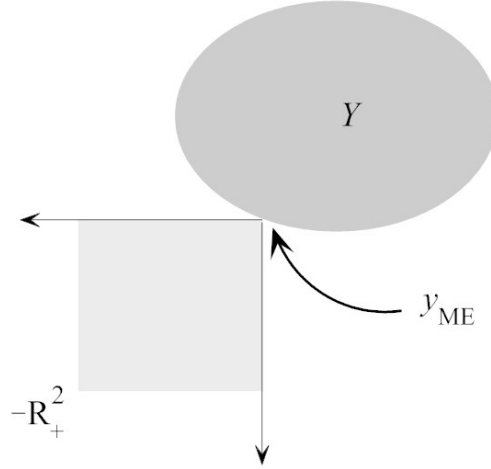


Figure 27. A minimal element.

Optimal trade-offs for a multiobjective function $\mathbf{h} : X \subseteq \mathbb{R}^M \rightarrow \mathbb{R}^N$ are determined by minimal elements of the performance image. Figure 28 illustrates the image of a Pareto optimal point for $\mathbf{h} : X \subseteq \mathbb{R}^M \rightarrow \mathbb{R}^2$.

Definition 6 (Pareto Optimal) [3, page] Let $\mathbf{h} : X \subseteq \mathbb{R}^M \rightarrow \mathbb{R}^N$ and

$$\mathbf{h}(X) := \{\mathbf{h}(\mathbf{x}) : \mathbf{x} \in X\}.$$

A element $\mathbf{x}_p \in X$ is called Pareto optimal if and only if $\mathbf{h}(\mathbf{x}_p)$ is a minimal element of $\mathbf{h}(X)$.

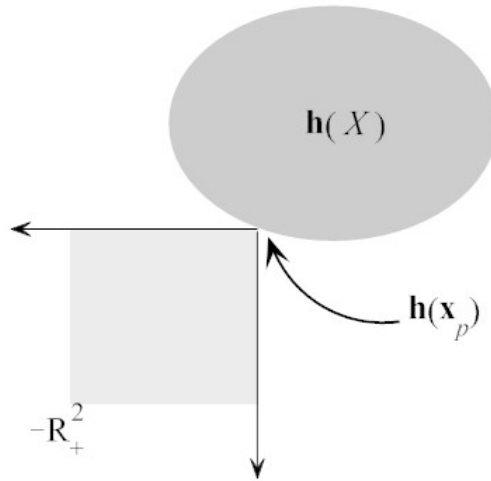


Figure 28. Pareto optimal point for the mapping $\mathbf{h} : X \subseteq \mathbb{R}^M \rightarrow \mathbb{R}^2$.

The image of all Pareto optimal points is called the *Pareto front* or *Pareto frontier*. Figure 29 illustrates such Pareto front marked by the heavy line. The dashed lines indicate that this Pareto front does not “wrap” past the vertical and horizontal axis.

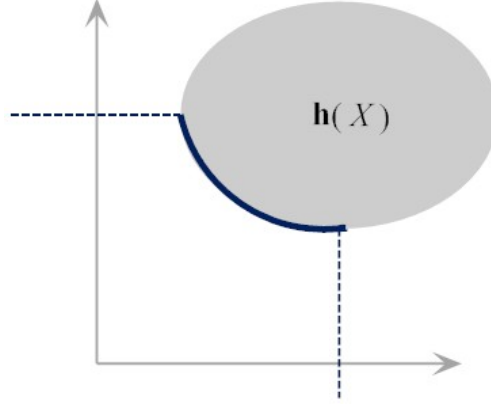


Figure 29. Pareto front of the mapping $\mathbf{h} : X \subseteq \mathbb{R}^M \rightarrow \mathbb{R}^2$.

This section closes with a few observations about the Pareto front and its specialization to the power-rate image. The first observation points out that the Pareto front must lie in the boundary of the performance image

Lemma 1 *Let $\mathbf{h} : X \subseteq \mathbb{R}^M \rightarrow \mathbb{R}^N$. The Pareto front of $\mathbf{h}(X)$ lies in the boundary of $\mathbf{h}(X)$.*

If the image is its own boundary, such as the graph of a function, the analytic properties of the function may force the image to be its own Pareto front.

Lemma 2 *Let $h : X \subseteq \mathbb{R} \rightarrow \mathbb{R}$ be continuous and strictly decreasing. Define $H : X \rightarrow \mathbb{R}^2$ as*

$$H(x) = \begin{bmatrix} x \\ h(x) \end{bmatrix}.$$

Then the Pareto front of $H(X)$ is $H(X)$.

When the generic Pareto theory is specialized to the power-rate image, the negative orthant is replaced by the quadrant pointing to “less power and more rate”. Let $\mathcal{Q} \subset \mathbb{R}^2$ denote this quadrant:

$$\mathcal{Q} := \left\{ \begin{bmatrix} -p_\Sigma \\ r_\Sigma \end{bmatrix} : p_\Sigma, r_\Sigma \geq 0 \right\}.$$

Figure 30 shows this quadrant in contact with the Pareto front of the power-rate image. The upper boundary of the power-rate image is the Pareto front—no variation in the power vector exists that simultaneously decreases power and increases throughput.

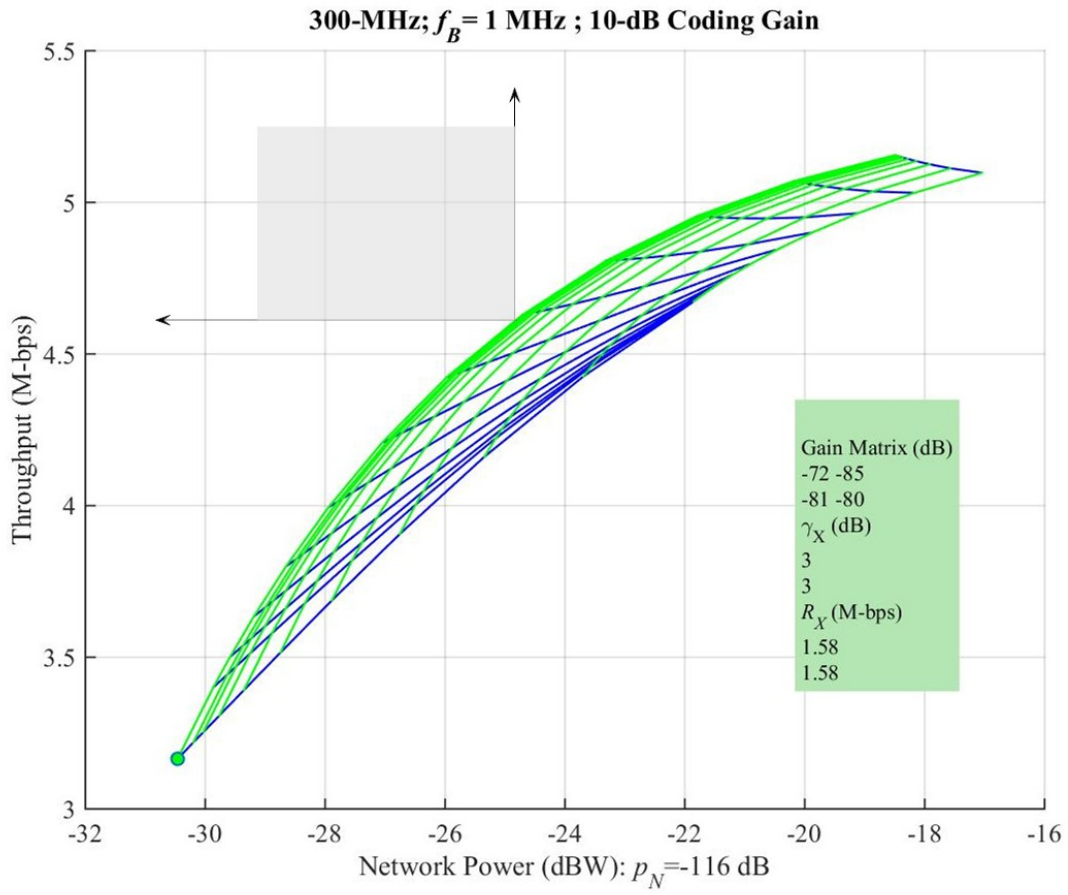


Figure 30. Power-rate image for a two-link wireless network meeting QoS with the quadrant marking a Pareto point.

5. POWER-RATE TRADE-OFFS

Section 3 describes the *geometry* of the two-link mobile wireless network operating in urban scenarios. This section describes a wireless power control *system* and consequent model of network performance. Power and throughput trade-offs are basic performance objectives of wireless power control *systems* operating in power-limited, ground-level wireless networks.

Figure 31 is a schematic of a generic wireless power control system for the smallest and simplest two-link mobile wireless network of Section 3. Each controller commands their respective transmitter so that the received SINR “tracks” the specified SINR. These controllers are in conflict because the transmit power on one link is the interference power on the other link. This model of a wireless power control system is the common operational framework for the forthcoming distributed wireless power control algorithms. This common model permits comparisons without getting entangled in system-specific implementations.

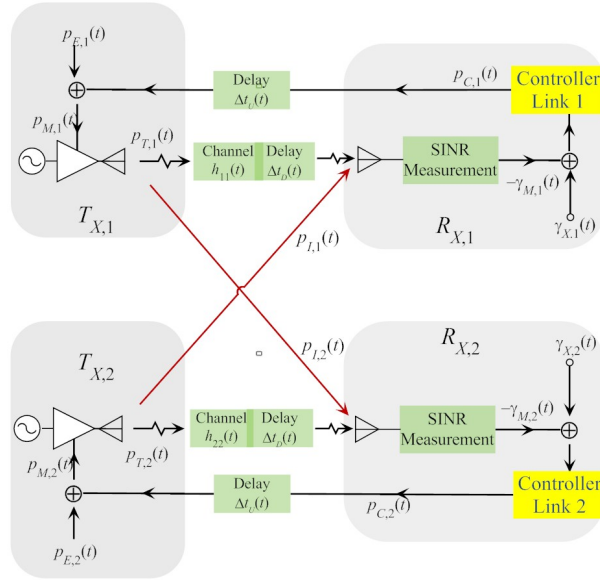


Figure 31. Two-link schematic of a generic distributed wireless power control system.

The uplink delays and downlink delays model the signal processing chain to implement this distributed wireless power control. For simplicity, all links use the same uplink delays and the same downlink delays. The downlink delay Δt_D models the processing delays mapping the analog received signal into the digital controllers, undertake measurements that may be allowed only once per frame, and then compute the power control decision. The uplink delay Δt_U models the processing delay for the controllers to map the power control decision into an analog power-control message that is broadcast back to the transmitters, demodulating this message at the transmitters, and then implement the power control command at the transmitter’s power amplifier. If the signals are narrowband, the wireless power flows are modeled by Equation (3) and repeated here for convenience:

$$\mathbf{p}_R(t) = G(t)\mathbf{p}_T(t) + \mathbf{p}_N(t).$$

Figure 31 generalizes the wireless power flows to account for the downlink delay:

$$\mathbf{p}_R(t) = G(t)\mathbf{p}_T(t - \Delta t_D) + \mathbf{p}_N(t).$$

Figure 31 also shows the transmitters setting their power from delayed and noise-corrupted version of their receiver's power command. Although the wireless system describes a digital messaging scheme, the following model eliminates the digital processing and uses the power control vector itself to set the transmitter's power:

$$\mathbf{p}_T(t) = \mathbf{p}_C(t - \Delta t_U) + \mathbf{p}_E(t).$$

The wireless power control models in this report lumps both delays into the single delay τ and omits the error vector. Consequently, the transmitter's power vector is modeled as delayed version of the control power vector:

$$\mathbf{p}_T(t) = \mathbf{p}_C(t - \tau). \quad (8)$$

Therefore, power control in the wireless network is the narrowband but time-delayed system:

$$\mathbf{p}_R(t) = G(t)\mathbf{p}_C(t - \tau) + \mathbf{p}_N(t). \quad (9)$$

The update commands are typically issued on a common clock on each link. One timing scheme resets the transmitter's power at the start of each frame in the received signal. Figure 32 illustrates this update-per-frame and the timing—1 millisecond per frame—used in this report. At the start of each received frame, receiver's controller has completed the power measurements, computed the power control, loaded the power control into a message, and starts the broadcast of the power-control update back to the transmitter.

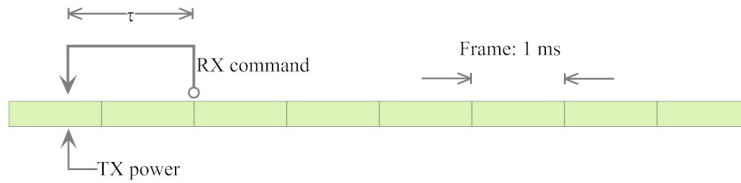


Figure 32. Power control timing with the update issued at the “downbeat” of each frame.

The signal-to-interference and noise ratio (SINR) bounds the throughput of the network. The signal power vector is measured at the input to the receiver's detector:

$$\mathbf{p}_S(t) = G_S(t)\mathbf{p}_C(t - \tau); \quad G_S(t) = \begin{bmatrix} g_{11}(t) & 0 \\ 0 & g_{22}(t) \end{bmatrix}.$$

The interference power vector is measured at the input to the receiver's detector:

$$\mathbf{p}_I(t) = G_I(t)\mathbf{p}_C(t - \tau); \quad G_I(t) = \begin{bmatrix} 0 & g_{12}(t) \\ g_{21}(t) & 0 \end{bmatrix}.$$

The measured SINR vector is

$$\gamma_M(\mathbf{p}_C; t) = \frac{\mathbf{p}_S(t)}{\mathbf{p}_N(t) + \mathbf{p}_I(t)},$$

where the “.” on the fraction denotes element-wise division. The generalization to multiple links $l = 1, \dots, L$ gives the standard form for the SINR [79, Equation 1]:

$$\gamma_{M,l}(\mathbf{p}_C; t) = \frac{g_{ll}(t)p_{C,l}(t - \tau)}{p_{N,l}(t) + \sum_{m \neq l} g_{lm}(t)p_{T,m}(t - \tau)}. \quad (10)$$

Figure 31 shows the controllers compare this measured SINR $\gamma_{M,l}(t)$ to the external SINR $\gamma_{M,l}(t)$. The controllers command their transmitters to vary their broadcast power so that measured SINR “tracks” the external SINR. The tracking error and the adaptive power control algorithms are the focus of this report—not the problems of measuring the SINR.

Measuring SINR: As shown in Figure 31, the controllers are limited to measurements that can be extracted from the received signal $s_{R,l}(t)$ as seen through the receiver’s antenna system. Consequently, measuring the SINR $\gamma_{M,l}(t)$ is not straightforward. Most radios do admit measurement of the total received power $p_{R,l}(t)$. Some frames allocate slots to measure the noise and interference $p_{N,l} + p_{I,l}(t)$ by commanding the transmitter to turn off. If the interference dominates the noise, $\gamma_{M,l}(t)$ admits an estimate from these measurements. The Kalman filter approach recognizes that state-space estimates obtained from indirect measurements are typically higher quality than downstream approximations, and are obtained with less disruption of the hardware and waveform modifications. For example, including the gain $g_l(t)$ as part of the state allows a Kalman filter to estimate the SINR by measuring only the received power $p_{R,l}(t)$.

This report ranks wireless power control algorithms assuming each controller has access only to the SINR $\gamma_{M,l}(t)$. The assumption allows an “apples-to-apples” comparison of algorithm performance in tactical environments without the confounding effects of implementations. Roughly speaking, optimizing network performance means the following:

WPC-1 Minimize network power p_Σ (watts)

WPC-2 Maximize network throughput R_Σ (bps).

Definition 7 (Network Power) *The network power is defined to be the total transmit power:*

$$p_\Sigma(t) := \sum_{l=1}^L p_{T,l}(t) \quad [\text{watts}].$$

Remarks: (i) The transmit power is modeled using Equation (8), so that the network power is the sum of the control powers:

$$p_\Sigma(\mathbf{p}_C; t) = \sum_{l=1}^L p_{C,l}(t - \tau).$$

(ii) This network power model does not include the power required for messaging, processing, and overhead.

Definition 8 (Network Throughput) *The network throughput is the sum of the link capacities integrated across the common bandwidth*

$$R_\Sigma(\mathbf{p}_C; t) := f_B \sum_{l=1}^L \log_2(1 + \gamma_{M,l}(\mathbf{p}_C; t)).$$

Remarks: (i) The network is narrowband. (ii) The throughput is an upper bound on realizable rates. (iii) Using the SINR of Equation (10) assumes that interference is independent of the signal.

Definition 9 (Network Performance) The network performance is the mapping $\mathfrak{N} : C_b(\mathbb{R}, \mathbb{R}_+^L) \times \mathbb{R} \rightarrow \mathbb{R}_+^2$ that determines the instantaneous trade-off between throughput and power:

$$\mathfrak{N}(\mathbf{p}_C; t) := \begin{bmatrix} p_\Sigma(\mathbf{p}_C; t) \\ R_\Sigma(\mathbf{p}_C; t) \end{bmatrix} \begin{matrix} \text{watts} \\ \text{Mbps} \end{matrix} \quad (11)$$

For each fixed time t_0 , the network performance image is the subset of the power-rate plane:

$$\mathfrak{N}(\mathbb{R}_+^L, t_0) := \{\mathfrak{N}(\mathbf{p}_C, t_0) : \mathbf{p}_C \in \mathbb{R}_+^L\} \subseteq \mathbb{R}_+^2.$$

Power allocations that deliver optimal performance—maximum throughput and minimum power—lie on the upper boundary of this image. At these Pareto point, where no change in power can simultaneously decrease power and increase throughput. The next example makes this geometry explicit.

Example 1 (Performance Image) Assume the gain matrix is fixed:

$$G = \begin{matrix} & \text{TX-1} & \text{TX-2} \\ \begin{matrix} \text{RX-1} \\ \text{RX-2} \end{matrix} & \begin{bmatrix} g_{11} & g_{12} \\ g_{21} & g_{22} \end{bmatrix} \end{matrix} = \begin{bmatrix} -72 & -75 \\ -71 & -80 \end{bmatrix} \text{ [dB]}.$$

Set the noise power $p_N = -131 \text{ dBW}$. Figure 33 shows the network performance image for the transmit powers sweeping $-40 \leq p_{C,1}, p_{C,2} \leq 0 \text{ dBW}$. The green lines correspond to constant power on Link 2. The blue lines correspond to constant power on Link 1. The heavy green line has the smallest power allocated to Link 2. The heavy blue line has the smallest power allocated to Link 1. The plot shows that to maximize throughput and minimize power, turn Link 2 off and allocate all the power to the Link 1.

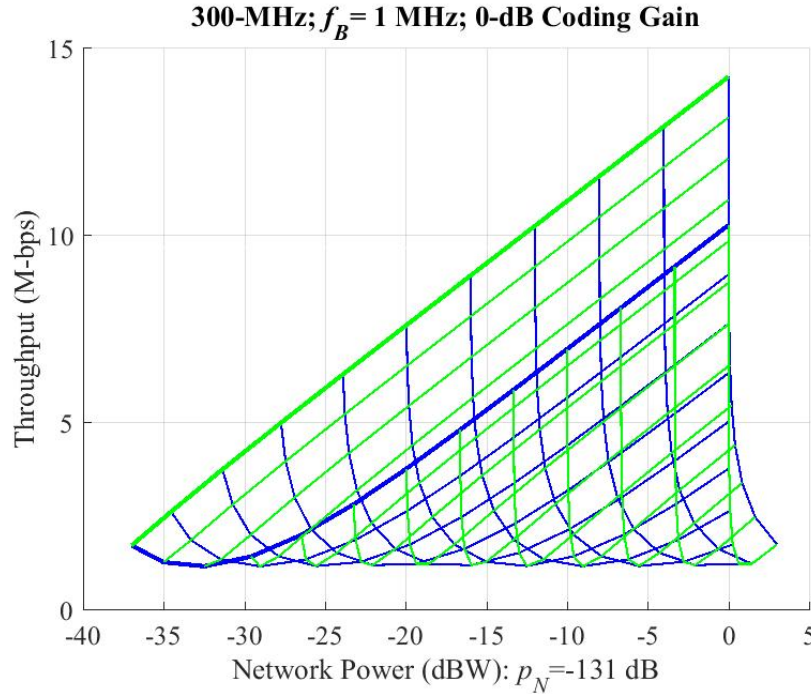


Figure 33. Two-link network performance image; the heavy green line is the Pareto front.

Figure 33 reports that the optimal network performance arises by allocating all network power to Link 1. This link has maximum signal gain. However, allowing only the strongest link to broadcast voids the meaning of “network”. Consequently, most wireless power control algorithms aim at “fairer” solutions by enforcing *quality-of-service* (QoS) constraints [12], [13]. One common QoS requires the measured SINR to exceed a user-specified external SINR on all links:

$$\gamma_{X,l}(t) \leq \frac{g_{ll}p_{C,l}(t - \tau)}{p_{N,l}(t) + \sum_{m \neq l} g_{lm}p_{C,m}(t - \tau)} = \gamma_{M,l}(\mathbf{p}_C; t)$$

for $l = 1, \dots, L$. In vector notation,

$$\gamma_X(t) \stackrel{\leq}{\cdot} \frac{G_S \mathbf{p}_C(t - \tau)}{\mathbf{p}_N(t) + G_I \mathbf{p}_C(t - \tau)} =: \gamma_M(\mathbf{p}_C; t), \quad (12)$$

where the “ $\stackrel{\leq}{\cdot}$ ” denotes the vector inequality and the “ \cdot ” on the fraction denotes the element-wise division. That is, the network performance is to be optimized under the constraint that each link is guaranteed a minimal throughput.

WPC-1 Maximize network throughput R_Σ (bps)

WPC-2 Minimize network power p_Σ (watts)

WPC-3 Guarantee QoS.

The pitfall of this approach is that there may be no power allocations that meet the QoS. Consequently, all approaches to the power-rate-QoS constraints require some knowledge of the feasible control vectors. Let

$$\mathcal{P}_C(t_0) := \{\mathbf{p}_C \in \mathbb{R}_+^L : \gamma_X(t_0) \stackrel{\leq}{\cdot} \gamma_M(\mathbf{p}_C; t_0)\}$$

denote the instantaneous *feasible* set of control vectors at time t_0 . The network performance image at time t_0 is the subset of the power-rate plane:

$$\mathfrak{N}(\mathcal{P}_C, t_0) := \{\mathfrak{N}(\mathbf{p}_C, t_0) : \mathbf{p}_C \in \mathcal{P}_C(t_0)\} \subset \mathbb{R}_+^2.$$

The following example uses the same gain matrix and noise level as in the proceeding example. The QoS severely constrain the resulting network performance image.

Example 2 (Performance Image: QoS) Assume the noise is $p_N = -131$ dBW and the gain matrix is

$$G = \begin{bmatrix} g_{11} & g_{12} \\ g_{21} & g_{22} \end{bmatrix} = \begin{bmatrix} -72 & -75 \\ -71 & -80 \end{bmatrix} \text{ [dB]}.$$

Figure 34 shows the resulting network performance image with QoS: $\gamma_M \stackrel{\geq}{\cdot} -5$ dB or equivalently, each throughput exceeds 0.395 Mbps. Section 7 details the explicit parameterization of this power-rate image.

Figure 34 shows the power-rate trade-offs that are possible under the QoS constraint. This image occupies the lower edge of the non-QoS performance image in Figure 33. The QoS performance image shows that massive increases in network power have little effect on the network throughput. Both figures point to the ideal wireless power control algorithm. Such an algorithm would compute

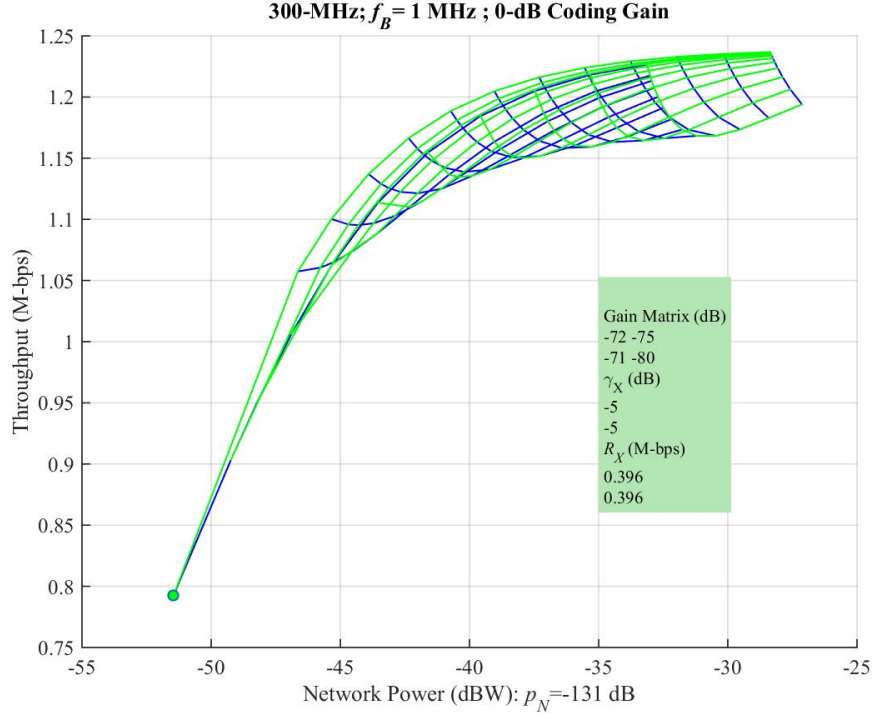


Figure 34. Two-link network performance image with QoS. The upper green line is the Pareto front.

- the Pareto front of $\mathfrak{N}(\mathcal{P}_C, t_0)$,
- the control vectors that parameterize these Pareto fronts.

This distributed wireless power control is computationally challenging—the multiobjective optimization must be implemented over a distributed network governed by the delayed control system of Equation (9). The power-rate trade-off is avoided by most wireless power control algorithms by constraining one of the objectives. Table 10 lists selected variations.

Table 10. Selected single-objective power control formulations.

Description	Objective	Constraint: $\mathbf{0} \leq \mathbf{p}$
Power-constrained	$\max\{R_\Sigma(\mathbf{p})\}$	Power: $p_\Sigma = \mathbf{1}^\top \mathbf{p}$
Rate-constrained	$\min\{\mathbf{1}^\top \mathbf{p}\}$	QoS: $R_{b,X} \leq R_b(\mathbf{p})$
Power-bounded	$\max\{R_\Sigma(\mathbf{p})\}$	Power: $\mathbf{p} \leq \mathbf{p}_{\text{MAX}}$
Rate-power Bounded	$\min\{\mathbf{1}^\top \mathbf{p}\}$	QoS: $R_{b,X} \leq R_b(\mathbf{p})$; Power: $\mathbf{p} \leq \mathbf{p}_{\text{MAX}}$

Nevertheless, the first challenge for any wireless power control algorithm—distributed or centralized—is to determine the set of feasible vectors. Indeed, the QoS constraint may be so stringent that no power control can deliver the QoS. Section 7 addresses the existence of feasible power control $\mathcal{P}_C \neq \emptyset$ for the static channel. The next section reviews matrix inequalities to facilitate this discussion.

6. INTERLUDE: MATRIX INEQUALITIES

Matrix and vector inequalities are basic tools for network optimization. There are several notations for these inequalities. The “ $\dot{\leq}$ ” was selected for similarity to the “pointwise” operations of MATLAB®.

Definition 10 [46, Chapter 15], [47, Chapter 16] A matrix $A \in \mathbb{R}^{M \times N}$ is said to be element-wise non-negative if no element of A is negative: $A_{m,n} \geq 0$ or $A \dot{\geq} \mathbf{0}$.

Just as scalar inequalities are preserved under multiplication by non-negative scalars, vector inequalities are preserved under multiplication by element-wise non-negative matrices.

Lemma 3 [46, page 531] Let $A \in \mathbb{R}^{M \times N}$ be element-wise non-negative: $A \dot{\geq} \mathbf{0}$. If $\mathbf{x}, \mathbf{y} \in \mathbb{R}^N$ and $\mathbf{x} \dot{\leq} \mathbf{y}$, then $A\mathbf{x} \dot{\leq} A\mathbf{y}$.

The wireless optimization problems reduce to constrained optimization problems with inequality constraints, including the constraint that the power vector \mathbf{p} is non-negative:

Definition 11 The closed, convex orthant of \mathbb{R}^L is denoted as

$$\mathbb{R}_+^L := \{\mathbf{p} \in \mathbb{R}^L : \mathbf{p} \dot{\geq} \mathbf{0}\}.$$

Several wireless optimization problems reduce to linear matrix inequalities. The following result parameterizes a matrix inequality when the matrix is invertible.

Corollary 1 Suppose $A \in \mathbb{R}^{L \times L}$ is invertible. Let $\mathbf{b} \in \mathbb{R}^L$. Then

$$\{\mathbf{x} \in \mathbb{R}^L : A\mathbf{x} \dot{\geq} \mathbf{b}\} = A^{-1}\mathbf{b} + A^{-1}\mathbb{R}_+^L.$$

Proof: (\subseteq): The inequality $A\mathbf{x} \dot{\geq} \mathbf{b}$ is equivalent to the equality $A\mathbf{x} = \mathbf{b} + \mathbf{y}$ for some $\mathbf{y} \dot{\geq} \mathbf{0}$. Apply the matrix inverse A^{-1} to the equality to get $\mathbf{x} = A^{-1}\mathbf{b} + A^{-1}\mathbf{y}$. (\supseteq): Conversely if $\mathbf{x} = A^{-1}\mathbf{b} + A^{-1}\mathbf{y}$ for $\mathbf{y} \dot{\geq} \mathbf{0}$, $A\mathbf{x} = \mathbf{b} + \mathbf{y}$ or, equivalently, $A\mathbf{x} \dot{\geq} \mathbf{b}$. ///

In addition to the element-wise inequality, there is the element-wise vector product

$$\mathbf{x} \odot \mathbf{y} := [x_m y_m]$$

and the element-wise fraction

$$\frac{\mathbf{x}}{\mathbf{y}} := \left[\frac{x_m}{y_m} \right].$$

Several wireless optimization problems require inverting a matrix of the form $I - F$ where $F \dot{\geq} \mathbf{0}$. If F is a contraction, the geometric series computes the inverse and reveals that the inverse is a element-wise non-negative matrix because each term F^k is an element-wise non-negative matrix:

$$(I - F)^{-1} = \sum_{k=0}^{\infty} F^k \dot{\geq} \mathbf{0}.$$

The key assumption is that F is a contraction relative to some matrix norm. The spectral radius determines this matrix norm.

Definition 12 (Spectral Radius) If $\lambda_1, \dots, \lambda_L$ are the eigenvalues of matrix $A \in \mathbb{C}^{L \times L}$, the maximum extent of the eigenvalues

$$\rho(A) := \max\{|\lambda_l|\}$$

is called the spectral radius of A .

Theorem 2 [71, page 384] For every matrix A and every $\epsilon > 0$, there exists a vector norm $\|\cdot\|_v$ such that the induced matrix norm is ϵ -bounded by the spectral radius:

$$\|A\|_v := \sup\{\|A\mathbf{x}\|_v : \|\mathbf{x}\|_v \leq 1\} \leq \rho(A) + \epsilon.$$

If every eigenvalue λ of A with $|\lambda| = \rho(A)$ has only linear elementary divisors, there is a vector norm $\|\cdot\|_v$ such that the induced matrix norm satisfies

$$\|A\|_v = \rho(A).$$

Example 3 If $b, c > 0$, the spectral radius of

$$F = \begin{bmatrix} 0 & b \\ c & 0 \end{bmatrix}$$

is the geometric mean of b and c : $\rho(F) = \sqrt{bc}$. If $\rho_0 > 0$, all matrices F that satisfy $\rho(F) \leq \rho_0$ are parameterized by the half-plane

$$\log(b) + \log(c) \leq 2 \log(\rho_0).$$

If F has a spectral radius strictly less than one: $\rho(F) < 1$, there is a matrix norm such that $\|F\| < 1$ and $(I - F)$ is invertible using its geometric series or, equivalently, the power method. To solve $(I - F)\mathbf{p} = \mathbf{y}$, observe the partial sums

$$\mathbf{p}_K = \sum_{k=0}^K F^k \mathbf{y}$$

converge to the solution and satisfy the recursion

$$\mathbf{p}_K = \mathbf{y} + F\mathbf{p}_{K-1}.$$

The partial sums converge according to the tail of the geometric series at a rate determined by the spectral radius.

Lemma 4 (Partial Sum) Let $F \in \mathbb{R}^{L \times L}$ with $\|F\| < 1$. The absolute error between the matrix inverse $(I - F)^{-1}$ and the associated partial sums is bounded as

$$\text{AbsErr}(F; K) := \left\| (I - F)^{-1} - \sum_{k=0}^K F^k \right\| \leq \frac{\|F\|^{K+1}}{1 - \|F\|}; \quad n = 0, 1, \dots$$

Use Theorem 2 to select a matrix norm

$$\|F\| \leq \rho(F)(1 + \epsilon); \quad 1 \gg \epsilon > 0.$$

Lemma 4 bounds the absolute error as

$$\text{AbsErr}(F; K) \leq \frac{\rho(F)^{K+1}(1 + \epsilon)^{K+1}}{1 - \rho(F)}.$$

7. POWER-RATE TRADE-OFFS IN STATIC CHANNEL

A basic problem in wireless power control is setting the minimum SINR requirements. The problem is that the user-specified SINR γ_X may be so stringent that no SINR vector γ_M exists that satisfies $\gamma_M \dot{\geq} \gamma_X$ or that the set feasible control vectors \mathcal{P}_C is empty.

The next result determines when feasible control vectors exist—assuming a constant channel, a constant noise power, and constant γ_X . In this *static channel*, the uplink and downlink delays are not present and the set of feasible control *functions* devolves to a set of feasible control *vectors*.

The seminal paper in wireless power control was written in 1993 by Foschini & Miljanic [22]. This remarkable paper determined that the set of feasible control vectors—if nonempty—must be a cone. This cone parameterizes the power-rate image. The geometry of the power-rate image determines best possible network performance. This section reviews selected results of the Foschini & Miljanic (FM) paper and presents several power-rate images showing the challenges for computing optimal performance.

Theorem 3 (FM) [22], [75], [82] *Let $G \in \mathbb{R}^{L \times L}$ be a constant gain matrix for L links. Define the signal and interference matrices as*

$$G_S = \begin{bmatrix} g_{11} & 0 & 0 & \cdots & 0 \\ 0 & g_{22} & 0 & \cdots & 0 \\ \vdots & & \ddots & & \vdots \\ 0 & 0 & \cdots & 0 & g_{LL} \end{bmatrix}; \quad G_I = G - G_S.$$

Let $\mathbf{p}_N \in \mathbb{R}_+^L$ denote the constant and positive noise vector: $\mathbf{p}_N \dot{>} \mathbf{0}$. Let $\gamma_M : \mathbb{R}^L \rightarrow \mathbb{R}^L$ denote the measured SINR vector

$$\gamma_M(\mathbf{p}_C) = \frac{G_S \mathbf{p}_C}{\mathbf{p}_N + G_I \mathbf{p}_C}.$$

Let γ_X denote a constant, user-specified SINR constraint vector. Let \mathcal{P}_C denote the set of feasible control vectors:

$$\mathcal{P}_C := \{\mathbf{p}_C \in \mathbb{R}^L : \gamma_X \dot{\leq} \gamma_M(\mathbf{p}_C)\}.$$

If the spectral radius of the feedback matrix

$$F := G_S^{-1} \Gamma_X G_I; \quad \Gamma_X := \text{diag}(\gamma_X) \quad (13)$$

is strictly less than unity: $\rho(F) < 1$, the vector

$$\mathbf{p}_{\min} := (I - F)^{-1} G_S^{-1} \Gamma_X \mathbf{p}_N \quad (14)$$

is well-defined, and is the vertex of the feasible control vectors:

$$\mathcal{P}_C = \mathbf{p}_{\min} + (I - F)^{-1} \mathbb{R}_+^L \subseteq \mathbb{R}_+^L. \quad (15)$$

The power-rate mapping $\mathfrak{N} : \mathcal{P}_C \subset \mathbb{R}_+^L \rightarrow \mathbb{R}_+^2$ (Definition 9)

$$\mathfrak{N}(\mathbf{p}_C) := \begin{bmatrix} p_\Sigma \\ R_\Sigma \end{bmatrix} \begin{matrix} \text{watts} \\ \text{Mbps} \end{matrix} \quad (16)$$

parameterizes the network's power-rate image as

$$\mathfrak{N}(\mathcal{P}_C) = \mathfrak{N}(\mathbf{p}_{\min} + (I - F)^{-1} \mathbb{R}_+^L)$$

that has minimal element: $\mathfrak{N}(\mathbf{p}_{\min}) \dot{\leq} \mathfrak{N}(\mathcal{P}_C)$.

Proof: Cross multiply to get the linear inequality:

$$\begin{aligned}
\gamma_X &\leq \frac{G_S \mathbf{p}_C}{\mathbf{p}_N + G_I \mathbf{p}_C} \\
\iff \gamma_X \odot (\mathbf{p}_N + G_I \mathbf{p}_C) &\leq G_S \mathbf{p}_C \\
\iff \Gamma_X \mathbf{p}_N + \Gamma_X G_I \mathbf{p}_C &\leq G_S \mathbf{p}_C; \quad \Gamma_X := \text{diag}(\gamma_X) \\
\iff \Gamma_X \mathbf{p}_N &\leq G_S \mathbf{p}_C - \Gamma_X G_I \mathbf{p}_C \\
\iff G_S^{-1} \Gamma_X \mathbf{p}_N &\leq (I - G_S^{-1} \Gamma_X G_I) \mathbf{p}_C \\
\iff G_S^{-1} \Gamma_X \mathbf{p}_N &\leq (I - F) \mathbf{p}_C,
\end{aligned} \tag{17}$$

where “ \odot ” denotes the Hadamard or element-wise product. By hypothesis, $\rho(F) < 1$. Theorem 2 applies so that $I - F$ is invertible via the geometric series

$$(I - F)^{-1} = \sum_{n=0}^{\infty} F^n \geq 0.$$

Lemma 3 applies to parameterize all vectors $\mathbf{p}_C \in \mathbb{R}^L$ that satisfy Inequality (17) as the pointed cone:

$$\{\mathbf{p}_C \in \mathbb{R}^L : G_S^{-1} \Gamma_X \mathbf{p}_N \leq (I - F) \mathbf{p}_C\} = \mathbf{p}_{\min} + (I - F)^{-1} \mathbb{R}_+^L.$$

The geometric expansion also reveals that the inverse is element-wise non-negative by Equation (13). Therefore, $\mathbf{p}_{\min} \geq 0$ and the set of vectors that satisfy Inequality (17) must also lie in the non-negative orthant:

$$\mathbf{p}_{\min} + (I - F)^{-1} \mathbb{R}_+^L \subseteq \mathbb{R}_+^L.$$

That is, all the vectors satisfying Inequality (17) are feasible power vectors. For the minimal element, any feasible vector $\mathbf{p}_C \in \mathcal{P}_C$ must have total power exceeding the minimal power $\mathbf{1}^\top \mathbf{p}_{\min} \leq \mathbf{1}^\top \mathbf{p}_C$ by Equation (15). Likewise, feasibility forces

$$\gamma_M(\mathbf{p}_{\min}) = \gamma_X \leq \gamma_M(\mathbf{p}_C).$$

Thus, $\mathfrak{N}(\mathbf{p}_{\min})$ is the minimal element of the power-rate image. ///

Three observations drop out of this result. The first observation is that this result determines when the set of feasible vectors is non-empty— \mathcal{P}_C is not empty provided the external SINR γ_X is sufficiently small to force the spectral radius $\rho(F) < 1$. The second observation is that the gain matrix G sets an upper limit on the user-defined SINR or, equivalently, the requested network throughput.

Example 4 (External SINR Constraints) *The narrowband channel gain matrix is*

$$G = \begin{matrix} & \begin{matrix} \text{TX-1} & \text{TX-2} \end{matrix} \\ \begin{matrix} \text{RX-1} \\ \text{RX-2} \end{matrix} & \begin{bmatrix} g_{11} & g_{12} \\ g_{21} & g_{22} \end{bmatrix} \end{matrix} = \begin{bmatrix} -72 & -75 \\ -71 & -80 \end{bmatrix} \text{ [dB]}.$$

The matrix

$$F := G_S^{-1} \Gamma_X G_I = \begin{bmatrix} 0 & g_{11}^{-1} \gamma_{X,1} g_{12} \\ g_{22}^{-1} \gamma_{X,2} g_{21} & 0 \end{bmatrix}; \quad \Gamma_X := \text{diag}(\gamma_X)$$

satisfies the inequality $\rho(F) < 1$ if and only if the requested SINR's are bounded by the excess SINR γ_E as follows:

$$\gamma_{X,1} \gamma_{X,2} < \frac{g_{11} g_{22}}{g_{12} g_{21}} =: \gamma_E.$$

Figure 35 illustrates how the excess SINR γ_E constrains the external SINR's to the following lower half-plane:

$$\gamma_{X,1} + \gamma_{X,2} < (-72 - 80) - (-71 - 75) = -6 = \gamma_E \text{ [dB]}.$$

In this example, positive SINR (dB) cannot simultaneously exist on both links because the excess SINR is negative: $\gamma_E = -6$ dB. Figure 35 also shows that the gain matrix also constrains the operational throughput—simultaneous throughput in excess of 0.6 Mbps cannot be delivered on both links.

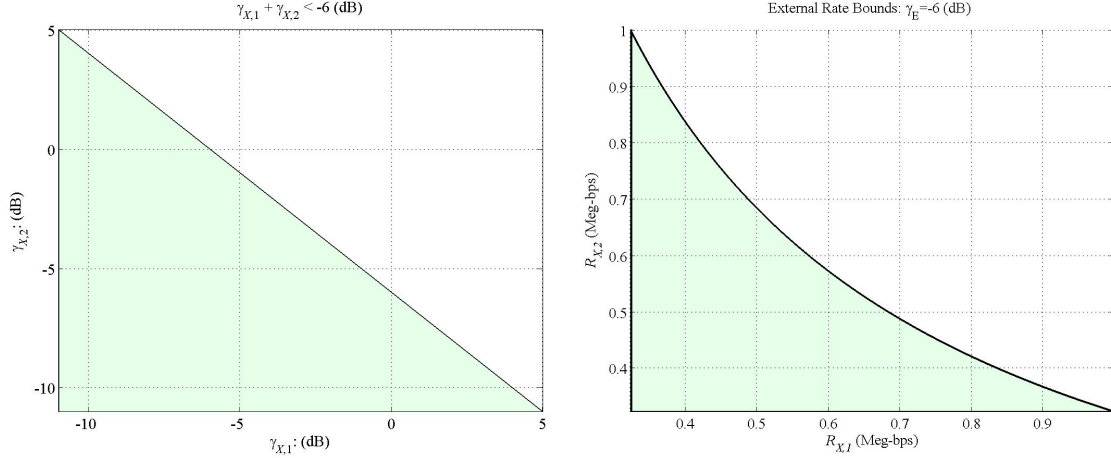


Figure 35. External constraints: SINR (left panel), throughput (right panel).

For networks with more than two links ($L > 2$), the spectral radius bound $\rho(F) < 1$ yields an upper bound on the QoS:

$$\gamma_{X,l} \leq \frac{g_{ll}}{\|G_I\|}.$$

This upper bound has the physical meaning that the requested SINR $\gamma_{X,l}$ cannot exceed the channel's SIR.

The third observation that drops out of Theorem 3 is that the set of feasible vectors \mathcal{P}_C is parameterized by the closed, convex cone \mathbb{R}_+^L under the affine mapping:

$$\mathcal{P}_C = \mathbf{p}_{\min} + (I - F)^{-1} \mathbb{R}_+^L.$$

The image of this convex cone under the (nearly) convex power-rate mapping \mathfrak{N} is power-rate (PR) image for the static channel:

$$\mathfrak{N}(\mathcal{P}_C) = \mathfrak{N}(\mathbf{p}_{\min} + (I - F)^{-1} \mathbb{R}_+^L).$$

The *Pareto front* of this power-rate image $\mathfrak{N}(\mathcal{P}_C)$ is the best possible trade-off between power and throughput under the external SINR constraint.

Example 5 (Power-Rate Image) *The narrowband channel gain matrix is*

$$G = \begin{matrix} & \begin{matrix} \text{TX-1} & \text{TX-2} \end{matrix} \\ \begin{matrix} \text{RX-1} \\ \text{RX-2} \end{matrix} & \begin{bmatrix} g_{11} & g_{12} \\ g_{21} & g_{22} \end{bmatrix} \end{matrix} = \begin{bmatrix} -72 & -75 \\ -71 & -80 \end{bmatrix} \text{ [dB]}$$

from Example 4. Select a feasible control vector less than the maximal SINR:

$$\gamma_X = \begin{bmatrix} +0 \\ -10 \end{bmatrix} \prec \begin{bmatrix} +3 \\ -9 \end{bmatrix} \text{ [dB]}.$$

With the 1-MHz noise set to $p_N = -116$ dBW and rounding, the network performance image $\mathfrak{N}(\mathcal{P}_C)$ of the feasible power vectors

$$\mathbf{p}_C = \mathbf{p}_{\min} + (I - F)^{-1} \mathbf{p}_K; \quad \mathbf{p}_K \in \mathbb{R}_+^2.$$

Figure 36 shows the grid for $\mathbf{p}_K \in \mathbb{R}_+^2$ (Left Panel) mapping into cone of feasible vectors: $\mathbf{p}_K \mapsto \mathbf{p}_C$ (Right Panel). Figure 37 reports how this grid of feasible vectors maps into the network performance image: $\mathbf{p}_C \mapsto \mathfrak{N}(\mathbf{p}_C)$.

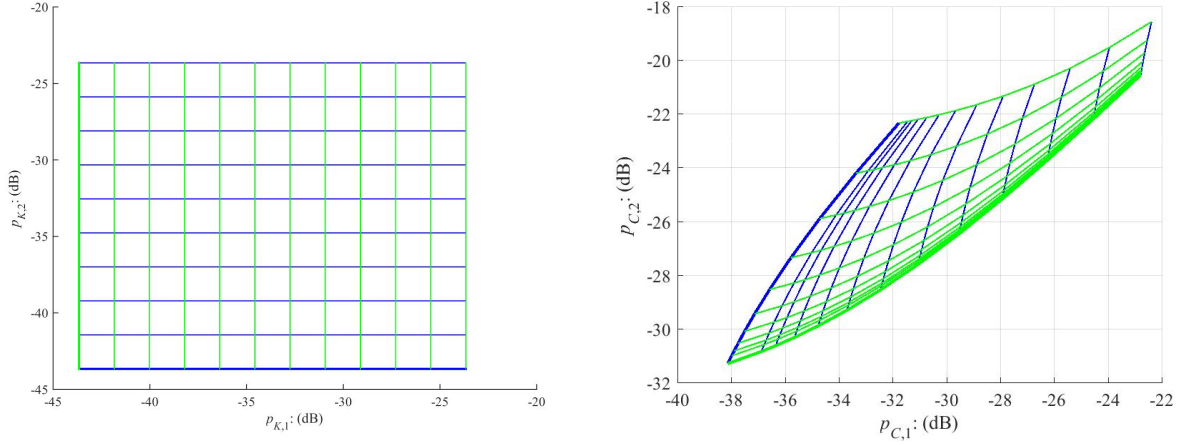


Figure 36. Pre-image of the cone of feasible power vectors: $\mathbf{p}_K \in \mathbb{R}_+^2$ (left panel). Cone of feasible power vectors: $\mathbf{p}_C = \mathbf{p}_{\min} + (I - F)^{-1} \mathbf{p}_K$; The grid is distorted by the dB scaling (right panel).

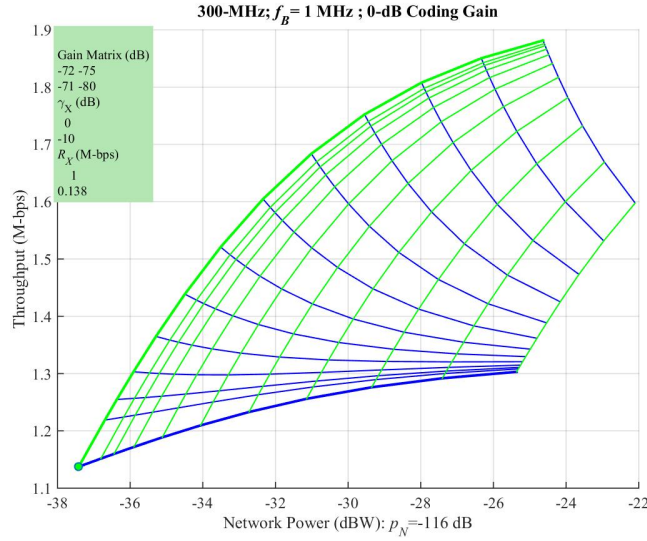


Figure 37. Network performance image; urban noise at 300 MHz is $p_N = -116$ dBW; the green dot is $\mathfrak{N}(\mathbf{p}_{\min})$. The heavy green line is the Pareto front.

Mapping the cone of feasible power vectors $\mathcal{P}_C \rightarrow \mathfrak{N}(\mathcal{P}_C)$ generates the network image in Figure 37. This image shows the Pareto front is a function of the total network power for this two-link network. The next result verifies this observation is true for networks with L links (Appendix A contains the proof).

Theorem 4 (Pareto Front) *Let $G \in \mathbb{R}^{L \times L}$ be a constant gain matrix for L links. Let $G_S = \text{diag}(G)$ and $G_I = G - G_S$ denote the signal and interference matrices, respectively. Let $\mathbf{p}_N \in \mathbb{R}_+^L$ denote the constant and strictly positive noise vector. Let $\gamma_M : \mathbb{R}^L \rightarrow \mathbb{R}^L$ denote the measured SINR vector*

$$\gamma_M(\mathbf{p}_C) = \frac{G_S \mathbf{p}_C}{\mathbf{p}_N + G_I \mathbf{p}_C}.$$

Let γ_X denote a constant, user-specified SINR constraint vector with $\Gamma_X = \text{diag}(\gamma_X)$ sufficiently large to force the feedback matrix $F = G_S^{-1} \Gamma_X G_I$ to have the spectral radius strictly less than unity. The feasible control vectors are the positive cone

$$\mathcal{P}_C = \mathbf{p}_{\min} + (I - F)^{-1} \mathbb{R}_+^L \subseteq \mathbb{R}_+^L$$

with vertex $\mathbf{p}_{\min} = (I - F)^{-1} G_S^{-1} \Gamma_X \mathbf{p}_N$. The Pareto front of the network's power-rate image $\mathfrak{N}(\mathcal{P}_C)$ is determined by maximizing the throughput for each slice of the total network power:

$$p_\Sigma \mapsto \max \left\{ R_\Sigma(\mathbf{p}_C) : \mathbf{p}_C \in \mathcal{P}_C; p_\Sigma = \mathbf{1}^\top \mathbf{p}_C \right\}.$$

The next example shows the effect of increasing noise on the power rate image. Roughly speaking, increasing noise simply shifts the image—the Pareto front does not change.

Example 6 (Power-Rate Image & Noise) *The narrowband channel gain matrix is*

$$G = \begin{matrix} & \begin{matrix} \text{TX-1} & \text{TX-2} \end{matrix} \\ \begin{matrix} \text{RX-1} \\ \text{RX-2} \end{matrix} & \begin{bmatrix} g_{11} & g_{12} \\ g_{21} & g_{22} \end{bmatrix} \end{matrix} = \begin{bmatrix} -72 & -75 \\ -71 & -80 \end{bmatrix} \text{ [dB]}$$

from Example 4. Select a feasible control vector less than the maximal SINR:

$$\gamma_X = \begin{bmatrix} +0 \\ -10 \end{bmatrix} \dot{<} \begin{bmatrix} +3 \\ -9 \end{bmatrix} \text{ [dB]}.$$

Figure 38 shows the network performance image when the noise increases to $p_N = -80$ dBW.

Example 6 also shows that increasing the noise power only shifts the performance image in power. The reason is that measured SINR constraint scales with the noise:

$$\gamma_M(\mathbf{p}_N; \mathbf{p}) := \frac{G_S \mathbf{p}}{\mathbf{p}_N + G_I \mathbf{p}}.$$

If $\mathbf{p} \in \mathbb{R}^L$ meets the SINR constraint: $\gamma_X \dot{\leq} \gamma_M(\mathbf{p}_N; \mathbf{p})$ then $\alpha \mathbf{p}$ meets the SINR constraint under the scaled noise:

$$\gamma_X \dot{\leq} \gamma_M(\alpha \mathbf{p}_N; \alpha \mathbf{p}); \quad (\alpha > 0).$$

The throughput will not change under the joint scaling of the power and noise:

$$R_b(\mathbf{p}_N; \mathbf{p}) = f_B \sum_{l=1}^L \log_2(1 + \gamma_M(\mathbf{p}_N; \mathbf{p})) = R_b(\mathbf{p}_N; \mathbf{p}).$$

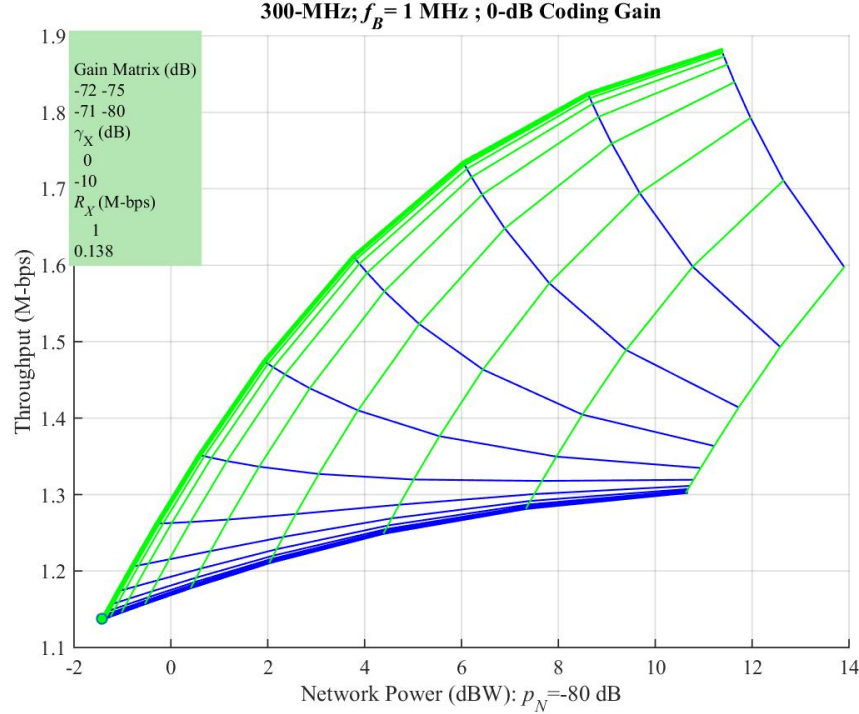


Figure 38. Network performance image; noise power $p_N = -80$ dB; the green dot is $\mathfrak{N}(\mathbf{p}_{\min})$. The Pareto front is the upper green line.

Consequently, the network performance image will only shift in power

$$\mathfrak{N}(\gamma_X; \alpha \mathbf{p}_N) = \begin{bmatrix} 0 \\ \alpha \end{bmatrix} + \mathfrak{N}(\gamma_X; \mathbf{p}_N)$$

with the noise scaling—provided the power is plotted in dB. However, coding gain does change the power-rate image.

Example 7 (Power-Rate Image & Coding Gain) A 10-dB coding gain is modeled by reducing the off-diagonal terms by a factor of 10. Therefore, the narrowband channel gain matrix from Example 4 is modified as

$$G = \begin{matrix} & \begin{matrix} \text{TX-1} & \text{TX-2} \end{matrix} \\ \begin{matrix} \text{RX-1} \\ \text{RX-2} \end{matrix} & \begin{bmatrix} g_{11} & g_{12} \\ g_{21} & g_{22} \end{bmatrix} \end{matrix} = \begin{bmatrix} -72 & -85 \\ -81 & -80 \end{bmatrix} \text{ [dB]}.$$

The feasible control vector is less than the maximal SINR and is selected to be the same as the preceding examples.

$$\gamma_X = \begin{bmatrix} +0 \\ -10 \end{bmatrix} \prec \begin{bmatrix} +13 \\ +1 \end{bmatrix} \text{ [dB]}.$$

With the 1-MHz noise set to $p_N = -116$ dBW, the network performance image

$$\mathfrak{N}(\mathcal{P}_C) = \mathfrak{N}(\mathbf{p}_{\min} + (I - F)^{-1} \mathbb{R}_+^2)$$

is illustrated in Figure 39. The green dot is $\mathfrak{N}(\mathbf{p}_{\min})$. The noise power in each link is $p_N = -116$ dBW. Figure 40 shows the corresponding plot when the noise power is increased to $p_N = -80$ dBW. Comparison of Figures 39 and 40 verifies that scaling the noise simply shifts the performance image.

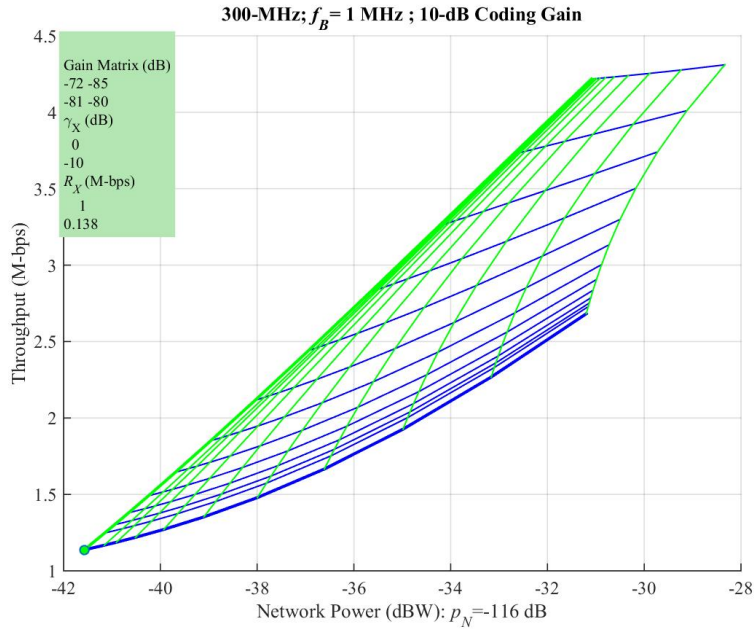


Figure 39. Network performance image at 300 MHz with 10-dB coding gain; urban noise is $p_N = -116$ dB. The Pareto front is the upper green line.

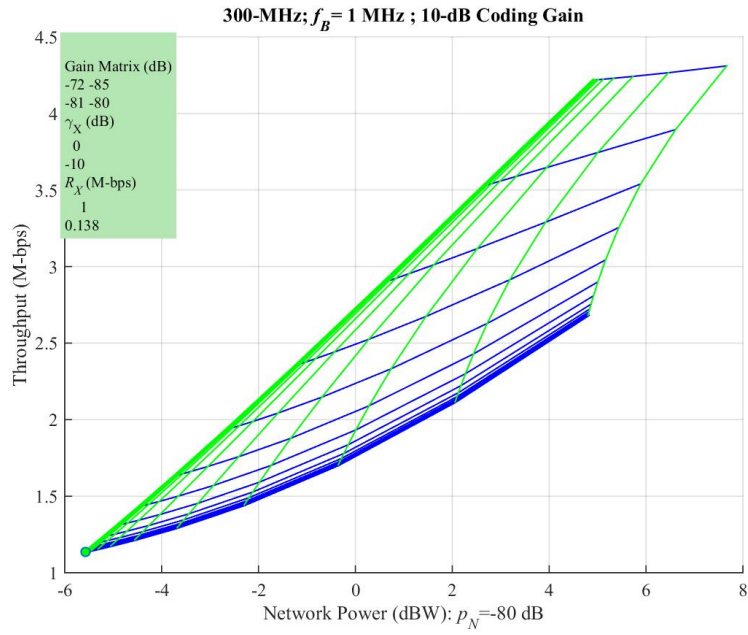


Figure 40. Network performance image at 300 MHz with 10-dB coding gain; noise power is -80 dB. The Pareto front is the upper green line.

The final example extends the range of the feasible power control vectors and equalizes the SINR requirement to -5 dB on both links. Figure 41 shows that the network mapping “twists” the cone on the power control vector. Standard optimizers seeking the Pareto front may get trapped in the fold and converge to a local minimum.

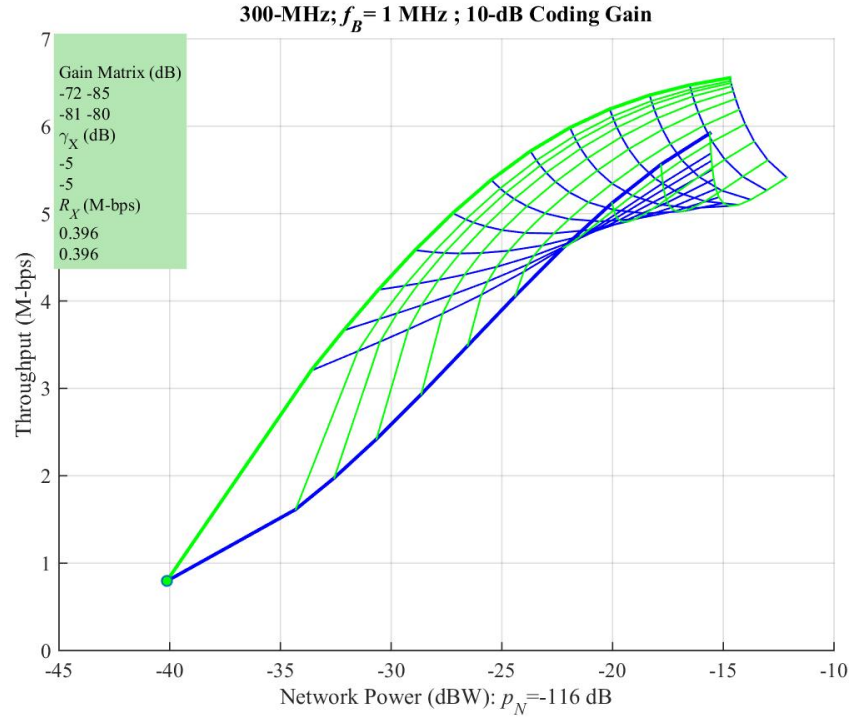


Figure 41. Network performance image at 300-MHz with 10-dB coding gain; noise power is -116 dB; the QoS is reduced to $\gamma_X = -5$ dB or $R_X = 0.396$ Mbps. The Pareto front is the upper green line.

8. POWER-RATE BASELINES FOR MOBILE TWO-LINK SCENARIOS

Figure 42 is a top view of the suburban Rosslyn, VA, showing two links:

- Link 1 is fixed with both TX-1 and RX-1 at the street level
- Link 2 has a TX-2 traveling along the x -axis track while RX-2 is on the roof of an 80-meter building.

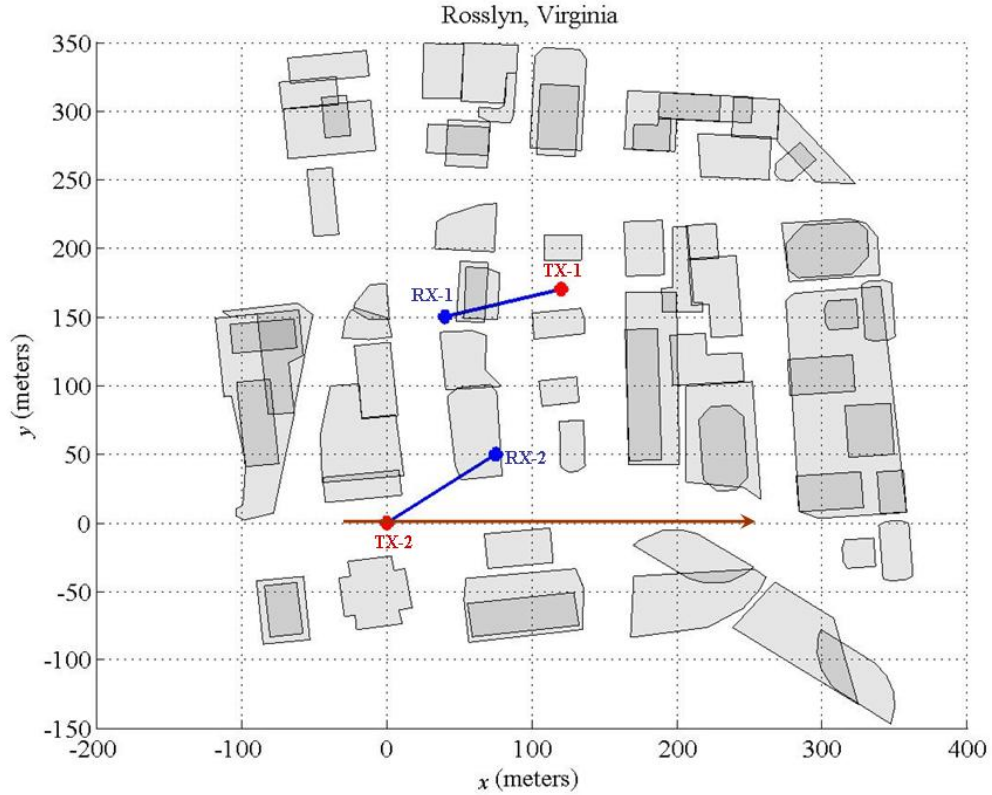


Figure 42. Top view of Rosslyn, VA, showing Link 1 (TX-1 to RX-1) and Link 2 (TX-2 to RX-2); TX-2 travels along the x -axis track.

The narrowband gain matrix for this network has the form

$$G(x) = \begin{matrix} & \begin{matrix} \text{TX-1} & \text{TX-2} \end{matrix} \\ \begin{matrix} \text{RX-1} \\ \text{RX-2} \end{matrix} & \begin{bmatrix} g_{11} & g_{12}(x) \\ g_{21} & g_{22}(x) \end{bmatrix} \end{matrix} \quad [\text{dB}],$$

where the first column is constant. Thus, this scenario is the smallest possible mobile network to benchmark the wireless power control algorithms.

Section 8.1 shows the mobile network operating along the track at 300 MHz using 1 watt per transmitter. The interference from Link 1 almost shuts down Link 2. The mismatch between the links makes Quality-of-Service challenging—the minimal throughput over the 25-kHz bandwidth is 11 bps. Section 8.2 shows that a 10-dB coding gain mitigates some of this QoS shortfall. Both transmitters each

broadcast 1 watt but the coding gain delivers throughput exceeding 25 kbps over 63% of the track. The natural question asks: *what is the payoff of using wireless power control?* Section 8.3 determines the *best possible* payoff for wireless power control using the following assumptions:

- Centralized control
- Channel matrix is perfectly known
- Noise power is perfectly known
- No delay.

That is, this network is equipped with an all-knowing “genie.” This genie is tasked to allocate power to maximize throughput while maintaining a minimal QoS of 25 kbps. Best possible power allocation boosts this QoS to cover 74% of the track. Section 8.4 moves the frequency region to 1.9 GHz and increases the bandwidth to 1 MHz.

8.1 MOBILE TRACK AT 300 MHZ: FIXED POWER

Figure 43 plots the gain matrix generated by TX-2 moving along the x axis:

$$G(x) = \begin{matrix} & \begin{matrix} \text{TX-1} & \text{TX-2} \end{matrix} \\ \begin{matrix} \text{RX-1} \\ \text{RX-2} \end{matrix} & \begin{bmatrix} g_{11} & g_{12}(x) \\ g_{21} & g_{22}(x) \end{bmatrix} \end{matrix} = \begin{bmatrix} -72 & g_{12}(x) \\ -71 & g_{22}(x) \end{bmatrix} \text{ [dB]}.$$

These gains exhibit multiple phenomena: the characteristic lobing when only a few strong rays interfere, the sharp jumps when a street “unblocks” a transmitter, and the large-scale trends caused by distance.

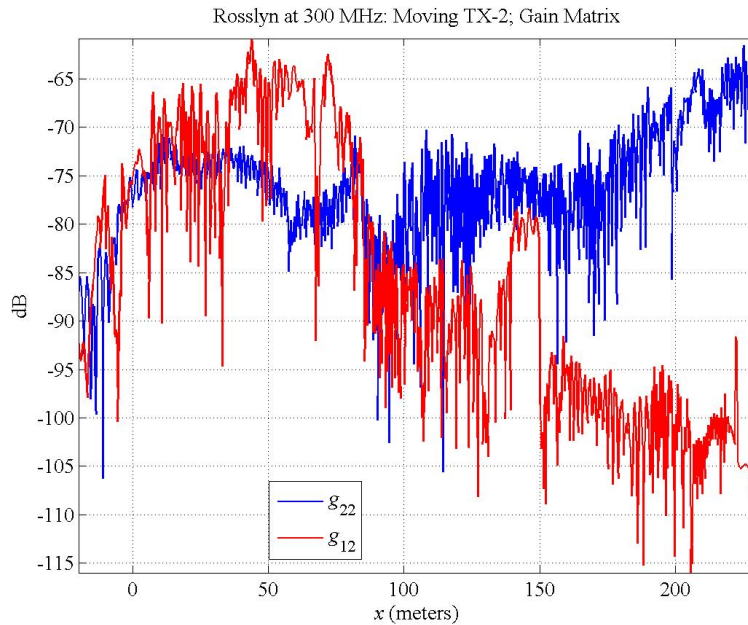


Figure 43. Gain matrix for moving TX-2 traveling along the x axis.

The signal gain for Link 1 falls below the interference for $10 < x < 75$: $g_{11} = -72$ dB; $g_{12}(x) \geq -70$. If equal transmit powers are employed and the noise is relatively small, Link 1 is interference-limited over this region and has negative SINR. The signal gain for Link 2 is comparable to interference over the whole track: $g_{22} \approx g_{21}(x)$. If equal transmit powers are employed and the noise is relatively small, Link 2 will have a relatively flat SINR around 0 dB. Figure 44 reports the SINR produced by moving TX-2 along the x -axis assuming:

- Unit power: $\mathbf{p}_T = [1; 1]^T$ watts
- Low noise: $p_N = -133$ dBW.

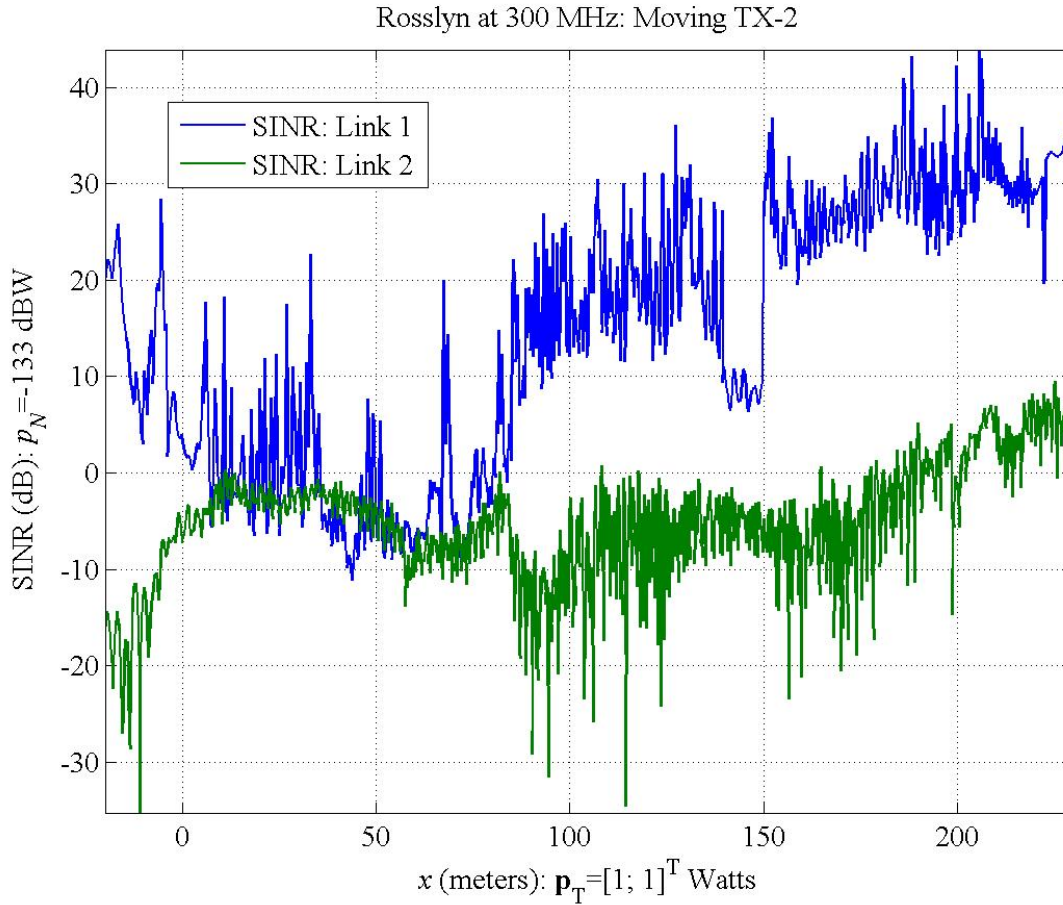


Figure 44. SINR for moving TX-2 traveling along the x -axis.

For Link 1, the power from TX-1 to RX-1 is not changing, so the “S” in SINR is constant, whereas the power from TX-2 is rolling off as TX-2 travels along the x -axis ($g_{12}(x) \downarrow$). Consequently, RX-1 receives less interference from TX-2 and shows an increase in the measured SINR $\gamma_{M,1}$. For Link 2, the power from TX-1 to RX-2 is not changing, so the “I” in SINR is constant, whereas the power from TX-2 is increasing as TX-2 travels along the x -axis ($g_{22}(x) \uparrow$). Consequently, RX-2 receives more signal from TX-2 and also shows an increase in the measured SINR $\gamma_{M,2}$.

Figure 45 reports the throughput produced by moving TX-2 along the x axis assuming:

- Unit power: $\mathbf{p}_T = [1; 1]^T$ watts
- Low noise: $p_N = -133$ dBW
- Bandwidth: $f_B = 25$ kHz.

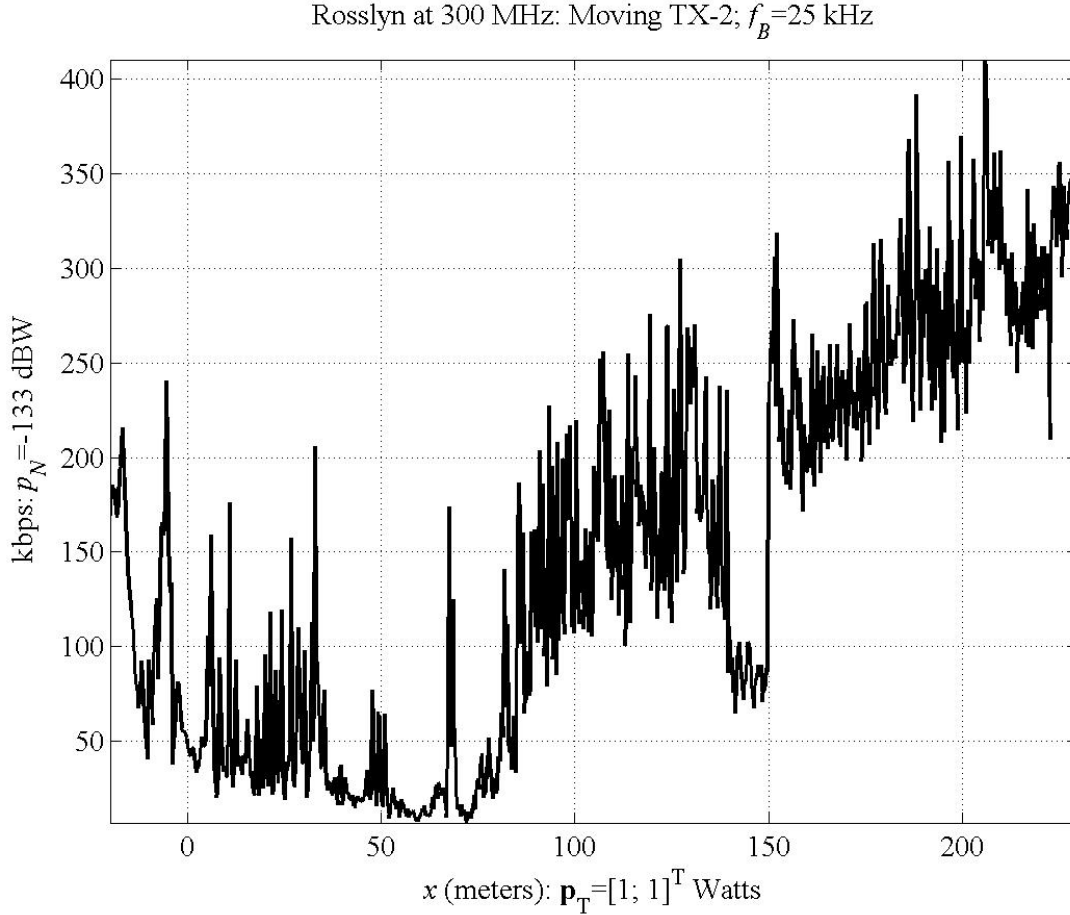


Figure 45. Throughput for moving TX-2 traveling along the x axis.

The throughput is totally dominated by Link 1 because the SINR of Link 1 typically exceeds the SINR of Link 2 by 10 dB. Giving equal power to both links “throws away” total throughput because of the SINR disparity between the links. Therefore, throughput would be maximized if *all* the power was allocated to Link 1 and Link 2 was shut down. If a minimal quality-of-service (QoS) is enforced, throughput is reduced because the throughput in Link 1 is traded to boost throughput in Link 2. That is, the measured SINR’s must exceed the external SINR: $\gamma_M \geq \gamma_X$. Indeed, Figure 45 uses an *implicit* external SINR: $\gamma_X = -35$ [dB] set by Figure 44. The QoS is equivalent to throughput:

$$R_b = f_B \log_2(1 + \gamma) \Leftrightarrow \gamma = 2^{R_b/f_B} - 1.$$

Therefore, $\gamma_X = -35$ dB implies an equivalent QoS $R_X = 11.4$ [bps], assuming a bandwidth $f_B = 25$ kHz. Coding gain can mitigate this low QoS.

8.2 MOBILE TRACK AT 300 MHZ: CODING GAIN

This section applies a 10-dB coding gain to the gain matrix:

$$G(x) = \begin{matrix} & \text{TX-1} & \text{TX-2} \\ \begin{matrix} \text{RX-1} \\ \text{RX-2} \end{matrix} & \begin{bmatrix} g_{11} & g_C^{-1} g_{12}(x) \\ g_C^{-1} g_{21} & g_{22}(x) \end{bmatrix} \end{matrix} = \begin{bmatrix} -72 & g_{12}(x) - 10 \\ -81 & g_{22}(x) \end{bmatrix} \quad [\text{dB}]$$

to get a network with practical link values. Figure 46 reports the SINR produced by moving TX-2 along the x axis assuming:

- Unit power: $\mathbf{p}_T = [1; 1]^T$ watts
- High noise: $p_N = -80$ dBW
- Coding gain: $g_C = 10$ dB.

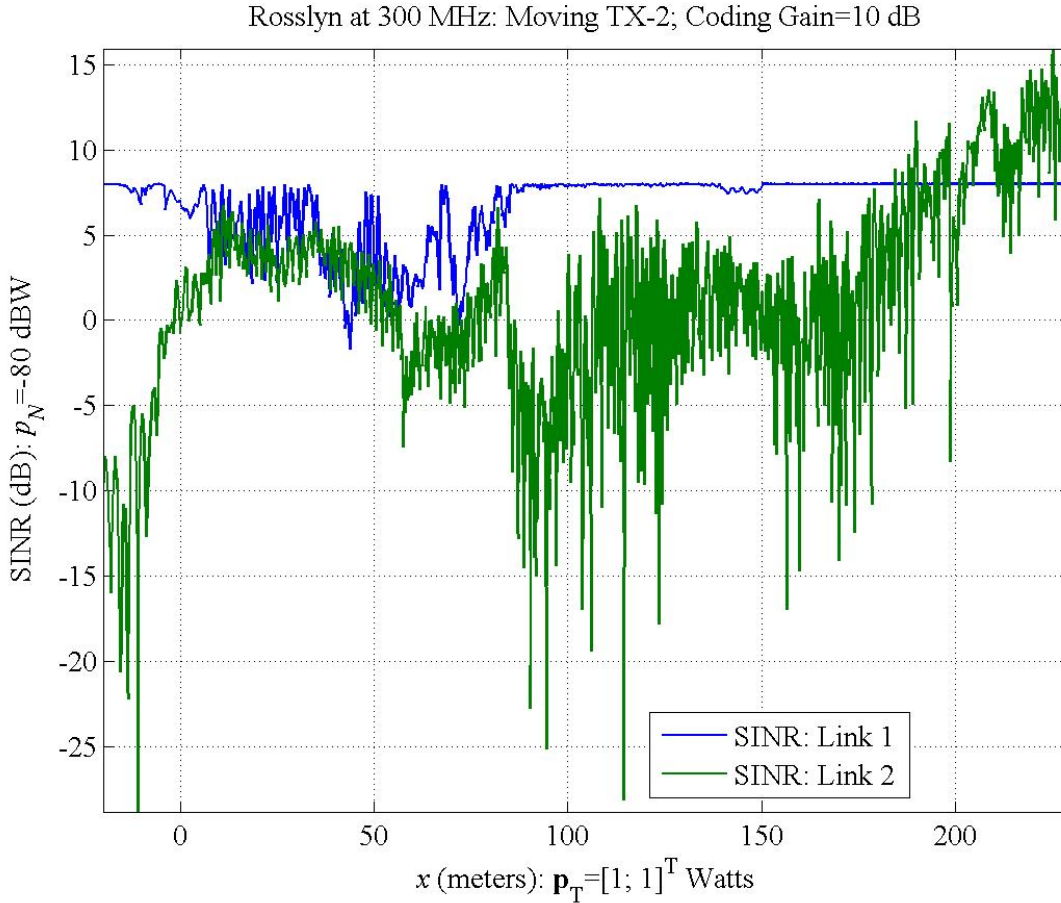


Figure 46. SINR for moving TX-2 traveling along the x axis; 10-dB coding gain.

The first observation is that SINR on both links are comparable because of the coding gain. The second observation is that “flat” areas for the SINR on Link 1 are caused by the coding gain and the increased noise: $p_N = -80$ dBW. The noise was increased because of the current limitations on the Pareto-front

code. Figure 43 showed that Link 1 was interference limited for $10 < x < 75$ (meters). Exterior to this region, the interference is smaller than the noise: Over this region,

$$g_C^{-1} g_{12}(x) p_{T,2} = -10 - 100 + 0 \ll -80 = p_N \quad [\text{dB}].$$

In this low-interference region, the SINR on Link 1 is almost constant as shown in Figure 46:

$$\gamma_{M,1}(x) = \frac{g_{11} p_{T,1}}{p_N + g_C^{-1} g_{12}(x) p_{T,2}} \approx \frac{g_{11}}{p_N} p_{T,1} = -72 + 80 + 0 = 8 \quad [\text{dB}]$$

Figure 47 reports the throughput determined by the noise and coding gain. The figure suggests that the large throughput on Link 1 can be traded to boost the smaller throughput on Link 2 so that a minimal rate of 25 kbps is possible.

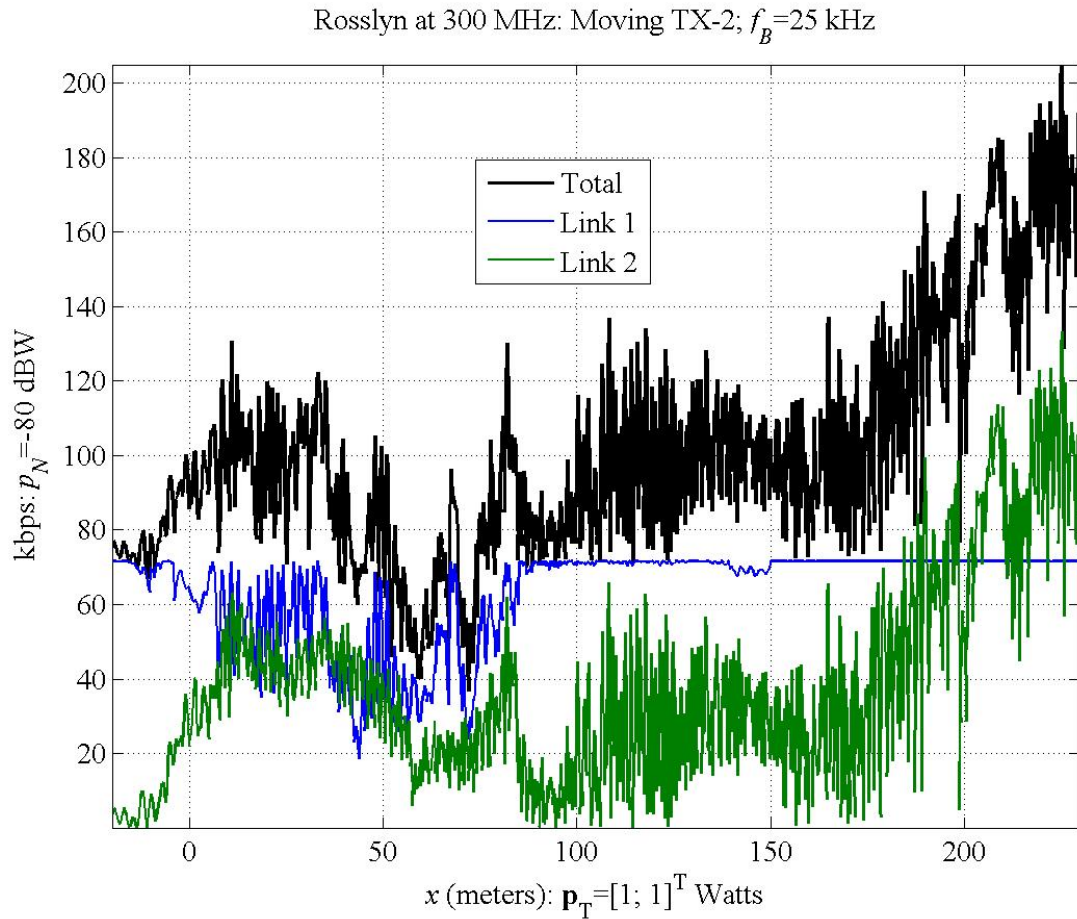


Figure 47. Throughput for moving TX-2 traveling along the x axis; Rosslyn at 300 MHz; 10-dB coding gain.

8.3 MOBILE TRACK AT 300 MHZ: BEST PERFORMANCE

Figure 48 reports the throughput for this noise, coding gain, and the explicit QoS constraint:

$$R_{b,X} = 25 \text{ [kbps]} \iff \gamma_X = 0 \text{ [dB]}.$$

The figure reports “Link” increased from 63% to 74%. The percentages arise when both Link 1 and Link 2 exceed the explicit QoS constraint over the track. The first number comes from Figure 46 where the power was equally divided between both links. This implicit design delivered 25-kbps links over 63% of the track. The second number is delivered by a Pareto-front optimizer that distributes the the power between the two links. Specifically, the network “genie” seeks to maximize throughput by allocating total power while guaranteeing QoS:

$$\max \left\{ R_{\Sigma}(\mathbf{p}) = \sum_{l=1}^L R_{b,l}(\mathbf{p}) \right\} \quad \text{subject to} \quad \begin{cases} \text{Positive powers:} & \mathbf{p} \geq \mathbf{0} \\ \text{Fixed network power:} & p_{\Sigma} = \sum_{l=1}^L p_l \\ \text{QoS:} & R_{b,l}(\mathbf{p}) \geq R_{b,X} \end{cases}.$$

This is the power-constrained optimization of Table 10. Figure 48 is produced by applying this Pareto-front optimizer to each gain matrix along the track. This best possible centralized control delivered the 25-kbps links over 74% of the track. Little difference is observed between this optimized throughput and the equal-power design—except the parts of the track where the Pareto-front optimizer delivers the improved QoS.

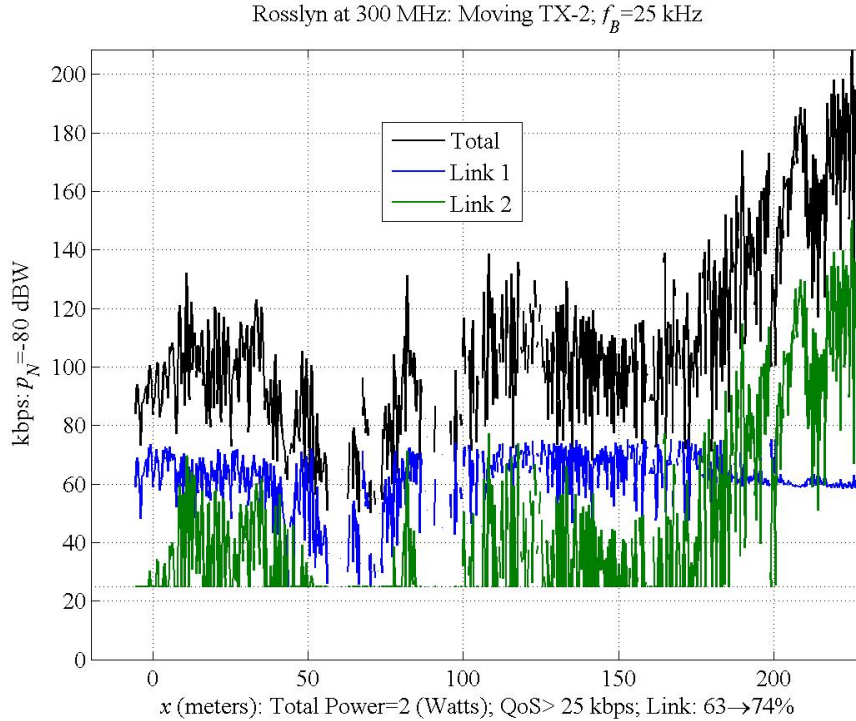


Figure 48. Throughput for moving TX-2 traveling along the x axis; 10-dB coding gain; $\text{QoS} \geq 25$ kbps. The “blanks” in the plot mark where QoS failed.

8.4 MOBILE TRACK AT 1.9 GHZ

Figure 43 plots the gain matrix produced by moving TX-2 along the x axis operating at 1.9 GHz:

$$G(x) = \begin{bmatrix} -102 & g_{12}(x) \\ -93 & g_{22}(x) \end{bmatrix} \quad [\text{dB}].$$

In comparison to the propagation at 300 MHz as seen in Figure 43, the channel matrix has the same general form: RX-1 is still jammed by TX-2 at the beginning of the track and then is blocked by buildings once TX-2 moves past $x = 75$ meters; there is the characteristic “2-ray” lobing on both $g_{22}(x)$ and $g_{12}(x)$ at the end of the track.

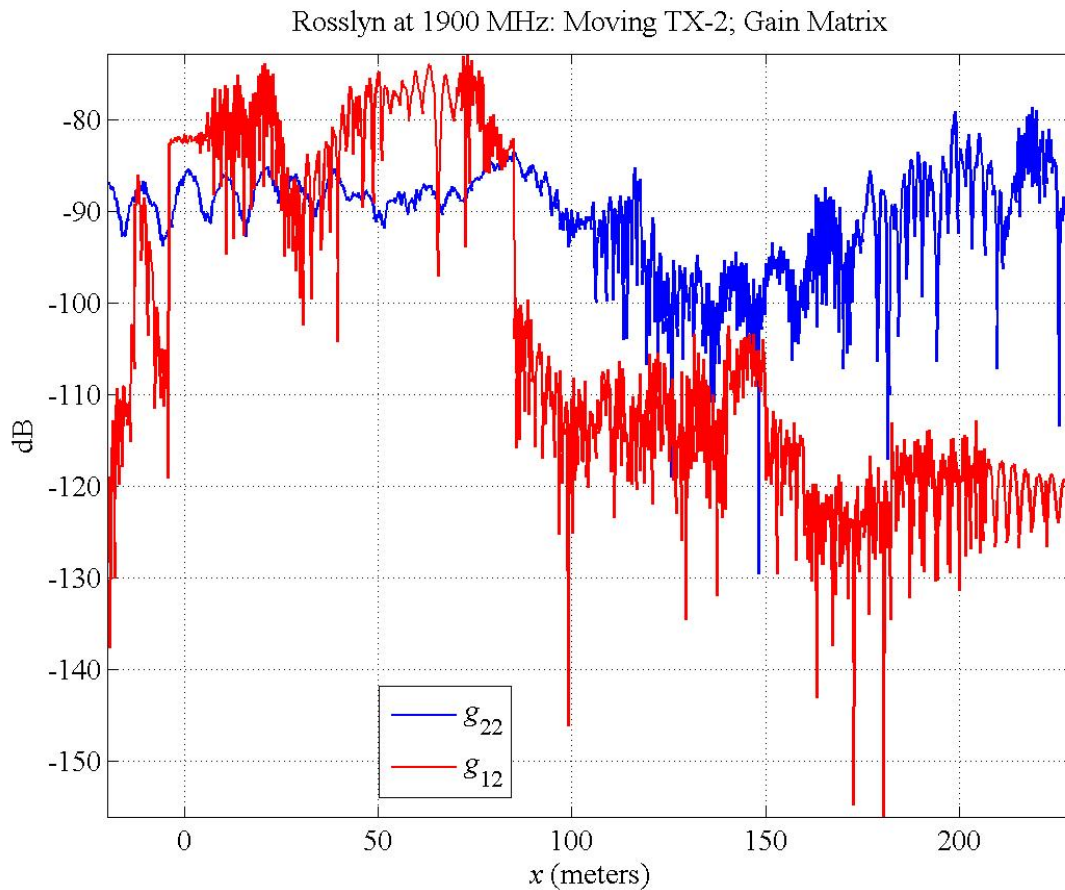


Figure 49. Gain matrix for moving TX-2 traveling along the x axis; Rosslyn at 1.9 GHz.

Figure 50 shows the SINR on both link in a high-noise environment. Suburban noise is typically $p_N = -149$ dBW at 1.9 GHz over the $f_B = 1.3$ -MHz band. These simulations use $p_N = -100$ dBW for a high-noise environment. Link 1 shows the flat regions characteristic of high noise: the noise dominates the interference ($g_{12}p_{T,2} \ll p_N$) so that

$$\begin{aligned}\gamma_{M,1}(x) &= \frac{g_{11}p_{T,1}}{p_N + g_{12}(x)p_{T,2}} \\ &\approx \frac{g_{11}p_{T,1}}{p_N} \\ &= g_{11} + p_{T,1} - p_N \quad [\text{dB}] \\ &= -102 + 0 + 100 \quad [\text{dB}] \\ &= -2 \quad [\text{dB}].\end{aligned}$$

These flat regions will control the link QoS.

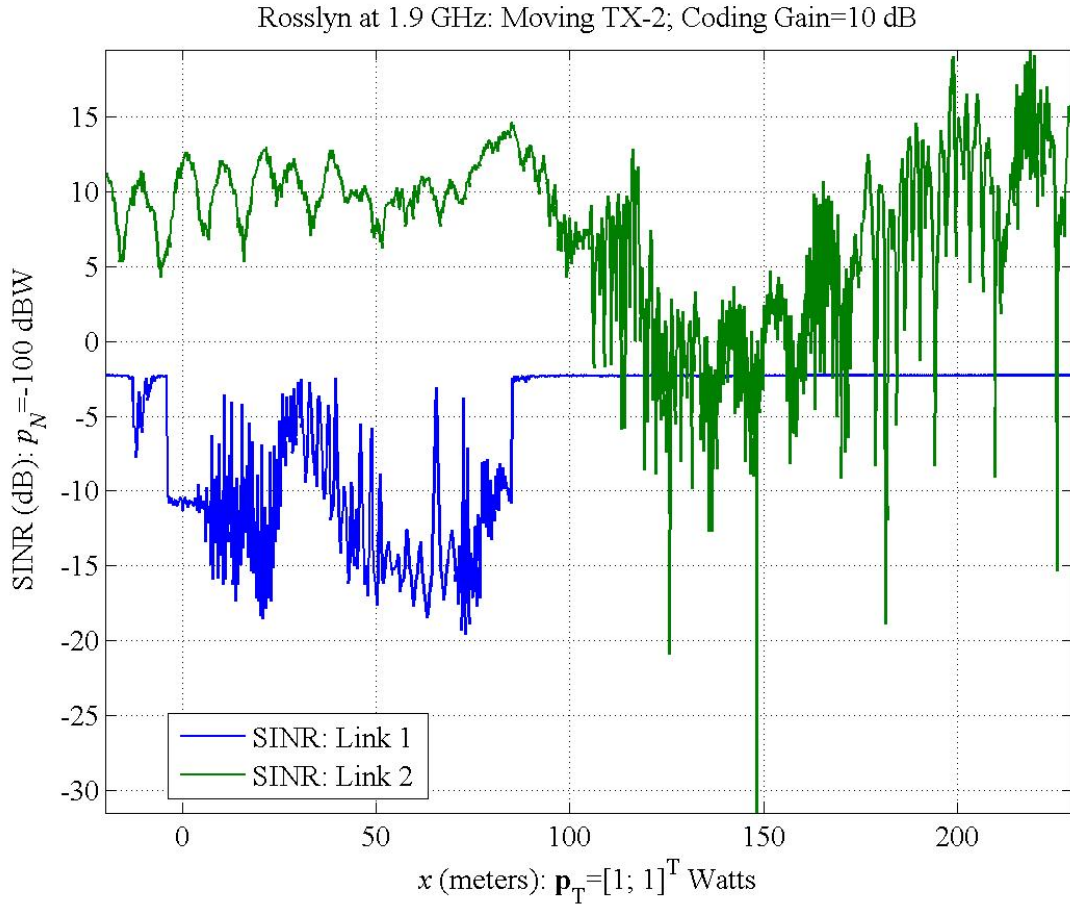


Figure 50. SINR for moving TX-2 traveling along the x axis; Rosslyn at 1.9 GHz; coding gain $g_C = 10$ dB; equal power $p_{T,1} = p_{T,2} = 1$ watt.

Figure 51 shows the throughput for this high-noise simulation. The network throughput is dominated by Link 2 because Link 1 is limited by the high noise: $R_{b,1}(x) < 1$ Mbps in the noise-limited regions.

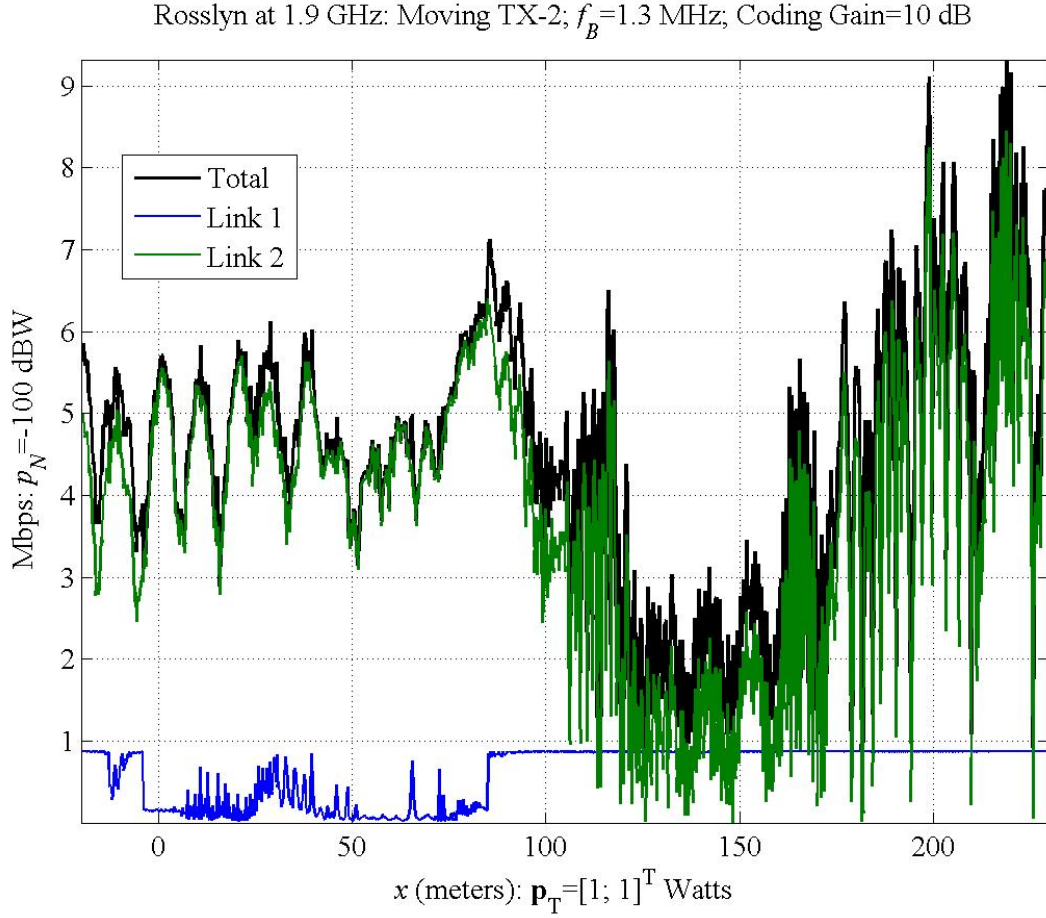


Figure 51. Equal-power throughput for moving TX-2 traveling along the x axis; Rosslyn at 1.9 GHz; coding gain $g_C = 10$ dB; equal power $p_{T,1} = p_{T,2} = 1$ watt.

Figure 52 illustrates best possible power control the QoS requirement—each link carries at least $R_{b,X} = 1$ Mbps. This best possible control assumes a network “genie” maximizing throughput subject to QoS constraints. At each point on the track, the genie solves

$$\max \left\{ R_{\Sigma}(\mathbf{p}) = \sum_{l=1}^L R_{b,l}(\mathbf{p}) \right\} \quad \text{subject to} \quad \begin{cases} \text{Positive powers:} & \mathbf{p} \succeq \mathbf{0} \\ \text{Fixed network power:} & p_{\Sigma} = \sum_{l=1}^L p_l \\ \text{QoS:} & R_{b,l}(\mathbf{p}) \geq R_{b,X} \end{cases} .$$

In the equal power case of Figure 51, Link 1 never meets the QoS: $R_{b,1}(x) < R_{b,X}$ so that QoS is 0% along the track. However, Figure 51 suggests that some of the throughput on Link 2 can be traded to boost the throughput on Link 1 to meet the QoS. Figure 52 reports that this trading is possible—QoS is delivered over 54% of the track. The plot shows where the QoS is delivered by plotting both links and their total. The blank regions mark where the QoS requirements cannot be met.

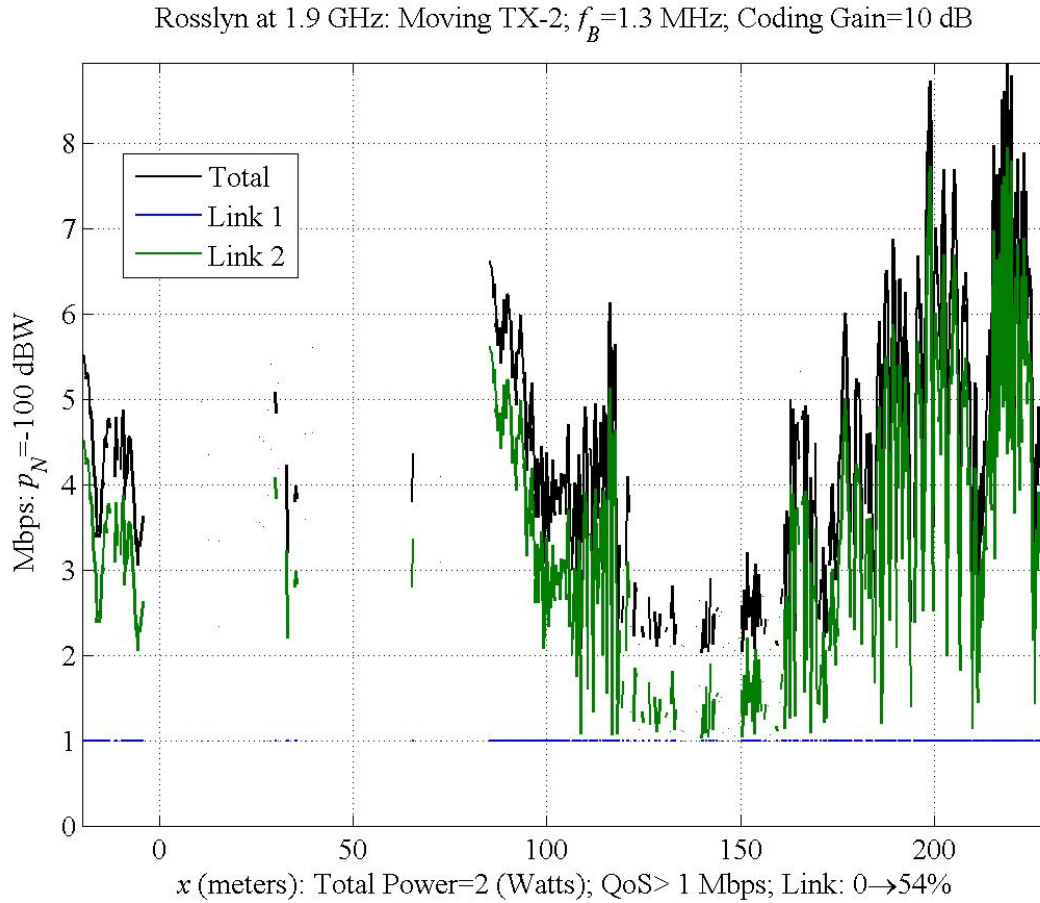


Figure 52. Throughput for moving TX-2 traveling along the x axis; Rosslyn at 1.9 GHz; coding gain $g_C = 10$ dB; $QoS \geq R_{b,X} = 1$ Mbps. The “blanks” in the plot mark where QoS failed.

9. THE FOSCHINI & MILJANIC (FM) ALGORITHM

In 1993, Foschini & Miljanic produced their seminal paper on distributed wireless power control [22]: *A Simple Distributed Autonomous Power Control Algorithm and Its Convergence*. Their excellent solution characterized the existence of solutions (feasibility), introduced the concept of the all-knowing network “genie,” computed the global solution via their network “genie” inverting a matrix, delivered a distributed solution based on a simple feedback ODE whose discrete version is equivalent matrix inversion via the power method, and finally, analyzed convergence and stepsize control. Assume the *feedback matrix* of Equation (13)

$$F = G_S^{-1} \Gamma_X G_I; \quad \Gamma_X := \text{diag}(\gamma_X)$$

has spectral radius strictly less than unity: $\rho(F) < 1$. The minimum power allocation $\mathbf{p}_{\min} \geq \mathbf{0}$ that meets the QoS $\gamma_M(\mathbf{p}_{\min}) = \gamma_X$ is [22, Equation 12]:

$$\mathbf{p}_{\min} := (I - F)^{-1} G_S^{-1} \Gamma_X \mathbf{p}_N.$$

The power method for matrix inversion produces the sequence of power control vectors $\mathbf{p}_C(t)$ at update times t_n [22, Equation 14]:

$$\begin{aligned} \mathbf{p}_{\min} \leftarrow \mathbf{p}_C(t_{n+1}) &= G_S^{-1} \Gamma_X \mathbf{p}_N + F \mathbf{p}(t_n) \\ &= G_S^{-1} \Gamma_X \mathbf{p}_N + G_S^{-1} \Gamma_X G_I \mathbf{p}_C(t_n) \\ &= G_S^{-1} \Gamma_X \{ \mathbf{p}_N + G_I \mathbf{p}_C(t_n) \} \\ &= G_S^{-1} \Gamma_X \{ \mathbf{p}_N + \mathbf{p}_I(t_n) \}. \end{aligned}$$

The power method is distributed along each link $l = 1, \dots, L$ because [22, Equation 2]:

$$\begin{aligned} p_{\min,l} \leftarrow p_{C,l}(t_{n+1}) &= g_{ll}^{-1} \gamma_{X,l} \{ p_{N,l} + p_{I,l}(t_n) \} \\ &= p_{C,l}(t_n) \gamma_{X,l} \frac{p_{N,l} + p_{I,l}(t_n)}{g_{ll} p_{C,l}(t_n)} \\ &= p_{C,l}(t_n) \frac{\gamma_{X,l}}{\gamma_{M,l}(t_n)}. \end{aligned}$$

That is, each receiver only has to measure its SINR to implement the update. If the wireless network has a system delay, the receiver measures the delayed SINR:

$$\gamma_{M,l}(t_n) = \frac{g_{ll}(t_n) p_{C,l}(t_n - \tau)}{p_{N,l}(t_n) + \sum_{m \neq l} g_{lm}(t_n) p_{C,m}(t_n - \tau)}.$$

The following algorithm includes a stepsize β to control stability using these time-delayed updates.

Algorithm 1 (FM) [22]: [27], [79] *Select the step size $0 \leq \beta < 1$.*

FM-1 *The network is synchronized and all updates occur at the start of each frame: $t_n := nt_F$.*

FM-2 *Each receiver measures its SINR at the start of each frame:*

$$\gamma_{M,l}(t_n) = \frac{g_{ll}(t_n) p_{C,l}(t_n - \tau)}{p_{N,l}(t_n) + \sum_{m \neq l} g_{lm}(t_n) p_{C,m}(t_n - \tau)}.$$

FM-3 The power is updated for the frame $[t_n, t_{n+1})$ as

$$p_{C,l}(t_{n+1}) = p_{C,l}(t_n) \left\{ \frac{\gamma_{X,l}}{\gamma_{M,l}(t_n)} \right\}^{1-\beta}.$$

FM-4 The control power is limited

$$p_{C,l}(t_{n+1}) = [p_{\min} \leq p_{C,l}(t_{n+1}) \leq p_{\max}].$$

9.1 FM TRACK PERFORMANCE AT 1.9 GHZ

Table 11 lists the RF parameters of the gain matrix, the SINR, and the updating of the wireless control algorithms. These parameters are outside the control of the FM algorithm.

Table 11. RF and system parameters.

Variable	Value	Description
f_C	1.9 GHz	Carrier frequency
f_B	1.3 MHz	Bandwidth
p_N	-149 dBW	RF noise
τ	0.9 ms	System delay
g_C	10 dB	Coding gain
t_F	1 ms	Frame duration

Table 12 lists the inputs to the FM algorithm. The QoS is 1 Mbps on both links; the frame duration $t_F = 1$ ms sets the power control update rate.

Table 12. FM parameters.

Variable	Value	Description
$R_{b,X}$	1 Mbps	Throughput
p_{\min}	0 W	Minimum power
p_{\max}	1 W	Maximum power
p_{ini}	10 μ W	Initial power
β	0.9	Stepsize

Figure 53 reports the power and the rate for the network during the time TX-2 travels along the x -axis track. The upper panel compares the power on each link computed by the distributed FM algorithm. The lower panel compares throughput on each link. Although the coding gain is $g_C = 10$ dB, throughput is set using the capacity: $R_b(t) = f_B \times \log_2(1 + \gamma_M(t))$. On the average, the FM algorithm delivers rates at $R_{b,X} = 1$ Mbps.

Figure 54 assesses the average performance of the FM algorithm as the mobile network travels along the x axis. Also plotted is an upper bound on performance given by the Exact FM algorithm (description forthcoming). Neither algorithm meets the QoS constraints at every point of the x -axis track. Therefore, the next two paragraphs detail how the average performances account for this loss of QoS.

FM Algorithm: let \mathcal{Q}_{FM} index those frames meeting the QoS:

$$\mathcal{Q}_{\text{FM}} := \{n \in [1 : N_F] - 1 : \gamma_M(\mathbf{p}_C; t_n) \geq \gamma_X; t_n = nt_F\},$$

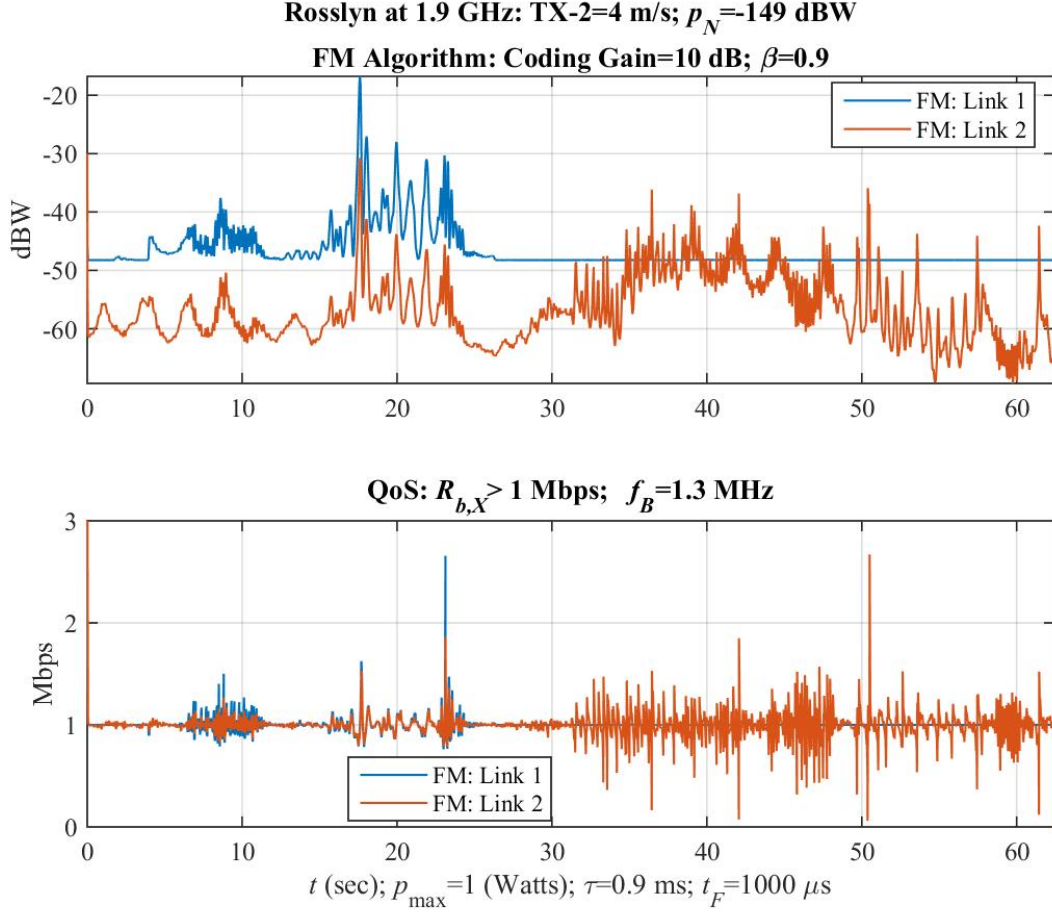


Figure 53. FM performance for mobile TX-2 traveling along the x axis; $R_{b,X} = 1$ Mbps; delay $\tau = 0.9$ ms; frame duration $t_F = 1$ ms; $f_C = 1.9$ GHz; Coding gain $g_C = 10$ dB. Upper Panel: Link power along the track; Lower Panel: Link rates along the track.

where N_F is the number of frames along the track. Averaging the rates over the entire track mixes the unsuccessful QoS transmission with the transmission that met the QoS. This mixing is problematic when one link dominates. Indeed, Section 8.4 reports Link 1 always delivers high rates although Link 2 was almost shut down—total throughput is high while the QoS is never satisfied. Therefore, the average network rate is defined as average rate only when the network delivers QoS:

$$R_{\text{FM}} = \frac{1}{N_F} \sum_{n \in Q_{\text{FM}}} \mathbf{1}^T \begin{bmatrix} R_{b,1}(t_n) \\ R_{b,2}(t_n) \end{bmatrix}.$$

The FM algorithm always transmits minimum power regardless of the QoS. Therefore, network power is the average power:

$$p_{\text{FM}} = \frac{1}{N_F} \sum_{n=0}^{N_F-1} \mathbf{1}^T \mathbf{p}_C(t_n).$$

Exact FM Algorithm: This algorithm operates with zero system delay, global network knowledge (i.e., the gain matrix), and solves for minimum power \mathbf{p}_{\min} meeting the QoS constraints. Not every position on the

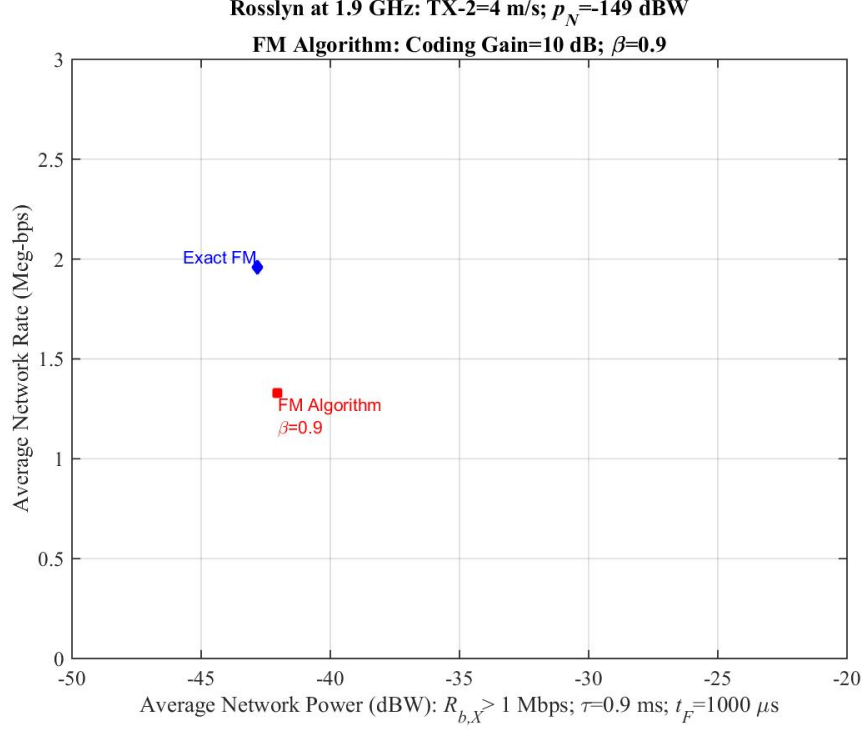


Figure 54. FM performance averaged over x -axis track; QoS $R_{b,X} = 1$ Mbps; delay $\tau = 0.9$ ms; frame rate $t_F = 1$ ms; $f_C = 1.9$ GHz; coding gain $g_C = 10$ dB.

x -axis track admits a solution. Let \mathcal{Q}_{XFM} index those frames meeting the QoS:

$$\mathcal{Q}_{\text{XFM}} := \{n \in [1 : N_F] - 1 : \gamma_M(\mathbf{p}_{\min}(t_n)) \stackrel{\circ}{\geq} \gamma_X; t_n = nt_F\}.$$

Define the average network rate as the average rate only when the network delivers the QoS:

$$R_{\text{XFM}} = \frac{1}{N_t} \sum_{n \in \mathcal{Q}_{\text{XFM}}} \mathbf{1}^\top \begin{bmatrix} R_{b,X} \\ R_{b,X} \end{bmatrix} = 2R_{b,X} \times \frac{|\mathcal{Q}_{\text{XFM}}|}{N_t}.$$

The average power used by the exact FM algorithm is defined as

$$p_{\text{XFM}} = \frac{1}{|\mathcal{Q}_{\text{XFM}}|} \sum_{n \in \mathcal{Q}_{\text{XFM}}} \mathbf{1}^\top \mathbf{p}_{\min}(t_n).$$

Indeed, the power is not defined when the QoS constraint cannot be satisfied.

Discussion: Figure 54 reports that the FM algorithm delivers approximately 70% of the best possible average network rate using only slightly more power. The FM delivers this performance against the system delay of $\tau = 0.9$ ms and no global knowledge of the network—each link uses only information measured at its receiver. The next section assesses the FM algorithm against larger system delays.

9.2 FM PERFORMANCE AGAINST DELAY

Figure 55 compares the average power-rate performance for the Exact FM algorithm to the distributed FM algorithm. As in the Section 9.1, the exact FM algorithm operates with zero system delay, global network knowledge, and solves for minimum power \mathbf{p}_{\min} that meets the QoS constraints. Therefore, its performance has not shifted from Figure 54. The distributed FM algorithm “hangs” tight until the delay exceeds 8 ms. At 9 ms delay, the power jumps by 15 dB. Increasing delays in excess of 9 ms force the power to increase while the throughput rolls off. Thus, the FM algorithm has a delay threshold—exceeding this threshold incurs system collapse.

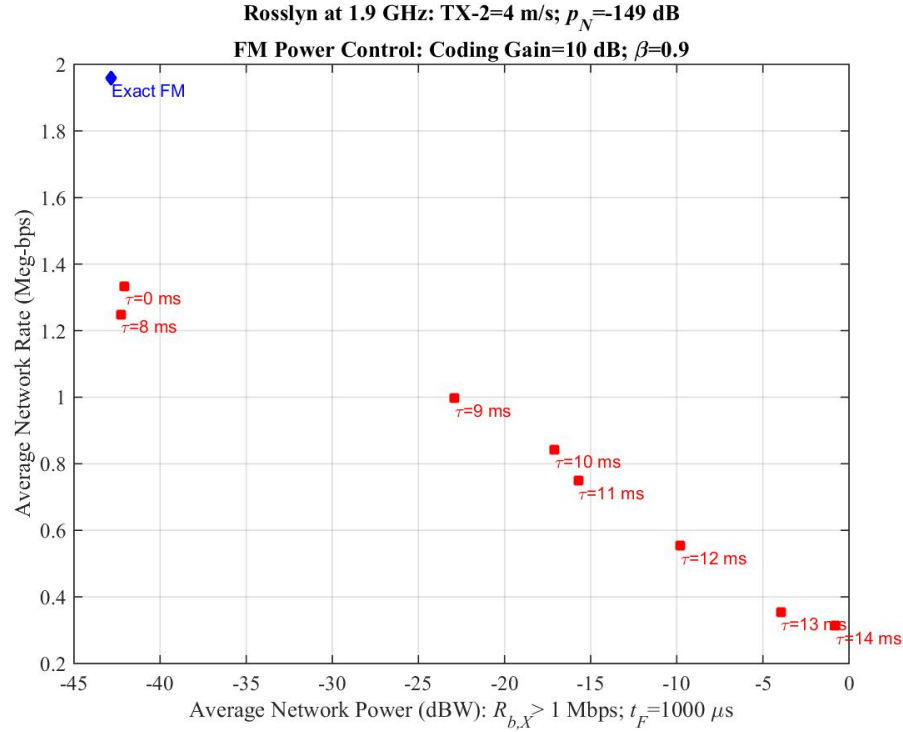


Figure 55. Average FM performance along x -axis track as a function of delay; $R_{b,X} = 1$ Mbps; frame rate $t_F = 1$ ms; $f_C = 1.9$ GHz; coding gain $g_C = 10$ dB.

10. THE MODPC ALGORITHM

An excellent generalization of the FM algorithm is the Multiple Objective Distributed Power Control Algorithm (MODPC) of Elumrati, Jäntti, and Koivo [20]. Their generalization starts with the observation that the FM algorithm seeks to minimize power subject to the QoS constraint. The MODPC algorithm [20]:

“... treats the QoS requirement as another objective for the power control and [produces] a fully distributed method for solving the multiobjective power optimization problem.”

Their derivation starts by weighting the excess power and the QoS gap [20, Equation 3]:

$$e_l(t) = \lambda_P |p_{C,l}(t) - p_{\min,l}| + \lambda_Q |\gamma_{X,l} - \gamma_{M,l}(t)|$$

on each link $l = 1, \dots, L$ where the power weight $\lambda_P \geq 0$ and the QoS weight $\lambda_Q \geq 0$ have unit sum: $\lambda_P + \lambda_Q = 1$. The global cost function sums these errors over the entire network and a time window [20, Equation 5]:

$$J(\mathbf{p}_C; t_n) = \sum_{l=1}^L \sum_{m=0}^M a_F^m e_l(t_{n-m})^2.$$

Here the time window looks back M time slots and weights the past with the “forgetting” factor $a_F > 0$. A power control is sought that minimizes this global cost function. Under the 1-tap AR assumption of the power evolution [20, Equation 6], the MODPC power control is [20, Equation 7]

$$p_{C,l}(t_{n+1}) = p_{C,l}(t_n) \frac{\lambda_P p_{\min} + \lambda_Q \gamma_X}{\lambda_P p_{C,l}(t_n) + \lambda_Q \gamma_{M,l}(t_n)}.$$

This solution contains the FM algorithm for $\lambda_P = 0$:

$$p_{C,l}(t_{n+1}) = p_{C,l}(t_n) \frac{\gamma_X}{\gamma_{M,l}(t_n)}.$$

Our interest lies at the other extreme when $\lambda_P \approx 1$. Elumrati, Jäntti, and Koivo [20] analyzed convergence, and compared their MODPC algorithm against the DPC algorithm [23], FM algorithm [22], and a second-order power control (SOPC) algorithm [35]. The remainder of this section ranks the following MODPC algorithm against the exact FM algorithm.

Algorithm 2 (MODPC) Select the step size $0 \leq \beta < 1$ and non-negative weights λ_P and λ_Q such that $\lambda_P + \lambda_Q = 1$.

MODPC-1 The network is synchronized and all updates occur at the start of each frame: $t_n := nt_F$.

MODPC-2 Each receiver measures its SINR at the start of each frame:

$$\gamma_{M,l}(t_n) = \frac{g_{ll}(t_n) p_{C,l}(t_n - \tau)}{p_{N,l}(t_n) + \sum_{m \neq l} g_{lm}(t_n) p_{C,m}(t_n - \tau)}.$$

MODPC-3 The power is updated for the frame $[t_n, t_{n+1})$ as [20, Equation 7]

$$p_{C,l}(t_{n+1}) = p_{C,l}(t_n) \left\{ \frac{\lambda_P p_{\min} + \lambda_Q \gamma_X}{\lambda_P p_{C,l}(t_n) + \lambda_Q \gamma_{M,l}(t_n)} \right\}^{1-\beta}.$$

MODPC-4 The control power is limited

$$p_{C,l}(t_{n+1}) = [p_{\min} \leq p_{C,l}(t_{n+1}) \leq p_{\max}].$$

10.1 MODPC TRACK PERFORMANCE AT 1.9 GHZ

Table 11 lists the RF and system parameters common to all the algorithms. These parameters are outside the control of the MODPC algorithm. Table 13 lists the inputs to the MODPC algorithm. The QoS is 1 Mbps on both links; the frame duration $t_F = 1$ ms sets the power control update rate. The table sets MODPC algorithm far from the FM algorithm by selecting the weights $\lambda_P = 0.99$ and $\lambda_Q = 0.01$, This weighting minimizes power at the expense of QoS.

Table 13. MODPC parameters.

Variable	Value	Description
$R_{b,X}$	1 Mbps	Throughput
p_{\min}	0 W	Minimum power
p_{\max}	1 W	Maximum power
p_{ini}	10 μ W	Initial power
β	0.9	Stepsize
λ_P	0.99	Power weight
λ_Q	0.01	QoS weight

Figure 56 reports the power and the rate for the network during the time TX-2 travels along the x -axis track. The upper panel compares the power on each link computed by the MODPC algorithm. The lower panel compares throughput on each link. Although the coding gain is $g_C = 10$ dB, throughput is set using the capacity: $R_b(t) = f_B \times \log_2(1 + \gamma_M(t))$. On the average, the MODPC algorithm delivers rates at $R_{b,X} = 1$ Mbps. The average performance of the MODPC algorithm is assessed in Figure 57.

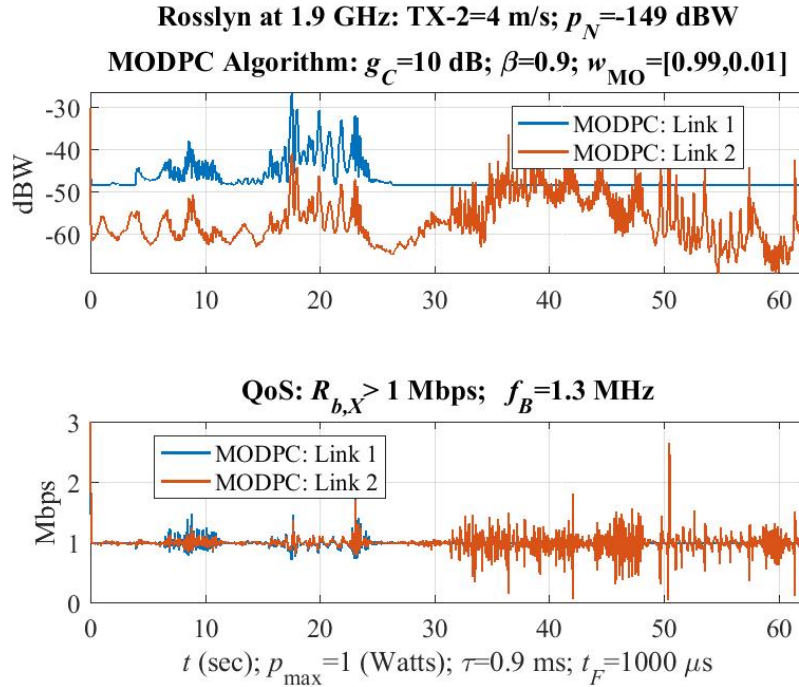


Figure 56. MODPC performance for mobile TX-2 traveling along the x axis; $R_{b,X} = 1$ Mbps; delay $\tau = 0.9$ ms; frame duration $t_F = 1$ ms; $f_C = 1.9$ GHz; coding gain $g_C = 10$ dB. Upper Panel: Link power along the track; Lower Panel: Link rates along the track.

Figure 57 assesses the average performance of the MODPC algorithm as the mobile network travels along the x axis. Also plotted is an upper bound on performance given by the Exact FM algorithm (description forthcoming). Neither algorithm meets the QoS constraints at every point of the x -axis track. Therefore, the next two paragraphs detail how the average performances account for this loss of QoS.

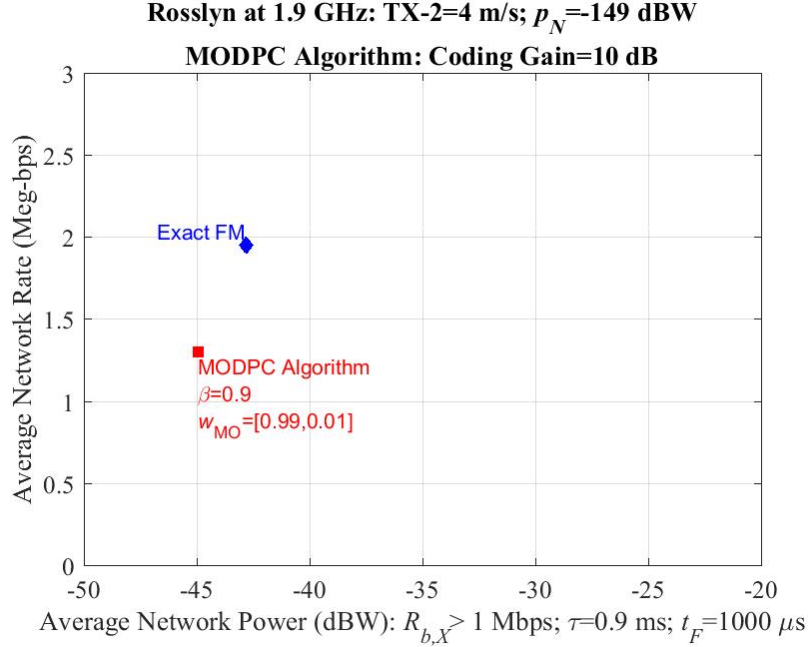


Figure 57. MODPC performance averaged over x -axis track; QoS $R_{b,X} = 1$ Mbps; delay $\tau = 0.9$ ms; frame duration $t_F = 1$ ms; $f_C = 1.9$ GHz; coding gain $g_C = 10$ dB.

MODPC Algorithm: let \mathcal{Q}_{MO} index those frames meeting the QoS:

$$\mathcal{Q}_{MO} := \{n \in [1 : N_F] - 1 : \gamma_M(\mathbf{p}_C; t_n) \geq \gamma_X; t_n = nt_F\},$$

where N_F is the number of frames along the track. Averaging the rates over the entire track mixes the unsuccessful QoS transmission with the transmission that met the QoS. This mixing is problematic when one link dominates. Indeed, Section 8.4 reports Link 1 always delivers high rates although Link 2 was almost shut down—total throughput is high while the QoS is never satisfied. Therefore, the average network rate is defined as average rate only when the network delivers QoS:

$$R_{MO} = \frac{1}{N_F} \sum_{n \in \mathcal{Q}_{MO}} \mathbf{1}^T \begin{bmatrix} R_{b,1}(t_n) \\ R_{b,2}(t_n) \end{bmatrix}.$$

The MODPC algorithm always transmits minimum power regardless of the QoS. Therefore, network power is the average power:

$$p_{MO} = \frac{1}{N_F} \sum_{n=0}^{N_F-1} \mathbf{1}^T \mathbf{p}_C(t_n).$$

Exact FM Algorithm: This algorithm operates with zero system delay, global network knowledge (i.e., the gain matrix), and solves for minimum power \mathbf{p}_{min} meeting the QoS constraints. Not every position on the x -axis track admits a solution. Let \mathcal{Q}_{XFM} index those frames meeting the QoS:

$$\mathcal{Q}_{XFM} := \{n \in [1 : N_F] - 1 : \gamma_M(\mathbf{p}_{min}(t_n)) \geq \gamma_X; t_n = nt_F\}.$$

Define the average network rate as the average rate only when the network delivers the QoS:

$$R_{\text{XFM}} = \frac{1}{N_t} \sum_{n \in \mathcal{Q}_{\text{XFM}}} \mathbf{1}^\top \begin{bmatrix} R_{b,X} \\ R_{b,X} \end{bmatrix} = 2R_{b,X} \times \frac{Q_{\text{XFM}}}{N_t}.$$

The average power used by the exact FM algorithm is defined as

$$p_{\text{XFM}} = \frac{1}{|Q_{\text{XFM}}|} \sum_{n \in Q_{\text{XFM}}} \mathbf{1}^\top \mathbf{p}_{\min}(t_n).$$

Indeed, the power is not defined when the QoS constraint cannot be satisfied.

Discussion: Figure 57 reports that the MODPC algorithm delivers approximately 70% of the best possible average network rate while using less power. The MODPEC algorithm delivers this performance against the system delay of $\tau = 0.9$ ms and no global knowledge of the network—each link uses only information measured at its receiver. The next section assesses the MODPC algorithm against larger system delays.

10.2 MODPC PERFORMANCE AGAINST DELAY

Figure 58 compares the average power-rate performance for the Exact FM algorithm to the MODPC algorithm. As in Section 10.1, the exact FM algorithm operates with zero system delay, global network knowledge, and solves for minimum power \mathbf{p}_{\min} that meets the QoS constraints. Therefore, its performance has not shifted from Figure 57. The MODPC algorithm “hangs” tight until the delay exceeds 8 ms. At 9 ms delay, the power jumps by approximately 12 dB. Increasing delays past 9 ms further increase the power while throughput rolls off. Thus, the MODPC algorithm has a delay threshold—exceeding this threshold incurs system collapse.

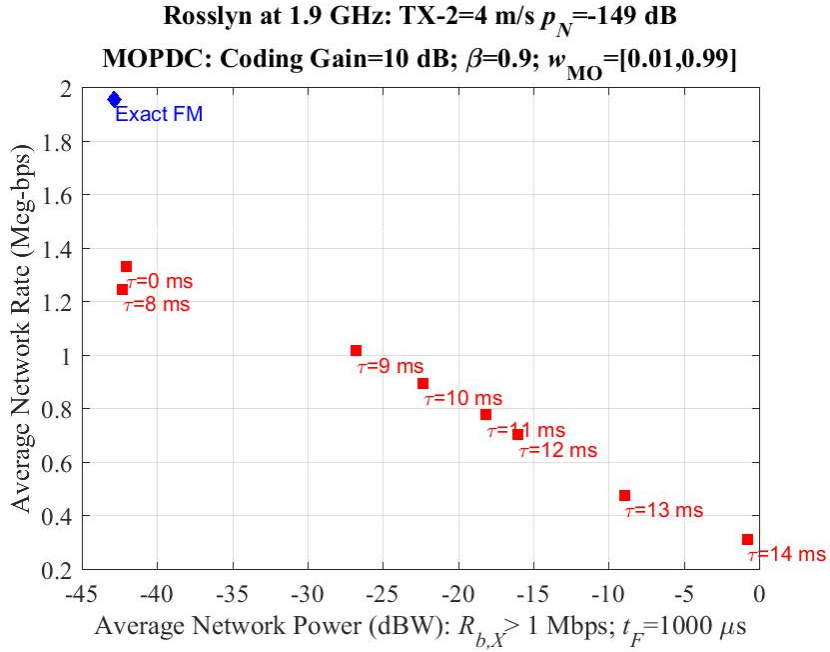


Figure 58. Average MODPC performance along x -axis track as a function of delay; $R_{b,X} = 1$ Mbps; frame duration $t_F = 1$ ms; $f_C = 1.9$ GHz; coding gain $g_C = 10$ dB.

11. INTERLUDE: KALMAN FILTER

A typical Kalman filter for wireless power control usually tracks the SINR and update power based on the predicted SINR. This section reviews the Kalman filter estimating the SINR. The resulting state space is used in the forthcoming sections.

11.1 KALMAN FILTER MODELS

The simplest discrete Kalman filter is based on the state-space model and measurement model of the form [5, Equations 4.2.1–4.2.2]: for $t = 0, 1, \dots$

$$\mathbf{x}_{t+1} = \Phi_t \mathbf{x}_t + \mathbf{w}_t, \quad (18)$$

$$\mathbf{z}_t = H_t \mathbf{x}_t + \mathbf{v}_t. \quad (19)$$

The transition matrix Φ_t and the measurement matrix H_t are known. The *process* noise $\{\mathbf{w}_t\}$ and the *measurement* noise $\{\mathbf{v}_t\}$ are zero-mean, white noise sequences that are uncorrelated and also uncorrelated with the initial state [5, Equations 4.2.3–4.2.5]

$$E \left[\begin{bmatrix} \mathbf{x}_0 \\ \mathbf{w}_t \\ \mathbf{v}_t \end{bmatrix} \begin{bmatrix} \mathbf{x}_0^\top & \mathbf{w}_t^\top & \mathbf{v}_t^\top \end{bmatrix} \right] = \begin{bmatrix} P_0 & 0 & 0 \\ 0 & \delta_{t,t'} Q_t & 0 \\ 0 & 0 & \delta_{t,t'} R_t \end{bmatrix}. \quad (20)$$

The process covariance $\{Q_t\}$ and the noise covariance $\{R_t\}$ are known. The Kalman filter advances the prior estimate of the state $\hat{\mathbf{x}}_t^-$ and the prior estimate of its error covariance P_t^- from the current measurement [5, Equations 4.2.17, 4.2.8, 4.2.22]:

$$K_t = P_t^- H_t^\top (H_t P_t^- H_t^\top + R_t)^{-1} \quad (21)$$

$$\hat{\mathbf{x}}_t = \hat{\mathbf{x}}_t^- + K_t (\mathbf{z}_t - H_t \hat{\mathbf{x}}_t^-) \quad (22)$$

$$P_t = (I - K_t H_t) P_t^- \quad (23)$$

and then updates for the next recursion [5, Equations 4.2.23, 4.2.25]:

$$P_{t+1}^- = \Phi_t P_t \Phi_t^\top + Q_t \quad (24)$$

$$\hat{\mathbf{x}}_{t+1}^- = \Phi_t \hat{\mathbf{x}}_t. \quad (25)$$

11.2 CHANNEL GAIN AND INTERFERENCE

The power control algorithms in this report assume perfect SINR measurements. This assumption allows algorithm comparison without the confounding effects of measurement errors and disrupting transmissions (e.g., shutting off transmissions to measure the interference is impractical.) In a wireless power control system, the receiver sets its transmitter's power. This knowledge of the transmitter's power makes SINR estimates possible. Received power on link $l = 1, \dots, L$

$$p_{R,l}(t) = g_u(t) p_T(t) + p_{I,l}(t) + p_{N,l}(t) \quad [\text{watts}]$$

is a standard measurement in most software-defined radios (SDR). Define the state vector

$$\mathbf{x}_l(t) := \begin{bmatrix} g_u(t) \\ p_{I,l}(t) \end{bmatrix}.$$

Assume the state-space model of the form

$$\mathbf{x}_l(t_{n+1}) := \mathbf{x}_l(t_n) + \Delta \mathbf{x}_l(t_n).$$

The measurement model for the received power is

$$p_{R,l}(t_n) = [p_{T,l}(t_n) \quad 1] \mathbf{x}(t_n) + p_{N,l}(t_n).$$

The transition matrix and the measurement matrix are known because the transmitter's power is controlled by the receiver:

$$\begin{aligned} \Phi_l(t) &= I \\ H_l(t) &= [p_{T,l}(t) \quad 1]. \end{aligned}$$

Assume the additive RF noise is constant for all receivers:

$$R_l(t_n) = \sigma_N^2.$$

The covariance of the process noise is

$$Q_l(t_n) = E[\Delta \mathbf{x}_l(t_n) \Delta \mathbf{x}_l(t_n)^\top] = \begin{bmatrix} E[\Delta g_{ll}^2(t_n)] & E[\Delta g_{ll}(t_n) \Delta p_{I,l}(t_n)] \\ E[\Delta p_{I,l}(t_n) \Delta g_{ll}(t_n)] & E[\Delta p_{I,l}^2(t_n)] \end{bmatrix}.$$

Assume there is no delay or error between the control power $p_{C,l}(t)$ at the receiver and the transmitted power:

$$p_{T,l}(t) = p_{C,l}(t).$$

As the l th link increments to time t_n , assume prior estimates $\mathbf{x}_l^-(t)$ and $P_l^-(t)$. Update these prior estimates as follows:

$$\begin{aligned} K_l(t_n) &= P_l(t_n)^- H_l(t_n)^\top \left(H_l(t_n) P_l(t_n)^- H_l(t_n)^\top + R_l(t_n) \right)^{-1} \\ \hat{\mathbf{x}}_l(t_n) &= \hat{\mathbf{x}}_l(t_n)^- + K_l(t_n) (p_{R,l}(t_n) - H_l(t_n) \hat{\mathbf{x}}_l(t_n)^-) \\ P_l(t_n) &= (I - K_l(t_n) H_l(t_n)) P_l(t_n)^-. \end{aligned}$$

Update or predict for the next recursion as follows:

$$\begin{aligned} P_l(t_{n+1})^- &= P_l(t_n) + Q_l(t_n) \\ \hat{\mathbf{x}}_l(t_{n+1})^- &= \hat{\mathbf{x}}_l(t_n). \end{aligned}$$

The SINR at the start of the n th frame is estimated as

$$\gamma_{M,l}(t_n) := \frac{g_{ll}(t_n) p_{T,l}(t_n)}{p_{I,l}(t_n) + p_{N,l}(t_n)} \approx \frac{\hat{g}_{ll}(t_n) p_{T,l}(t_n)}{\hat{p}_{I,l}(t_n) + \sigma_N^2}.$$

Knowing the covariances is a basic problem for the Kalman filter. The next sections use the H^2/H^∞ approach to drop the covariance assumptions.

12. H^2 ALGORITHMS

Chaves, Abbas-Turki, Abou-Kandil, and Romano approach power control using [13]: “a standard target tracking algorithm with a dynamic target QoS”. This section reviews their *Opportunistic QoS* approaches and assesses the performance of their static H^2 algorithm (\mathcal{H}_2 -DPC) and their adaptive H^2 algorithm (A- \mathcal{H}_2 -DPC) on the two-link mobile wireless scenario of Section 8. The FM algorithm updates power on the l -th link using the difference between the external SINR $\gamma_{X,l}$ that is *fixed* throughout the wireless operation and the measured SINR $\gamma_{X,l}(t_n)$ that varies in the mobile scenario [22]:

$$\bar{p}_{C,l}(t_{n+1}) = \bar{p}_{C,l}(t_n) + (1 - \beta_l) \{ \bar{\gamma}_{X,l} - \bar{\gamma}_{M,l}(t_n) \}.$$

The step-size for the l -th link is denoted by $0 \leq \beta_l < 1$. The dB scaling is denoted by the overline:

$$\bar{p}_{C,l}(t_n) = 10 \log_{10}(p_{C,l}(t_n)).$$

The H^2 algorithms update power as

$$\bar{p}_{C,l}(t_{n+1}) = \bar{p}_{C,l}(t_n) + (1 - \beta_l) \{ \bar{\gamma}_{T,l}(t_n) - \bar{\gamma}_{M,l}(t_n) \}, \quad (26)$$

where the target SINR $\bar{\gamma}_{T,l}(t_n)$ varies to deliver [13]: “high flexibility on the quality-of-service (QoS) provision by exploiting link quality variation.” The variation of the target SINR “steers” state-space model tracking the power and rate along a trajectory realizing an optimal trade-off between power and rate. More formally, the H^2 algorithms minimize a quadratic form of the power and QoS.

This section starts by reviewing the state-space model and the quadratic form. Urban simulations are run using nominal values that parametrize the quadratic form. These simulations provide a concrete example to discuss the quadratic form. This section concludes by discussing parameterizations the quadratic form to deliver better performance. A state-space model determines the evolution of the target SINR using a state vector measuring the deviation from the minimum power [13, Equation 11]

$$\bar{\epsilon}_l^p(t_n) := \bar{p}_{C,l}(t_n) - \bar{p}_{\min}$$

and the deviation from the maximum SINR [13, Equation 10]

$$\bar{\gamma}_{T,l}(t_n) := \bar{\gamma}_{\max} + u_l(t_n),$$

where $u_l(t_n)$ is the control signal. Subtracting \bar{p}_{\min} from Equation (26) determines state equation of the power derivation

$$\bar{\epsilon}_l^p(t_{n+1}) = \beta_l \bar{\epsilon}_l^p(t_n) + (1 - \beta_l) \{ \bar{\gamma}_{T,l}(t_n) - \bar{\mu}_l(t_n) - \bar{p}_{\min} \},$$

where the channel gain [13, Equation 2]

$$\mu_l(t_n) := \frac{g_{ll}(t_n)}{p_{N,l}(t_n) + \sum_{m \neq l} g_{lm}(t_n) p_{C,m}(t_n - \tau)}$$

is computed from the measured SINR and the known power. Therefore, the state vector for the l -th link [13, Equation 12]

$$\mathbf{x}_l(t_n) := \begin{bmatrix} \bar{\epsilon}_l^p(t_n) \\ \bar{\gamma}_{T,l}(t_n) \end{bmatrix}$$

has the state equation [13, Equation 13]

$$\mathbf{x}_l(t_{n+1}) = A \mathbf{x}_l(t_n) + B_1 \mathbf{w}_l(t_n) + B_2 u_l(t_n),$$

structured by the matrices [13, Equation 14]:

$$A = \begin{bmatrix} \beta & (1-\beta) \\ 0 & 0 \end{bmatrix}; \quad B_1 = \begin{bmatrix} 0 & -(1-\beta) & -(1-\beta) \\ 1 & 0 & 0 \end{bmatrix}; \quad B_2 = \begin{bmatrix} 0 \\ 1 \end{bmatrix}$$

and driven by the exogenous input [13, Equation 14]:

$$\mathbf{w}_l(t_n) := \begin{bmatrix} \bar{\gamma}_{\max} \\ \bar{\mu}_l(t_n) \\ \bar{p}_{\min} \end{bmatrix}.$$

The quadratic trade-off between power and QoS seeks a control sequence $u_l(t_n)$ to minimize the associated quadratic form [13, Equation 15]

$$\mathcal{Q}(\mathbf{u}) := \sum_{n=0}^N \mathbf{x}_l^\top(t_n) Q \mathbf{x}_l(t_n) + r(t_n) u_l(t_n)^2; \quad Q = \begin{bmatrix} 1 & 0 \\ 0 & 0 \end{bmatrix} \quad (27)$$

determined by the sequence of weighting parameters $r(t_n) > 0$. Small values of the weighting parameters force the power to track the minimum power p_{\min} while accepting a lower QoS. Larger values of the weighting parameters force a better QoS at the cost of more power. The challenge is to adapt the trade-off to the time-varying gain matrix or, equivalently, an RF scenario. Chaves solves the quadratic minimization by converting to a feedback control problem [13, Equation 16]

$$G : \begin{cases} \mathbf{x}_l(t_{n+1}) &= A\mathbf{x}_l(t_n) + B_1\mathbf{w}_l(t_n) + B_2u_l(t_n) \\ \mathbf{z}_l(t_n) &= C_1\mathbf{x}_l(t_n) + D_{12}u_l(t_n) \end{cases}$$

that is structured by the matrices [13, Equation 14]:

$$C_1 = \begin{bmatrix} 1 & 0 \\ 0 & 0 \end{bmatrix}; \quad D_{12} = \begin{bmatrix} 0 \\ r(t_n)^{1/2} \end{bmatrix}.$$

Figure 59 illustrates the feedback control determined by the system G . Chaves produces the static controller by setting $r(t_n) = r$ constant and $N \rightarrow \infty$ to obtain the control signal [13, Equation 18, 19]

$$u_l(t_n) = -K\mathbf{x}_l(t_n) = -\left\{r + B_2^\top P B_2\right\}^{-1} B_2^\top P A \begin{bmatrix} \bar{\epsilon}_l^p(t_n) \\ \bar{\gamma}_{T,l}(t_n) \end{bmatrix},$$

where P is the solution to the discrete-time algebraic Riccati equation [13, Equation 20]

$$P = A^\top P A + Q - A^\top P B_2 \left\{r + B_2^\top P B_2\right\}^{-1} B_2^\top P A.$$

Algorithm 3 (\mathcal{H}_2 -DPC) Select the step size $0 \leq \beta < 1$ and QoS weight $r > 0$. Compute the solution P to the discrete-time algebraic Riccati equation [13, Equation 20]

$$P = A^\top P A + Q - A^\top P B_2 \left\{r + B_2^\top P B_2\right\}^{-1} B_2^\top P A.$$

Compute the feedback gain matrix [13, Equation 19]

$$K = \left\{r + B_2^\top P B_2\right\}^{-1} B_2^\top P A.$$

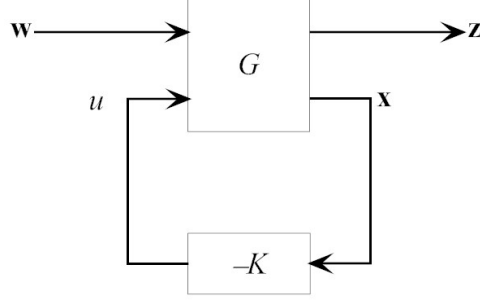


Figure 59. Kalman feedback for QoS power control.

Select the minimum power \bar{p}_{\min} , the initial transmission power $\bar{p}_{\text{ini},l}$, and the maximum SINR $\bar{\gamma}_{\max}$. Initialize the state vectors

$$\mathbf{x}_l(t_0) = \begin{bmatrix} \bar{e}_l^p(t_0) \\ \bar{\gamma}_{T,l}(t_0) \end{bmatrix} = \begin{bmatrix} \bar{p}_{\text{ini},l} - \bar{p}_{\min} \\ \bar{\gamma}_{\max} \end{bmatrix}$$

on all the links $l = 1, \dots, L$. Assume the wireless network has been operating with initial power up to the time the power control is turned on: $p_{C,l}(t) = p_{\text{ini},l}$ for $t \leq t_0$ and for $l = 1, \dots, L$

H-1 The network is synchronized and all updates occur at the start of each frame: $t_n := nt_F$.

H-2 Each receiver measures its SINR at the start of each frame:

$$\gamma_{M,l}(t_n) = \frac{g_{ll}(t_n)p_{C,l}(t_n - \tau)}{p_{N,l}(t_n) + \sum_{m \neq l} g_{lm}(t_n)p_{C,m}(t_n - \tau)}.$$

H-3a Extract the adaptive target SINR from the state vector

$$\mathbf{x}_l(t_n) = \begin{bmatrix} \bar{e}_l^p(t_n) \\ \bar{\gamma}_{T,l}(t_n) \end{bmatrix} \rightarrow \gamma_{T,l}(t_n).$$

H-3b Update the exogenous input vector from the measured SINR

$$\gamma_{M,l}(t_n) \rightarrow \begin{bmatrix} \bar{\gamma}_{\max} \\ \bar{\mu}_l(t_n) \\ \bar{p}_{\min} \end{bmatrix} = \mathbf{w}_l(t_n).$$

H-3c Update the state vector

$$\mathbf{x}_l(t_{n+1}) = (A + B_2K)\mathbf{x}_l(t_n) + B_1\mathbf{w}_l(t_n).$$

H-4 The power is updated for the frame $[t_n, t_{n+1})$ as

$$p_{C,l}(t_{n+1}) = p_{C,l}(t_n) \left\{ \frac{\gamma_{T,l}(t_n)}{\gamma_{M,l}(t_n)} \right\}^{1-\beta}.$$

12.1 \mathcal{H}^2 -DPC MOBILE PERFORMANCE AT 1.9 GHZ

Table 11 lists the RF parameters of the gain matrix, the SINR, and the updating of the wireless control algorithms. These parameters are outside the control of the \mathcal{H}^2 -DPC algorithm. Table 14 lists the inputs to the \mathcal{H}^2 -DPC algorithm. The QoS is 1 Mbps on both links; the large weighting parameter r biases the power-rate trade-off to the QoS; the frame duration of $t_F = 1$ ms sets the power control update rate; the delay is a fraction of a frame.

Table 14. \mathcal{H}^2 -DPC Parameters.

Variable	Value	Description
$R_{b,X}$	1 Mbps	Throughput
p_{\min}	0 W	Minimum power
p_{\max}	1 W	Maximum power
p_{ini}	10 μ W	Initial power
β	0.9	Stepsize
r	500	Weighting parameter

Figure 60 reports the power and the rate for the network during the time TX-2 travels along the x -axis track. The upper panel compares the power on each link computed by the distributed \mathcal{H}^2 -DPC algorithm. The lower panel compares throughput on each link. Although the coding gain is $g_C = 10$ dB, throughput is set using the capacity: $R_b(t) = f_B \times \log_2(1 + \gamma_M(t))$. On the average, the \mathcal{H}^2 -DPC algorithm delivers rates at $R_{b,X} = 1$ Mbps. The next plot reports the average performance along the x -axis track.

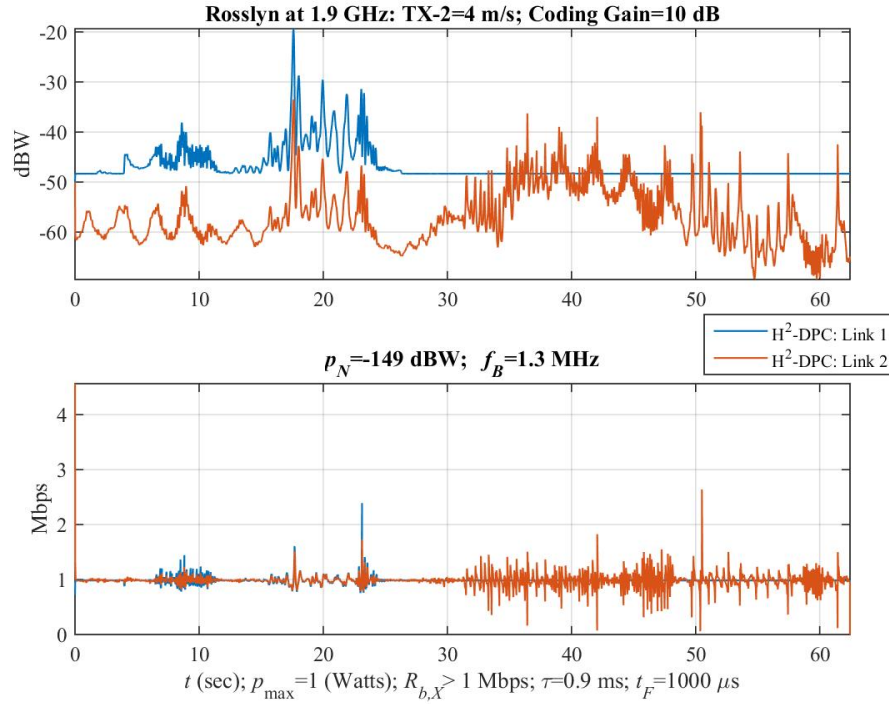


Figure 60. \mathcal{H}^2 -DPC performance along x -axis track; $R_{b,X} = 1$ Mbps; frame duration $t_F = 1$ ms; $f_C = 1.9$ GHz; coding gain $g_C = 10$ dB. Upper Panel: power on each link; Lower Panel: throughput on each link.

Figure 61 assesses the average performance of the \mathcal{H}^2 -DPC algorithm as the mobile network travels along the x -axis track. As described in Section 9.1, an upper bound on performance given by the Exact FM algorithm is plotted. Neither algorithm can meet the QoS constraints at every point along the x -axis track. The next paragraph details how the average performances of both algorithms account for this loss of QoS.

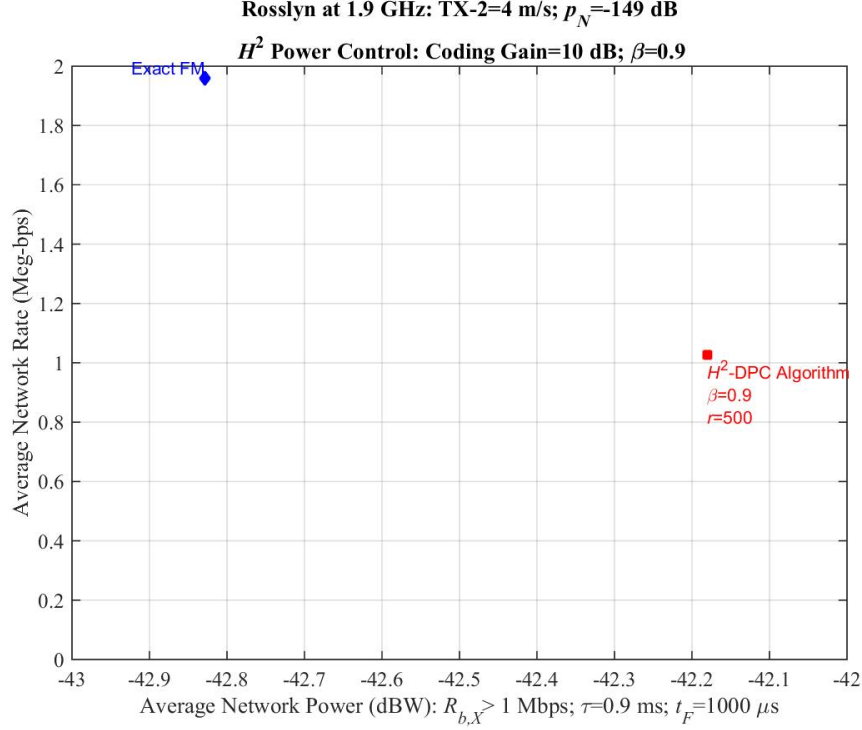


Figure 61. Average \mathcal{H}^2 -DPC performance along x -axis track with delay $\tau = 0.9$ ms; $R_{b,X} = 1$ Mbps; frame duration $t_F = 1$ ms; $f_C = 1.9$ GHz; coding gain $g_C = 10$ dB.

\mathcal{H}^2 -DPC Algorithm: Let $\mathcal{Q}_{\mathcal{H}^2}$ denote those frames that meet the QoS

$$\mathcal{Q}_{\mathcal{H}^2} := \{n \in [1 : N_F] - 1 : \gamma_M(\mathbf{p}_C(t_n); t_n) \geq \gamma_X; t_n = nt_F\},$$

where N_F denotes the number of frames along the track. Averaging the rates over the entire track mixes the unsuccessful QoS transmission with the transmission that met the QoS. This mixing is problematic when one link dominates. For example, Section 8.4 reports Link 1 delivers high rates while Link 2 is almost shut down. Consequently, total throughput is high although QoS is never satisfied. Therefore, the average network rate will be defined as average rate only when the network delivers QoS:

$$R_{\mathcal{H}^2} = \frac{1}{N_F} \sum_{n \in \mathcal{Q}_{\mathcal{H}^2}} \mathbf{1}^T \begin{bmatrix} R_{b,1}(t_n) \\ R_{b,2}(t_n) \end{bmatrix}.$$

Average network power will be defined as the average total power

$$p_{\mathcal{H}^2} = \frac{1}{N_F} \sum_{n=0}^{N_F-1} \mathbf{1}^T \mathbf{p}_C(t_n)$$

because the \mathcal{H}^2 -DPC algorithm always transmits a minimum power.

Exact FM Algorithm (repeated for convenience): The exact FM algorithm operates with zero system delay, global network knowledge of the gain matrix, and power levels to solve for minimum power \mathbf{p}_{\min} that meets the QoS constraints. Not every position along the x -axis track admits a solution. For the exact FM algorithm, let \mathcal{Q}_{XFM} index those frames meeting the QoS

$$\mathcal{Q}_{\text{XFM}} := \{n \in [1 : N_F] - 1 : \gamma_M(\mathbf{p}_{\min}(t_n); t_n) \geq \gamma_X; t_n = nt_F\}.$$

Define the average network rate as the average rate only when the network delivers the QoS:

$$R_{\text{XFM}} = \frac{1}{N_t} \sum_{n \in \mathcal{Q}_{\text{XFM}}} \mathbf{1}^\top \begin{bmatrix} R_{b,X} \\ R_{b,X} \end{bmatrix} = 2R_{b,X} \times \frac{|\mathcal{Q}_{\text{XFM}}|}{N_t}.$$

Therefore, the average power used by the exact FM algorithm is

$$p_{\text{XFM}} = \frac{1}{|\mathcal{Q}_{\text{XFM}}|} \sum_{n \in \mathcal{Q}_{\text{XFM}}} \mathbf{1}^\top \mathbf{p}_{\min}(t_n).$$

Discussion: Figure 61 reports that the \mathcal{H}^2 -DPC algorithm delivers approximately half of the best possible network rate using only slightly more power. The \mathcal{H}^2 -DPC algorithm delivers this performance against the system delay of $\tau = 0.9$ ms and no global knowledge of the network—each link uses only information measured at its receiver. The next section assesses the \mathcal{H}^2 -DPC algorithm against larger system delays.

12.2 \mathcal{H}^2 -DPC PERFORMANCE AGAINST DELAY

Figure 62 compares the average power-rate performance for the Exact FM algorithm to the \mathcal{H}^2 -DPC algorithm. As in Section 12.1, the exact FM algorithm operates with zero system delay, global network knowledge, and solves for minimum power \mathbf{p}_{\min} meeting the QoS constraints. Therefore, its performance has not shifted from Figure 61. The \mathcal{H}^2 -DPC algorithm “hangs” tight until the delay exceeds 8 ms. At 9 ms delay, the power jumps by 25 dB. Increasing delays in excess of 9 ms force the power to increase while the throughput rolls off. Thus, the \mathcal{H}^2 -DPC algorithm exhibits delay threshold—exceeding this threshold incurs system collapse.

12.3 ADAPTIVE \mathcal{H}^2 -DPC

Chaves points out that adapting the weighting parameters $r(t_n) > 0$ to the time-varying channel produces an adaptive \mathcal{H}^2 -DPC algorithm and offers the following rule as a starting point [13, Equation 21]:

$$r(t_n) := \max\{\phi \times (\bar{\gamma}_{\max} - \bar{\gamma}_M(t_n), r_{\min}\}, \quad (28)$$

where $r_{\min} > 0$ and $\phi > 0$ selects throughput or power savings via ϕ “large” or “small,” respectively. Minimizing the quadratic for this adaptive $r(t_n)$ forces a time-varying gain $K(t_n)$ computed from a *backwards* Riccati [13, Equation 22]

$$K(t_n) = (r(t_n) + B_2^\top P(t_{n+1}) B_2)^{-1} B_2^\top P(t_{n+1}) A$$

and a *backwards* Riccati for the projection matrix $P(t_n)$. These backwards recursions are not possible because the weighting parameters $r(t_n)$ are computed from propagation conditions. Chaves works around this future-past conflict as follows [13]: “Therefore, the adaptive \mathcal{H}^2 -DPC algorithm consists in implementing the \mathcal{H}^2 -DPC algorithm for a different $r(t_n)$ for each time slot, according to Equation (28). We call this procedure the adaptive \mathcal{H}^2 distributed power control (A- \mathcal{H}^2 -DPC) algorithm.”

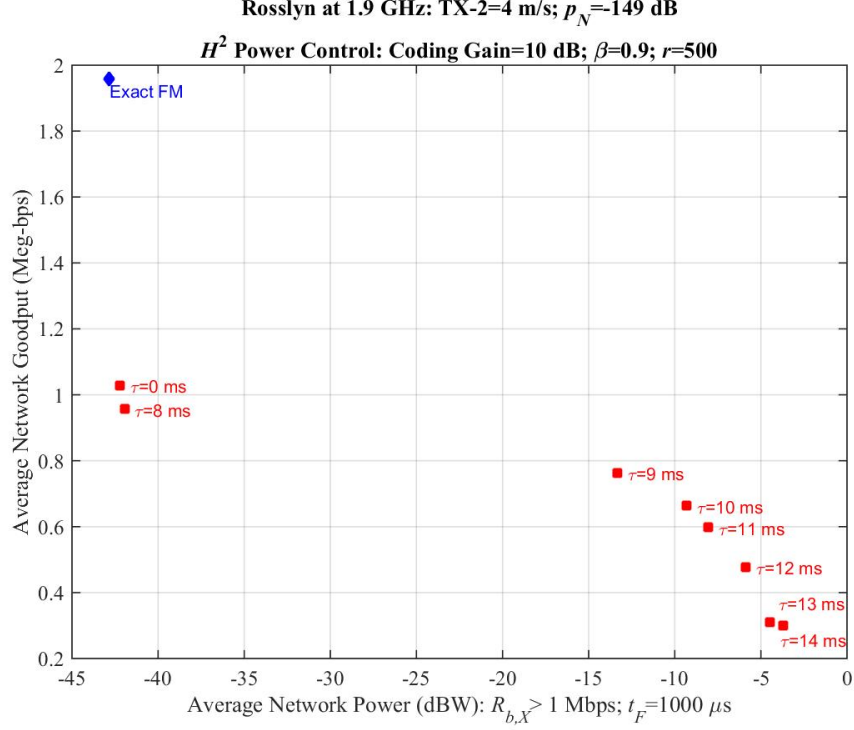


Figure 62. Average \mathcal{H}^2 -DPC power-rate performance along x -axis track subjected to delays; $R_{b,X} = 1$ Mbps; frame duration $t_F = 1$ ms; $f_C = 1.9$ GHz; coding gain $g_C = 10$ dB.

Algorithm 4 (A- \mathcal{H}_2 -DPC) Select the step size $0 \leq \beta < 1$. Select $r_{\min} > 0$. Select $\phi > 0$ “large” for throughput or $\phi > 0$ “small” to save power. Select the minimum power \bar{p}_{\min} , the initial transmission power $\bar{p}_{\text{ini},l}$, and the maximum SINR $\bar{\gamma}_{\max}$. Initialize the state vectors

$$\mathbf{x}_l(t_0) = \begin{bmatrix} \bar{e}_l^p(t_0) \\ \bar{\gamma}_{T,l}(t_0) \end{bmatrix} = \begin{bmatrix} \bar{p}_{\text{ini},l} - \bar{p}_{\min} \\ \bar{\gamma}_{\max} \end{bmatrix}$$

on all the links $l = 1, \dots, L$. Assume the wireless network has been operating with initial power up to the time the power control is turned on: $p_{C,l}(t) = p_{\text{ini},l}$ for $t \leq t_0$ and for $l = 1, \dots, L$:

H-1 The network is synchronized and all updates occur at the start of each frame: $t_n := nt_F$.

H-2 Each receiver measures its SINR at the start of each frame:

$$\gamma_{M,l}(t_n) = \frac{g_{ll}(t_n)p_{C,l}(t_n - \tau)}{p_{N,l}(t_n) + \sum_{m \neq l} g_{lm}(t_n)p_{C,m}(t_n - \tau)}.$$

H-3a Extract the adaptive target SINR from the state vector

$$\mathbf{x}_l(t_n) = \begin{bmatrix} \bar{e}_l^p(t_n) \\ \bar{\gamma}_{T,l}(t_n) \end{bmatrix} \rightarrow \gamma_{T,l}(t_n).$$

H-3b Update the exogenous input vector from the measured SINR

$$\gamma_{M,l}(t_n) \rightarrow \begin{bmatrix} \bar{\gamma}_{\max} \\ \bar{\mu}_l(t_n) \\ \bar{p}_{\min} \end{bmatrix} = \mathbf{w}_l(t_n).$$

H-3c Compute the weighting parameter [13, Equation 21]:

$$r_l(t_n) = \max\{\phi \times (\bar{\gamma}_{\max,l} - \bar{\gamma}_{M,l}(t_n)), r_{\min}\}.$$

H-3d Compute the solution $P_l(t_n)$ to [13, Equation 20]

$$P_l(t_n) = A^\top P_l(t_n) A + Q - A^\top P_l(t_n) B_2 \left\{ r_l(t_n) + B_2^\top P_l(t_n) B_2 \right\}^{-1} B_2^\top P_l(t_n) A.$$

H-3e Compute the feedback gain matrix [13, Equation 19]

$$K_l(t_n) = \left\{ r_l(t_n) + B_2^\top P_l(t_n) B_2 \right\}^{-1} B_2^\top P_l(t_n) A.$$

H-3f Update the state vector

$$\mathbf{x}_l(t_{n+1}) = (A + B_2 K_l(t_n)) \mathbf{x}_l(t_n) + B_1 \mathbf{w}(t_n).$$

H-4 The power is updated for the frame $[t_n, t_{n+1})$ as

$$p_{C,l}(t_{n+1}) = p_{C,l}(t_n) \left\{ \frac{\gamma_{T,l}(t_n)}{\gamma_{M,l}(t_n)} \right\}^{1-\beta}.$$

Figure 63 shows the adaptive \mathcal{H}^2 performance is comparable to the non-adaptive algorithm under moderate delay. Figure 64 reports that the the adaptive \mathcal{H}^2 breaks down with the delay exceeds 8 ms. Figure 65 is the power allocation of this adaptive algorithm. This figure shows that the excessive delay causes this algorithm to “chatter” and instability is likely held in check by the power limiter.

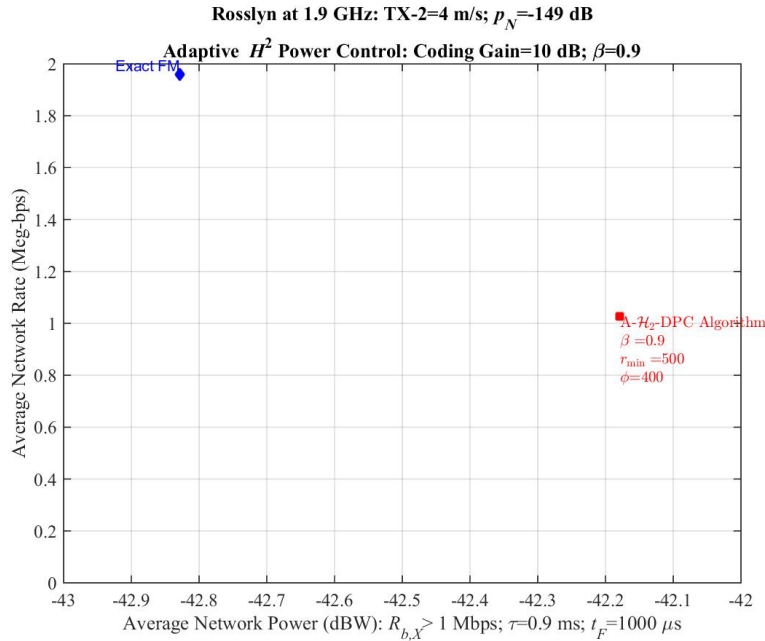


Figure 63. Average A- \mathcal{H}^2 -DPC performance along x -axis track: $\tau = 0.9$ ms.

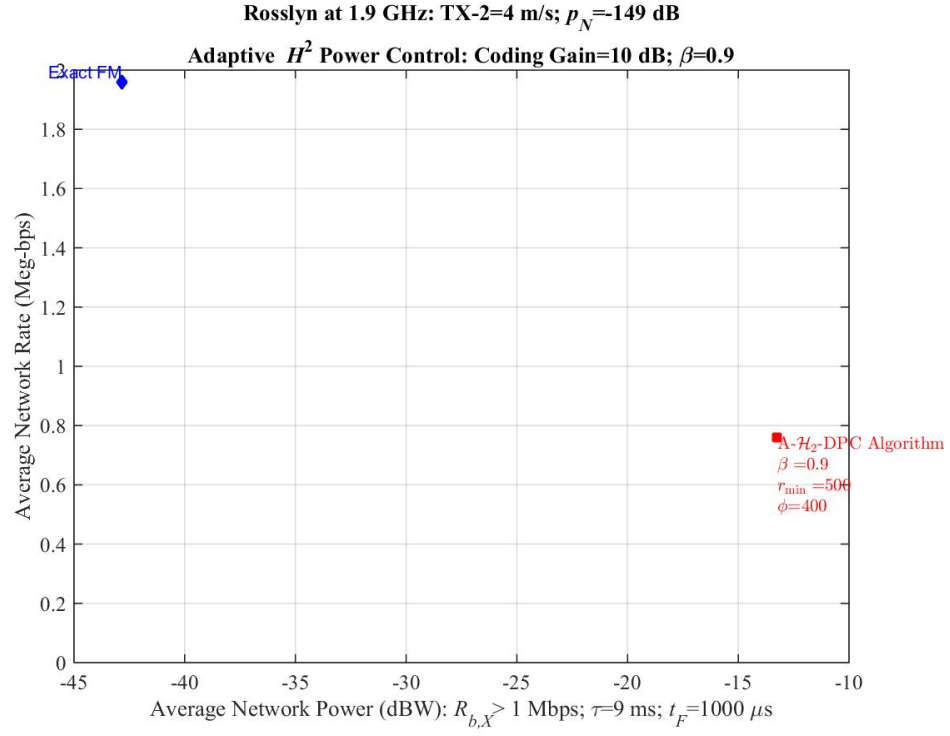


Figure 64. Average A- \mathcal{H}_2 -DPC performance along x -axis track: $\tau = 9$ ms.

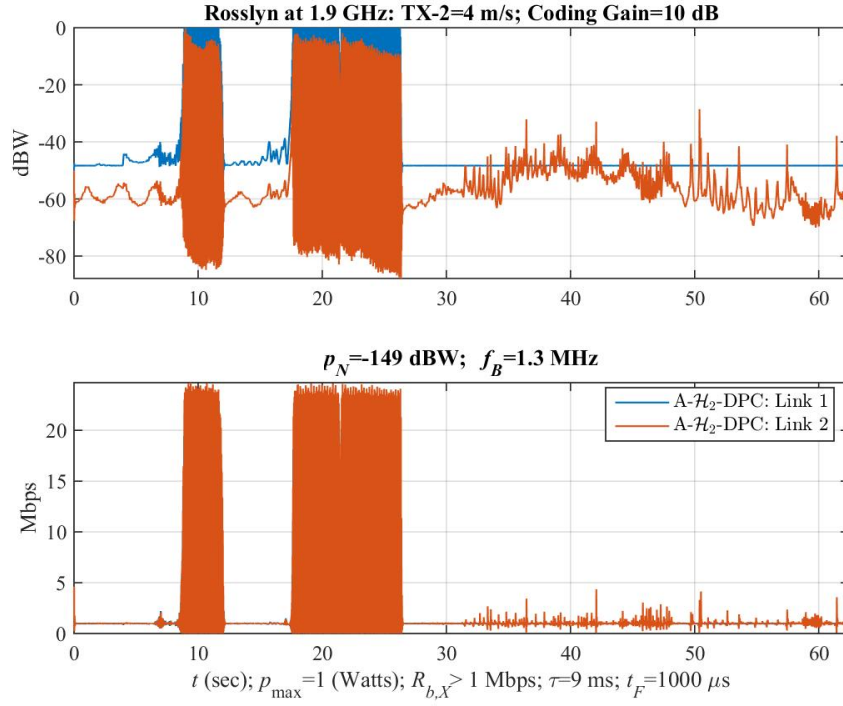


Figure 65. Power allocation for the A- \mathcal{H}_2 -DPC along x -axis track: $\tau = 9$ ms.

13. THE FM-TD ALGORITHM

The preceding sections show the limitations of the FM algorithm, Kalman filtering, the H^2 and H^∞ approaches that model the errors caused by the time delay as noise. Increasing time delays causes all these approaches to fail—time delay is not part of the modeling. Gunnarsson, Guustafsson, and Blom produced a superb analysis of time-delay effects [29]:

“... round-trip delays in the power control loop result in oscillations. Essentially, the core problem is that the measurements do not reflect the most recent power updates. However, these are known to the algorithm, and can be compensated for. Therefore, we adjust the measured SINR according to the power control commands that have been sent but whose effects have not yet been experienced by the receiver.”

The problem is that each receiver measures the time-delayed SINR at the start of each frame:

$$\gamma_{M,l}(t_n) = \frac{g_{ll}(t_n)p_{C,l}(t_n - \tau)}{p_{N,l}(t_n) + \sum_{m \neq l} g_{lm}(t_n)p_{C,m}(t_n - \tau)}$$

whereas the update should use the SINR without time delay

$$\tilde{\gamma}_{M,l}(t_n) = \frac{g_{ll}(t_n)p_{C,l}(t_n)}{p_{N,l}(t_n) + \sum_{m \neq l} g_{lm}(t_n)p_{C,m}(t_n)}.$$

The solution is approximate $\tilde{\gamma}_{M,l}(t_n)$ using the measured SINR and the past power control $p_C(t_n - \tau)$ stored at the receiver [29]:

$$\begin{aligned} \tilde{\gamma}_{M,l}(t_n) &\approx \check{\gamma}_{M,l}(\tau; t_n) \\ &:= \frac{g_{ll}(t_n)p_{C,l}(t_n)}{p_{N,l}(t_n) + \sum_{m \neq l} g_{lm}(t_n)p_{C,m}(t_n - \tau)} \\ &= \gamma_{M,l}(t_n) \frac{p_{C,l}(t_n)}{p_{C,l}(t_n - \tau)}. \end{aligned}$$

Thus, the FM algorithm—and the other wireless power control algorithms—only needs a slight modification to compensate for time delays.

Algorithm 5 (FM-TD) [29] All receivers have an estimate τ_F of the system delay τ .

FMTD-1 The network is synchronized and all updates occur at the start of each frame: $t_n := nt_F$.

FMTD-2 Each receiver measures the time-delay SINR at the start of each frame:

$$\gamma_{M,l}(t_n) = \frac{g_{ll}(t_n)p_{C,l}(t_n - \tau)}{p_{N,l}(t_n) + \sum_{m \neq l} g_{lm}(t_n)p_{C,m}(t_n - \tau)}.$$

FMTD-3 Each receiver compensates for the time delay in the SINR:

$$\check{\gamma}_{M,l}(\tau_F; t_n) = \gamma_{M,l}(t_n) \frac{p_{C,l}(t_n)}{p_{C,l}(t_n - \tau_F)}.$$

FMTD-4 The power is updated for the frame $[t_n, t_{n+1})$ using the delay-compensated SINR:

$$p_{C,l}(t_{n+1}) = p_{C,l}(t_n) \left\{ \frac{\gamma_{X,l}}{\check{\gamma}_{M,l}(\tau_F; t_n)} \right\}^{1-\beta}.$$

FMTD-5 The control power is limited

$$p_{C,l}(t_{n+1}) = [p_{\min} \leq p_{C,l}(t_{n+1}) \leq p_{\max}].$$

Figure 66 reports this delay compensation for the two-link mobile wireless scenario. Instead of the power-rate performance rolling off with increasing delay as seen in the FM algorithm (Figure 55) and the H^2 algorithm (Figure 62), the FM-TD does compensate for time delays sweeping out to 20 ms. However, this performance assumes the system delay is known exactly:

$$\tau = \tau_F.$$

The natural question asks: *How does FM-TD performance degrade when the system delay τ is not known exactly?*

Both the FM algorithm and the H^2 algorithm breakdown when the system delay exceeds $\tau = 10$ ms (Figure 55 and Figure 62). Accordingly, the system delay fixed at $\tau = 10$ ms and τ_F is varied around this delay:

$$\tau_F = \tau \times (1 \pm 25\%) \in [7.5, 12.5] \text{ [ms]}.$$

Figure 67 reports that the FM-TD is robust with respect to errors in the delay of $\pm 25\%$: Although 30 τ_F 's were generated, rounding to the frame increments produced the discrete distribution of FM-TD power-rate performance.

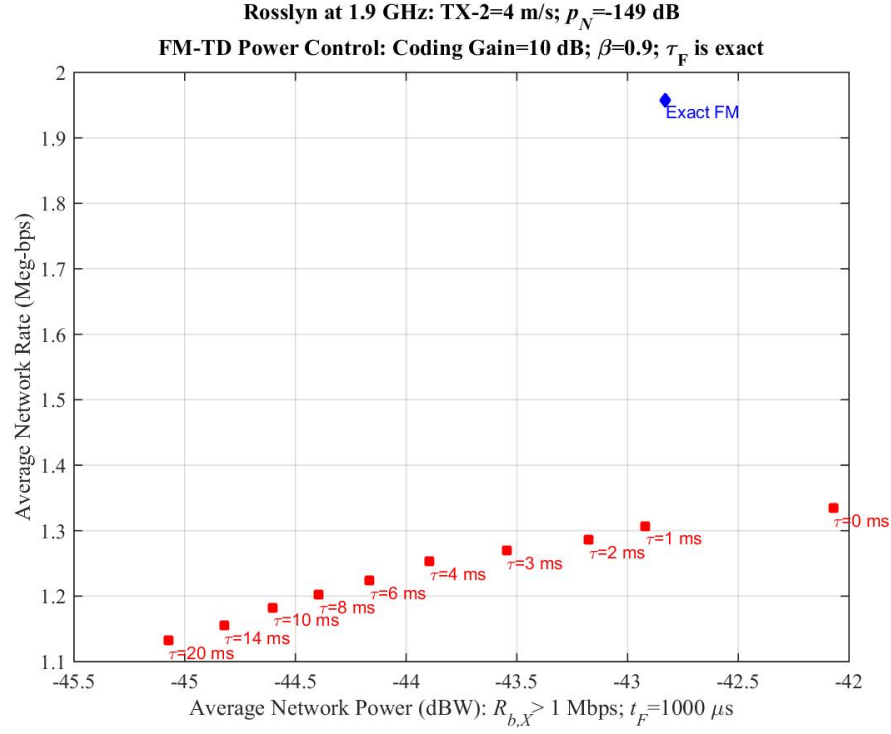


Figure 66. Average FM-TD performance along x -axis track subjected to delays; QoS $R_{b,X} = 1$ Mbps; frame duration $t_F = 1$ ms; $f_C = 1.9$ GHz; coding gain $g_C = 10$ dB; delay is known: $\tau = \tau_F$.

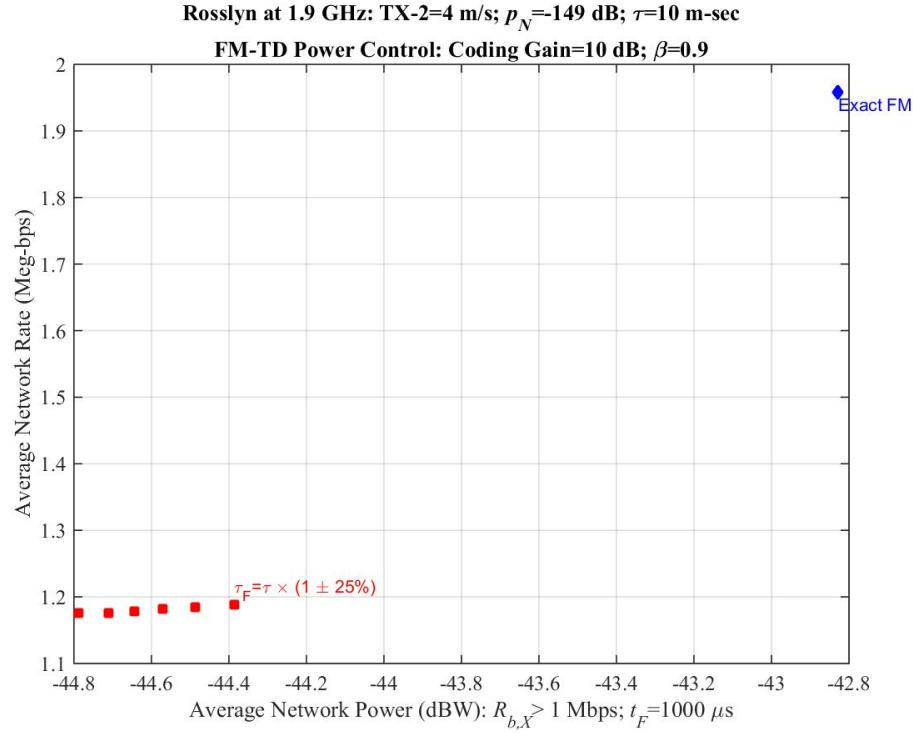


Figure 67. Average FM-TD performance along x -axis track subjected to delays; QoS $R_{b,X} = 1$ Mbps; frame duration $t_F = 1$ ms; $f_C = 1.9$ GHz; coding gain $g_C = 10$ dB; delay is approximate: $\tau_F \approx \tau$.

14. DELAY AND STABILITY

The preceding sections show increasing system delay causes the algorithms to break down. This breakdown is analyzed by considering

- Stability of the FM algorithm
- Variation of the channel
- Effect of delay on stability.

The FM algorithm, without delay and step size is [18, Equation 6]:

$$\mathbf{p}(t_{n+1}) = \mathbf{p}(t_n) \frac{\gamma_X}{\gamma_M(t_n)}.$$

Assuming the channel does not change, this distributed recursion is equivalent to the *power method* [18, Equation 5]

$$\mathbf{p}(t_{n+1}) = \mathbf{y} + F\mathbf{p}(t_n), \quad (29)$$

where F is the *feedback matrix* $F = G_S^{-1} \Gamma_X G_I$ determined by the channel gain matrices and $\Gamma_X := \text{diag}(\gamma_X)$. Assuming spectral radius of the *feedback matrix* is strictly less than unity $\rho(F) < 1$, the FM algorithm converges to the solution of $(I - F)\mathbf{p} = \mathbf{y}$ by the partial sums

$$\mathbf{p}(t_n) = \sum_{k=0}^n F^k \mathbf{y} \rightarrow (I - F)^{-1} \mathbf{y}.$$

Thus, convergence of the FM algorithm is guaranteed assuming (i) that the channel does not change and (ii) the spectral radius $\rho(F) < 1$. Figure 68 plots the spectral radius $\rho(F)$ along the x -axis track. This plot shows $\rho(F) < 1$ excepting a few points in the initial part of the track ($0 < x < 100$). Thus, the FM algorithm converges at almost all points along the track—provided the channel does not change. Therefore, the discussion turns to the question: *What effect does the channel variation have on the FM convergence?* The absolute error between the matrix inverse $(I - F)^{-1}$ and the associated partial sums is bounded by Lemma 4:

$$\text{AbsErr}(F; n_{\text{FM}}) := \left\| (I - F)^{-1} - \sum_{k=0}^{n_{\text{FM}}} F^k \right\| \leq \frac{\|F\|^{n_{\text{FM}}+1}}{1 - \|F\|}; \quad n = 0, 1, \dots$$

Define the relative error between the matrix inverse $(I - F)^{-1}$ and the associated partial sums as follows:

$$\text{RelErr}(F; n_{\text{FM}}) := \frac{\text{AbsErr}(F; n_{\text{FM}})}{\|(I - F)^{-1}\|}.$$

Figure 69 estimates the number of iterations n_{FM} for the FM algorithm to converge to “2-digit” accuracy:

$$\text{RelErr}(F; n_{\text{FM}}) \leq 10^{-2},$$

using the standard matrix norm. This plot report that convergence requires less than 200 iterations over most of the slow fading ($0 < x < 100$) part of the track. Over the fast fading part of the track ($100 < x$), the plot reports five iterations or less are needed.

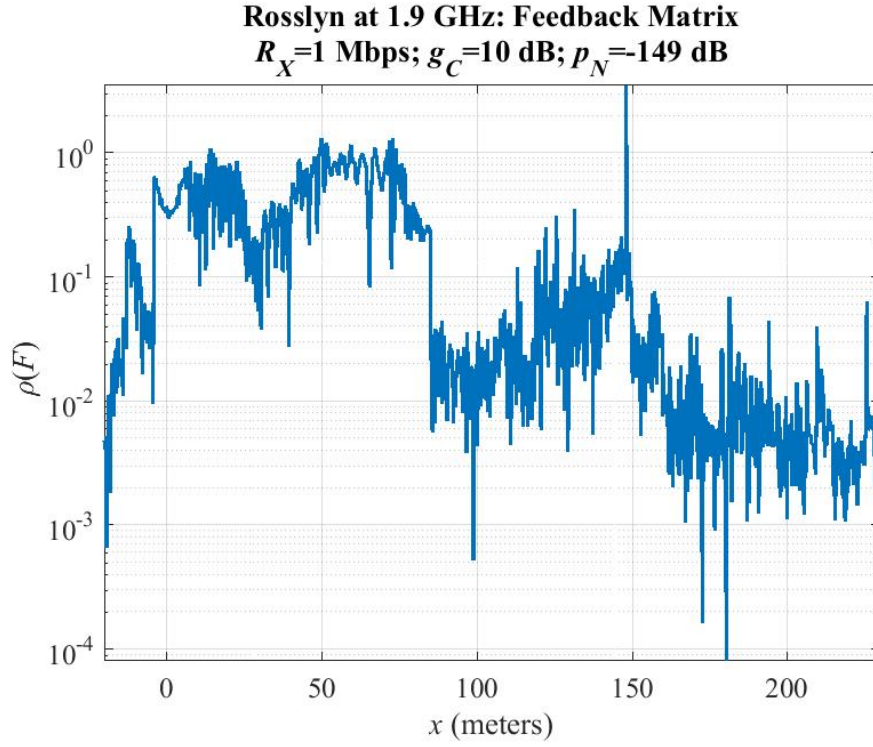


Figure 68. Spectral radius of the feedback matrix x -axis track; QoS $R_{b,X} = 1$ Mbps; $f_C = 1.9$ GHz; coding gain $g_C = 10$ dB.

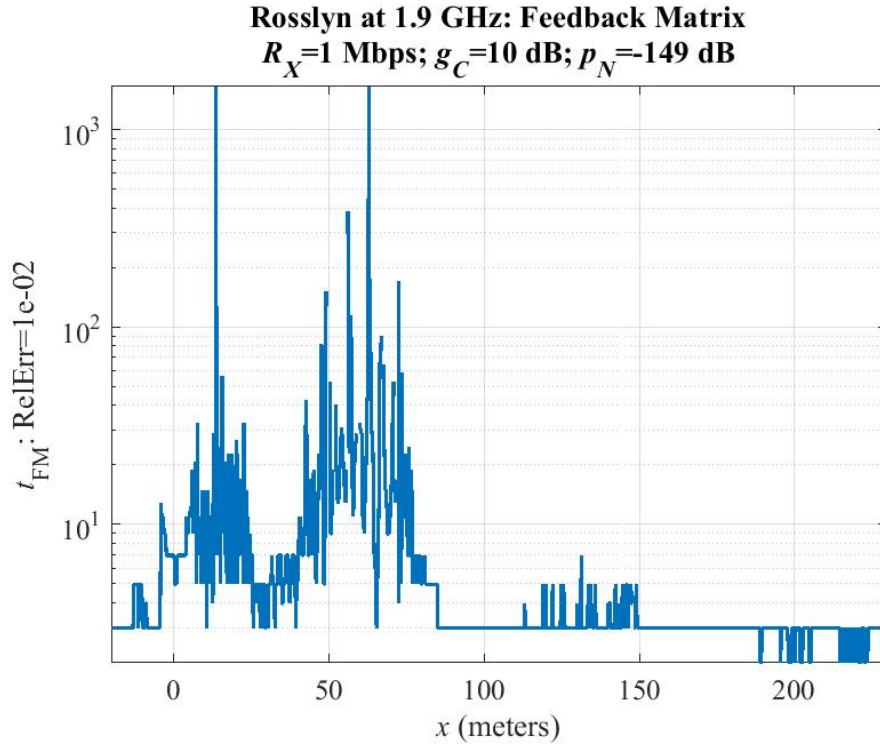


Figure 69. FM algorithm convergence along x -axis track; QoS $R_{b,X} = 1$ Mbps; $f_C = 1.9$ GHz; coding gain $g_C = 10$ dB; “blanks” mark where $\rho(F(x)) > 1$.

Section 8 defines the channel correlation function $|C_{hh}(\Delta x)|$ and the correlation distance $\Delta x(90\%)$ as the biggest distance where

$$|C_{hh}(\Delta x)| \geq 0.9$$

for all $\Delta x \in [0, \Delta x(90\%)]$. Table 15 reports this correlation distance in Column 2 for both the slow-fading region ($0 < x < 100$) and the fast-fading region ($x > 100$). Column 3 lists the time for transmitter TX-2 to decorrelate when traveling at $v = 4$ m/s. The FM algorithm is updating at the frame rate of $t_F = 1$ ms. Columns 4 and 5 lists the time and number of iterations for for the FM algorithm to deliver “two-digit” accuracy. Table 15 and shows the FM algorithm will converge to “two-digit” accuracy in both the slow-fading and fast-fading regions—without time delays.

Table 15. Spatial correlation and convergence along the x -axis track; Transmitter TX-2 traveling at $v = 4$ m/s; frame duration $t_F = 1$ ms.

Fading	$\Delta x(90\%)$	Δt	t_{FM}	n_{FM}
Slow	0.90 m	225 ms	200 ms	200
Fast	0.07 m	17.5 ms	5	5

Figure 70 shows the FM algorithm performance along the track with the system delay of $\tau = 10$ ms. This figure shows that the FM algorithm breaks down in the slow-fading region but recovers to deliver the QoS in the fast-fading region.

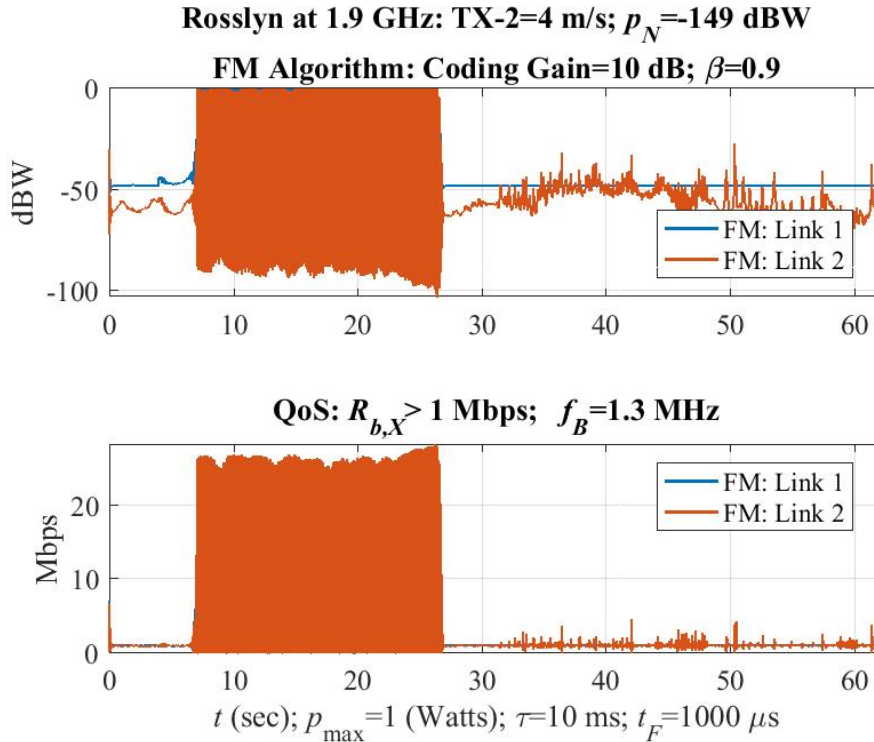


Figure 70. FM algorithm against delay $\tau = 10$ ms along the x -axis track; QoS $R_{b,X} = 1$ Mbps; $f_C = 1.9$ GHz; coding gain $g_C = 10$ dB.

Time delay induces instabilities. The FM algorithm without stepsize operating in a static channel

$$\begin{aligned}
p_l(t_{n+1}) &= p_l(t_n) \frac{\gamma_{X,l}}{\gamma_{M,l}(t_n)} \\
&= \frac{p_l(t_n)}{p_l(t_n - \tau)} \frac{\gamma_{X,l}}{g_{ll}} \left\{ p_{N,l} + \sum_{m \neq l} g_{ml} p_m(t_n - \tau) \right\}.
\end{aligned} \tag{30}$$

When the time delay is zero $\tau = 0$, the leading term is unity and this formulation reduces to Equation (29):

$$p_l(t_{n+1}) = \frac{\gamma_{X,l}}{g_{ll}} p_{N,l} + \sum_{m \neq l} \frac{\gamma_{X,l}}{g_{ll}} g_{ml} p_m(t_n).$$

Analysis of the single-link system suffices to show how delay affects the system stability. Figure 71 is a block diagram of the single-link system.

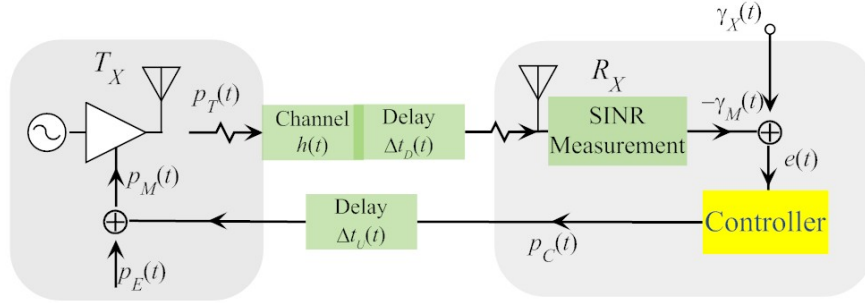


Figure 71. Single link model.

The FM algorithm for a single link with delay and stepsize is

$$p(t_{n+1}) = p(t_n) \left(\frac{\gamma_X}{g p(t_n - \tau) / p_N} \right)^{1-\beta},$$

where g is the the channel magnitude. Converting to log scale and approximating $\tau \approx t_F k$ produces the linear recursion

$$\bar{p}(n+1) = \bar{p}(n) - (1-\beta)\bar{p}(n-k) + y.$$

This recursion is stable provided the roots of

$$\psi(k, \beta; z) = z^{k+1} - z^k + (1-\beta) = 0$$

are contained in the closed unit disk $|z| \leq 1$ and any root on the boundary of the disk $|z| = 1$ is simple [71, Theorem 7.2.9.6]. For each delay k , let $z_m(k, \beta)$ denote the roots of the recursion $m = 1, \dots, (k+1)$:

$$\psi(k, \beta; z_m(k, \beta)) = 0.$$

Figure 72 plots the maximum of the magnitude roots as a function of the stepsize.

$$\beta \mapsto \max\{|z_m(k, \beta)| : m = 1, \dots, (k+1)\}.$$

This plot shows that increasing delays require β to migrate toward 1. The two-link simulations in this report all use $\beta = 0.9$. Figure 72 reports the FM algorithm becomes unstable for $k = 16$ at $\beta = 0.9$. All

simulations in this report set the update increment at $t_F = 1$ ms. Thus, the single links become unstable at the delay $\tau = 16$ ms. The two-link networks in this report all reported instability when the delay $\tau > 8$ ms. These two-link networks are two single-links coupled by their mutual interference. If each single link becomes unstable at $\tau = 16$ ms, instability for $\tau \leq 16$ should be expected when these unstable links are coupled. Therefore, stabilization of each single link, such the time-delay compensation algorithm (Section 13), is a necessary condition for network stability.

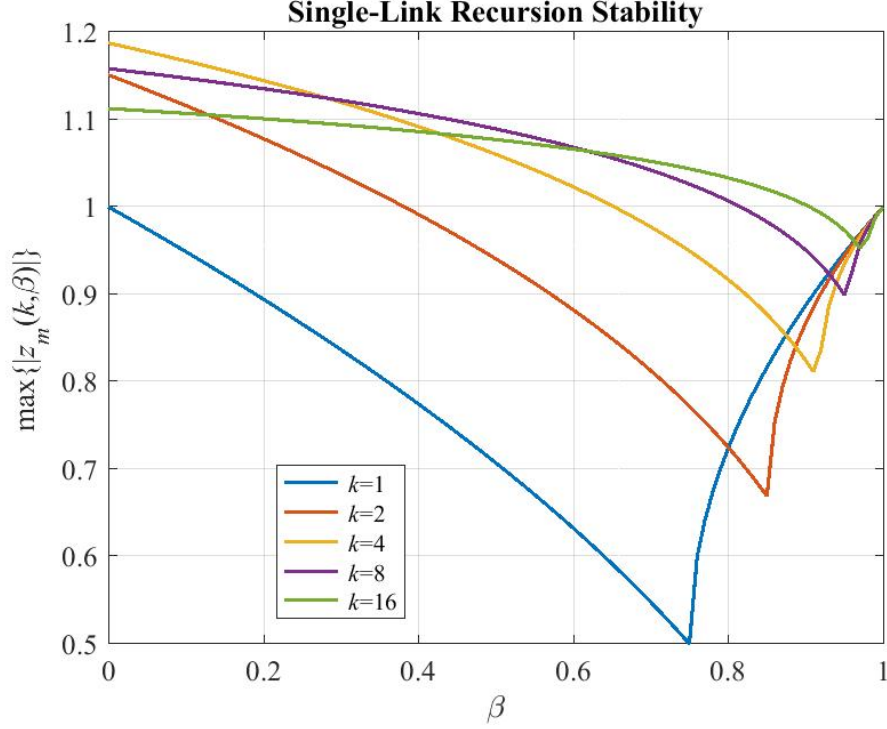


Figure 72. Stability of the recursion for the single-link system; maximum of roots of $z^{k+1} - z^k + (1 - \beta) = 0$

15. EXTENDING WIRELESS POWER CONTROL

Performance of the wireless power control algorithms was determined from the three-dimensional urban simulation operating under the assumptions of ideal measurements and perfect timing. As such, algorithm performance was assessed against channel variations and system delays without the entanglements of modeling non-ideal measurements. This final section proposes a similar approach to encompass non-ideal measurements and multivariate wireless power control algorithms:

- Non-ideal measurements
- Joint optimization and cross-layer optimization
- Wideband power control.

These simulations propose to follow the same pattern as the simulations in this report: upper bounds on algorithm performance are obtained by modeling “best possible” assumptions; relative performance shifts between contending algorithms ranks of the algorithms.

15.1 NON-IDEAL MEASUREMENTS

Assessment of the wireless power control algorithms assumed ideal measurements: perfect SINR measurements, exact power control commands, and perfect timing for the updates. There are two payoffs for this approach: (i) an upper bound on algorithm performance is established assuming ideal measurements, (ii) algorithm sensitivity to non-ideal measurements is computable. The latter item requires error modeling encompassing measurement systems currently operating in specific radio systems. A remarkable paper by Jian, Sidiropoulos, and Giannakis undertakes such modeling [36]. The paper start by quantifying the necessity of accurate measurements for wireless power control [36]:

- “A 1-dB reduction in local power estimation error enables accommodating five more users in a system for a fixed outage probability, under a variety of power control schemes.” [74]
- Adapting “signal constellations according to both the instantaneous receiver signal power and local mean (shadow) power . . . require accurate shadow power estimation and prediction.” [19]

The paper identifies limitations of commercial power estimation techniques [36]:

- “A simple type of window-based estimator, namely weighted sample average estimators of local mean power, is currently employed in many commercial communication systems such as GSM, and the Motorola Personal Access Communication System (PACS) ” [33], [59]
- “Both analysis . . . and experiment shows that the mean-square error (MSE) performance of these window based estimators deteriorates severely when the window size increases beyond certain value.”

The paper produces a Kalman filter for estimating local channel gain [36]:

“that always meets or exceeds the performance of window-based estimators . . . and provides a host of other side benefits as well.”

This approach influenced other papers [68], [72]. Therefore, these papers provide a natural approach to rank wireless power control algorithms operating from non-ideal measurements.

15.2 CROSS-LAYER OPTIMIZATION

The wireless power control algorithms considered in this report were limited only controlling the power in the PHY-layer. A massive literature exists on boosting wireless power control by jointly optimizing other PHY-layer controllers or working across the MAC layer. Two surveys on this *Cross-Layer* optimization are [50], [58] while the specific algorithms are listed:

- Power Control & Beamforming: [30], [61]
- Power Control & Channel Selection: [54], [68]
- Power Control, Scheduling & Routing: [44], [67], [51], [57].

The payoff from these extra “knobs” in controller is expected to be substantial. For example, beam steering—essentially managing the network’s inference—nearly doubles network throughput in this urban simulation [16]. However, enlarging the number of “knobs” in the domain of the optimizer typically increases system delay and decreases system stability. Algorithms that encompass the MAC layer are dependent on the network messaging. This messaging may not be supported in the distributed or non-centralized wireless power control for tactical networks. Therefore, before implementing joint optimization scheme that operate across multiple layers, simulations can assess both the performance and the stability under the assumption of perfect cross-layer communication. If the proposed algorithms deliver significant performance shifts, consideration of the messaging complexity is justified.

15.3 BANDWIDTH

The wireless algorithms considered in report are narrowband. Power control algorithms operating over wide bandwidths typically employ OFDM waveforms [69], [42], [78]. Local geometry and the wavelength determine the variations across the band. For example, Figure 73 plots the wideband gain matrix (left) and the SINR (right) over the 20-MHz band centered at 1.9 GHz when the mobile transmitter TX-2 is located at $x = 0$.

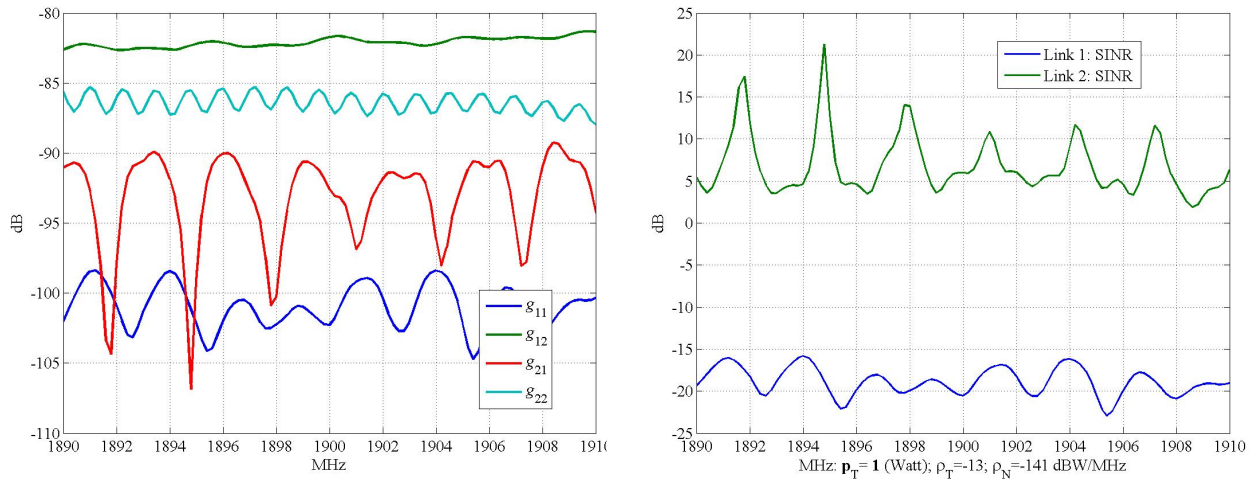


Figure 73. Gain matrix at 1.9 GHz (left); SINR at 1.9 GHz (right).

The gains are relatively flat in comparison to the interference generated by Link 1. That interference has 15-dB swings forcing corresponding variations in the SINR. The SINR is computed assuming both transmitters each broadcast a total of $\mathbf{p}_T = \mathbf{1}$ watt over the entire frequency band $f_B = 20$ MHz producing a signal spectral density vector

$$\rho_T(f) = \frac{\mathbf{p}_T}{f_B} = \frac{1}{f_B} \begin{bmatrix} 1 \\ 1 \end{bmatrix} \quad [\text{watts} \cdot \text{Hz}^{-1}].$$

This signal spectral density is reported as $\rho_T = -13$ dB/MHz on the SINR plot. The total noise power is $p_N = -158$ dBW and arises from the noise spectral density of $\rho_N = -149$ dB/MHz. The SINR is the ratio of the local signal to noise and interference:

$$\gamma_M(p_T; f) = \frac{G_S(f)\rho_T(f)}{\rho_N(f) + G_I(f)\rho_T(f)},$$

where the signal and interference matrices are

$$G_S(f) = \begin{bmatrix} g_{11}(f) & 0 \\ 0 & g_{22}(f) \end{bmatrix} \quad \text{and} \quad G_I(f) = \begin{bmatrix} 0 & g_{12}(f) \\ g_{21}(f) & 0 \end{bmatrix}.$$

These plots reveals several features: first, the SINR of the links are separated by approximately 15 dB. Therefore, a 10-dB coding gain delivered by CDMA is one option to close this gap. Second, the channels are frequency selective so the OFDM is a candidate waveform. Kuehn, Dekorsy, and Kammeyer observe [43]:

“OFDM (Orthogonal Frequency Division Multiplex) is used to combat the frequency selectivity of the mobile radio channel. Therefore, each subcarrier is affected by flat fading, hence a one-tap equalizer suffices for eliminating channel distortion.”

Gúeguen, Crussi re, and H lard observe that combining OFDM and CDMA handles such channels [28]:

“a new waveform for UWB systems [is] obtained by the combination of Orthogonal Frequency Division Multiplex (OFDM) and Code Division Multiple Access (CDMA). The proposed system, called Spread Spectrum - Multi-Carrier - Multiple Access (SS-MC-MA) turns out to be a judicious solution to combat frequency selectivity and narrowband interferers, and to manage the coexistence of several users and piconets.”

This waveform has been under intense development because of the degrees of freedom [14] and substantial waveform designs for cognitive radios [76].

Regardless of the system, the ensemble of narrowband channels $\{G(x; f_C)\}$ stressed the distributed wireless power control algorithms and showed the sensitivity to system delay. Likewise, the ensemble of wideband channels $\{G(x; f)\}$ should also determine performance bounds to benchmark these wideband systems.

REFERENCES

1. Alavi, S. M. Mahdi; Michael J. Walsh; Martin J. Hayes [2009] Robust Distributed Active Power Control Technique for IEEE 802.15.4 Wireless Sensor Networks—A Quantitative Feedback Theory Approach, *Control Engineering Practice*, 17, pages 805–814.
2. Alavi, S. M. Mahdi; Michael J. Walsh; Martin J. Hayes [2010] Robust Power Control for IEEE 802.15.4 Wireless Sensor Networks with Round-Trip Time-Delay Uncertainty, *Wireless Communications and Mobile Computing*, 10, pages 811–825.
3. Boyd, Stephen and Lieven Vandenberghe [2004] *Convex Optimization*, Cambridge University Press, Cambridge.
4. Brockwell, Peter J. & Richard A. Davis [1987] *Times Series: Theory and Methods*, Springer-Verlag, New York, NY.
5. Brown, Robert Grover & Patrick Y. C. Hwang [2012] *Introduction to Random Signals and Applied Kalman Filtering*, John Wiley & Sons, New York, NY.
6. Buzzi, Stefano; H. Vincent Poor [2008] Joint Receiver and Transmitter Optimization for Energy-Efficient CDMA Communications, *IEEE Journal on Selected Areas in Communications*, 26(3), pages 459–472.
7. Campos-Delgado, Daniel U. & J. Martin Luna-Rivera [2013] Distributed Power Allocation Algorithm in Wireless Networks under SNR Constraints, *International Journal of Electronics and Communications*, 67, pages 1015–1024.
8. Campos-Delgado, Daniel Ulises; Alejandro J. Rojas; Jose Martin Luna-Rivera; Carlos A. Gutiérrez [2015] Event-Triggered Feedback for Power Allocation in Wireless Networks, *IET Control Theory & Applications*, 9(14).
9. Campos-Delgado, Daniel U.; J.M. Luna-Rivera; Alejandro J. Rojas; Carlos A. Gutierrez [2016] Power Allocation in Mobile Cellular Communication under Multiplicative Noise and Interference Uncertainty *IEEE Transactions on Control of Network Systems*.
10. Charalambous, Themistoklis [2009] A Lyapunov-Krasovskii Method for the Stability of the Foschini-Miljanic Algorithm under Time-Varying Delays, *Technical Report*, CUED/F-INFENG/TR.646, University of Cambridge Engineering Department.
11. Chiang, J; P. Hande; T. Lan; C. W. Tan [2008] *Power Control in Cellular Networks*, Now Publishers Inc., Hanover, MA.
12. Chaves, Fabiano de Sousa; F. R. P. Cavalcanti; R. A. de Oliveira Neto; R. B. Santos [2008] Opportunistic Distributed Power Control with Adaptive QoS and Fairness for Wireless Networks, *Wireless Communication and Mobile Computing*, 10, pages 200–213.
13. Chaves, Fabiano de Sousa; Mohaded Abbas-Turki, Hisham Abou-Kandil, Joao Marcos Travassos Romano [2013] Transmission Power Control for Opportunistic QoS Provision in Wireless Networks, *IEEE Transactions on Control Systems Technology*, 21(2).
14. Dahman, Haysam & Yousef Shayan [2011] Performance evaluation of space-time-frequency spreading for MIMO OFDM-CDMA systems *EURASIP Journal on Advances in Signal Processing*, 139.

15. Daly, Michael P. [2012] *Physical-Layer Encryption Using Fixed and Reconfigurable Antennas*, Ph.D Thesis, Electrical Engineering Department, University of Illinois at Urbana-Champaign.
16. Daly, Michael; Jeffery Allen; Marcos Ontiveros; Stephen Aldama [2016] Beamspace Multiple-Input Multiple-Output Part II: Steerable Antennas in Mobile Ad Hoc Networks *SSC Pacific Technical Report*.
17. Dem'yanov, V. F. & V. N. Malozemov [1974] *Introduction to Minimax*, John Wiley & Sons, New York, NY.
18. Douros, Vaggelis G. & George C. Polyzos [2011] Review of Some Fundamental Approaches for Power Control in Wireless Networks, *Elsevier Computer Communications*, 34(13).
19. Duel-Hallen, A.; S. Hu; H. Hallen [2000] Long-Range Prediction of Fading Signals, *IEEE Signal Processing Magazine*, 17, pages 62–75.
20. Elmusrati, Mohammed; Riku Jäntti; Heikki N. Koivo [2007] Multiobjective Distributed Power Control Algorithm for CDMA Wireless Communication Systems *IEEE Transactions on Vehicular Technology*, 56(2).
21. Ewaisha Ahmed & Cihan Tepedelenlioğlu [2015] Joint Scheduling and Power-Control for Delay Guarantees in Heterogeneous Cognitive Radios, <http://arxiv.org/pdf/1602.08010.pdf>
22. Foschini, Gerard J. and Zoran Miljanic [1993] A Simple Distributed Autonomous Power Control Algorithm and its Convergence, *IEEE Transactions on Vehicular Technology*, 42(4).
23. Grandhi, Sudheer A.; Rajiv Vijayan; David J. Goodman [1994] Distributed Power Control in Cellular Radio Systems, *IEEE Transactions on Communications*, 42.
24. Garrity, Thomas A. [2015] *Electricity and Magnetism for Mathematicians*, Cambridge University Press, New York, NY.
25. Georgiou, Orestis; Shanshan Wang; Mohammud Z. Bocus; Carl P. Dettmann; Justin P. Coon [2015] Location, Location, Location: Border Effects in Interference Limited Ad-Hoc Networks, *arXiv:1504.01873v1 [cs.NI]* 8 Apr 2015.
26. Gejji, R. R. [1992] Forward Line Power Control in CDMA Cellular Systems, *IEEE Transactions on Vehicular Technology*, 41(4).
27. Goldsmith, Andrea, [2009] *Wireless Communications*, Cambridge University Press, New York, NY.
28. Gúeguen, Emeric ; Matthieu Crussière; Jean-François H  lard [2007] An OFDM-CDMA scheme for High Data Rate UWB applications, *arXiv:0705.0428v1*
29. Gunnarsson, Fredrik; Fredrik Guustafsson; Jonas Blom [2001] Dynamical Effects of Time Delays and Time-Delay Compensation in Power Controlled DS-CDMA, *IEEE Journal on Selected Areas in Communications*, 19(1), pp. 141–151.
30. Han, Zhu; Farrokhi R. Farrokhi; K. J. Ray Liu [2004] Joint Power Control and Blind Beamforming over Wireless Networks: A Cross-Layer Approach, *EURASIP Journal on Applied Signal Processing*, 5, pp 751–761.

31. Han, Cunwu; Dehui Sun; Song Bi; Lei Liu; Zhengxi Li [2014] Modeling and Model Predictive Power and Rate Control of Wireless Communication Networks, *Journal of Applied Mathematics*, Article ID 642673.
32. Hanly, S. V. & D.N. Tse [1999] Power Control and Capacity of Spread Spectrum Wireless Networks, *Automatica*, 35.
33. Hanzo, L. & J. Stefanov [1994] The Pan-European Digital Cellular Mobile Radio System—Known as GSM, *Mobile Radio Communications*, edited by R. Steel, IEEE Press, New York, NY.
34. Hassan, Naveed Ul; Mohamad Assad, Hamidou Tembine [2013] Distributed H-Infinity-Based Power Control in a Dynamic Wireless Environment, *IEEE Communications Letters*, 17(6).
35. Jäntti, R. & S. Kim [2000] Second-Order Power Control with Asymptotically Fast Convergence, *IEEE Selected Areas in Communications*, 18(3).
36. Jian, Tao; Nicholas D. Sidiropoulos; Georgios B. Giannakis [2003] Kalman Filtering for Power Estimation in Mobile Communications, *IEEE Transactions on Wireless Communications*, 2(1).
37. Jiang, Canming; Yi Shi; Sastry Kompella; Y. Thomas Hou; Scott F. Midkiff [2013] Bicriteria Optimization in Multihop Wireless Networks: Characterizing the Throughput-Energy Envelope, *IEEE Transactions on Mobile Computing*, 12(9).
38. Kaushik, Ankit; Shree Krishna Sharma; Symeon Chatzinotas; Björn Ottersten; Friedrich K. Jondral [2015] Performance Analysis of Underlay Cognitive Radio Systems: Estimation-Throughput Trade-off submitted to *IEEE Wireless Communications Letters*, arXiv:1510.03353 [cs.IT].
39. Kim, J. C. & E. I. Muehldorf [1995] *Naval Shipboard Communications Systems*, Prentice Hall, Englewood Cliffs, NJ.
40. Kong, Shulan; Huanshui Zhang; Zhaosheng Zhang [2013] A Scheme to Design Power Controller in Wireless Network Systems, *Physics Letters A* 361 pages 422–428.
41. Koskie, S. & Zoran Gajic [2006] Signal-to-Interference-based Power Control for Wireless Networks: A Survey 1992–2005, *Dynamics of Continuous, Discrete, and Impulsive Systems Series B: Applications and Algorithms*, 2(2).
42. Koutsopoulos, Iordanis & Leandros Tassiulas [2006] Cross-Layer Adaptive Techniques for Throughput Enhancement in Wireless OFDM-Based Networks, *IEEE/ACM Transactions on Networking*, 44(5).
43. Kuehn, Volker; Armin Dekorsy; Karl-Dirk Kammeyer [2016] Channel Coding Aspects in an OFDM-CDMA System, *preprint*
44. Lakshminarayana, Subhash; Mohamad Assaad; Mérouane Debbah [2011] H-Infinity Control Based Scheduler for the Deployment of Small Cell Networks, 200 International Symposium of Modeling and Optimization of Mobile, Ad Hoc, and Wireless Networks.
45. Lamperski, Andrew & Joun Doyle [2015] The H^2 Problem with Quadratically Invariant Systems With Delays, *IEEE Transactions on Automatic Control*, 60(7).
46. Lancaster, Peter & Miron Tismenetsky [1985] *The Theory of Matrices* (second edition), Academic Press, San Diego, CA.

47. Lax, Peter [2007] *Linear Algebra and Its Applications*, John Wiley & Sons, Inc., Hoboken, NJ.
48. Lee, Bore-Kuen; Yuan-Ho Chen; Bor-Sen Chen [2006] Robust H_∞ Power Control for CDMA Cellular Communication Systems, *IEEE Transactions on Signal Processing*, 54(10).
49. Lin, Che & Bor-Sen Chen [2013] Achieving Pareto Optimal Power-Tracking Control for Interference-Limited Wireless Systems via Multiobjective H_2/H_∞ Optimization, *IEEE Transactions on Wireless Communications*, 12(12).
50. Lin, Xiaojun; Ness B. Shroff; R. Srikant [2006] A Tutorial on Cross-Layer Optimization in Wireless Networks, *IEEE Journal on Selected Areas in Communications*, Special Issue on Non-Linear Optimization of Communication Systems, 24(8), pages 1452–1463.
51. Lin, Xiaojun & Shahzada Rasool [2009] Distributed and Provably Efficient Algorithms for Joint Channel-Assignment, Scheduling and Routing in Multi-Channel Ad Hoc Wireless Networks, *IEEE/ACM Transactions on Networking*, 17(6).
52. López, F. J. Martínez; D. U. Campos-Delgado; J. J. Luna-Rivera [2007] Distributed Power Control Algorithms in the Uplink of Wireless Systems, *Fourth International Conference on Electrical and Electronics Engineering*, Mexico City, Mexico.
53. Luo, Jie; Sennur Ulukus; Anthony Ephremides [2005] Standard and Quasi-Standard Stochastic Power Control Algorithms, *IEEE Transactions on Information Theory*, 55(7).
54. Maghsudi, Setarch & Slawomir Stańczak [2014] Joint Channel Selection and Power Control in Infrastructureless Wireless Networks: A Multi-Player Multi-Armed Bandit Framework, <http://arxiv.org/pdf/1407.5447v1.pdf>.
55. Marhefka, Ronald J. [2002] *Numerical Electromagnetics Code-Basic Scattering Code, (NEC-BSC 4.2) User's Manual*, Department of Electrical Engineering, Ohio State University, Columbus Ohio.
56. John H. Meloling [1994] *A Caustic-Corrected Uniform Geometrical Theory of Diffractions for Evaluating High-Frequency Electro-magnetic Fields Near the Cusp of the Caustic Caused by the Curvature of an Edge*, Ph.D Thesis, The Ohio State University.
57. Mhiri, Mariem; Vineeth S. Varma; Karim Cheikhrouhou; Samson Lasaulce; Abdelaziz Samet [2015] Cross-layer distributed power control: A repeated games formulation to improve the sum energy-efficiency *EURASIP Journal on Wireless Communications and Networking*, 2015:257.
58. Miao, Guowang; Nageen Himayat; Ye (Geoffrey) Li y, and Ananthram Swami [2009] Cross-Layer Optimization for Energy-Efficient Wireless Communications: A Survey, *Wireless Communications and Mobile Computing*, 9, pages 529–542.
59. Motorola, Inc. [1995] *Final Text for PACS Licensed Air Interface (TAG 3) J-STD014*.
60. Muqattash, A. & M. Krunz [2002] Power-Controlled Dual Channel (PDPC) Medium Access Protocol for Wireless Ad Hoc Networks, *Proceedings of the 22nd Annual Joint Conference of the IEEE Computer and Information Societies (INFOCOM)*.
61. Olfat, Masoud ; Farrokh R. Farrokhi; K. J. Ray Liu [2005] Power Allocation for OFDM Using Adaptive Beamforming Over Wireless Networks, *IEEE Transactions on Communications*, 53(3).

62. Olama, M. M.; S.M. Shajaat; S. M. Djouadi; D.C.Charalambous [2005] Stochastic Power Control for Time-Varying Lognormal Fading Wireless Channels, *Proceedings of the American Control Conference*.
63. Ontiveros, M.; Arceo, D.; Allen, J.; James, J.; Daly, M. [2014] Beam-Space MIMO Simulations in a 3-D Suburban Environment, *Antennas and Propagation Society International Symposium (APSURSI)*, pp.472–473.
64. Paul, Ayanendu; Mehmet Akar; Michael G. Safonov; Urbashi Mitra [2005] Adaptive Power Control for Wireless Networks Using Multiple Controllers and Switching, *IEEE Transactions on Neural Networks*, 16(5).
65. Sams, Howard W. [1977] *Reference Data for Radio Engineers (Sixth Edition)* International Telephone and Telegraph Corporation.
66. Schubert M. & H. Bocke [2005] *QoS-Based Resource Allocation and Transceiver Optimization*, Now Publishers Inc., Hanover, MA.
67. Shi, Yi; Y. Thomas Hou; Hanif D. Sherali [2008] Cross-Layer Optimization for Data Rate Utility Problem in UWB-Based Ad Hoc Networks, *IEEE Transactions on Mobile Computing*, 7(6).
68. Shoarinejad, Kambiz; Jason L. Speyer; Gregory J. Pottie [2003] Integrated Predictive Power Control and Dynamic Channel Assignment in Mobile Radio Systems, *IEEE Transactions on Wireless Communications*, 2(5).
69. Song, Guocong & Ye (Geoffrey) Li [2005] Cross-Layer Optimization for OFDM Wireless Networks Part I: Theoretical Framework, *IEEE Transactions on Wireless Communications*, 4(2).
70. Sorooshyari, Siamak & Zoran Gajic [2008] Autonomous Dynamic Power Control for Wireless Networks, *IEEE Transactions on Wireless Communications*, 7(3).
71. Stoer, J. & R. Bulirsch [1980] *Introduction to Numerical Analysis*, Springer-Verlag, New York, NY.
72. Subramanian, Ananth; Ali H. Sayed [2005] Joint Rate and Power Control Algorithms for Wireless Networks, *IEEE Transactions on Signal Processing*, 53(11).
73. Subramanian, Ananth; Ali H. Sayed [2005] A Robust Power and Rate Control Method for State-Delayed Wireless Networks, *Automatica* 41.
74. Tam, W. & F. C. M. Lau [1999] Analysis of Power Control and Its Imperfections in CDMA Cellular Systems, *IEEE Transactions on Vehicular Technologies*, 48, pages 1706–1777.
75. Tan, Chee Wei; Shumel Friedland; Steven Low [2011] Nonnegative Matrix Inequalities and Their Applications to Nonconvex Power Control Optimization, *SIAM Journal Of Matrix Analysis and Applications*, 32(3).
76. Thumar, Vinay; Taskeen Nadkar; Tej Gopavajhula; Uday B Desai; Shabbir N Merchant [2011] Power allocation, bit loading and sub-carrier bandwidth sizing for OFDM-based cognitive radio *EURASIP Journal on Wireless Communications and Networking*, 87.
77. Vincent, Thomas L. & Walter J. Grantham [1981] *Optimality in Parametric Systems*, John Wiley & Sons, New York, NY.

78. Wang, Di; Zhaoquan Li; Xin Wang [2012] Joint Optimal Subcarrier and Power Allocation for Wireless Cooperative Networks Over OFDM Fading Channels *IEEE Transactions on Vehicular Technology*, 61(1).
79. Wu, Yihong; Kai Yang; Jianwei Huang; Xiaodong Wang; Mung Chiang [2014] Distributed Robust Optimization (DRO) Part II: Wireless Power Control, *Springer Optimization and Engineering*, Preprint.
80. Xu, Yongjun & Xiaohui Zhao [2014] Robust Adaptive Power Control for Cognitive Radio Networks, *IET Signal Processing*, 10(1).
81. Yang, Kai; Jianwei Huang; Yihong Wu; Xiaodong Wang; Mung Chiang [2014] Distributed Robust Optimization (DRO), Part I: Framework and Example, *Journal of Optimization and Engineering*, 15(1).
82. Yates, Roy D. [1996] A Framework for Uplink Power Control in Cellular Radio Systems, *IEEE Selected Areas in Communications*, 13(7), pp. 1341–1348.
83. Zander, Jens [1992] Performance of Optimum Transmitter Power Control in Cellular Radio Systems *IEEE Transactions on Vehicular Technology*, 41(1).
84. Zhao, Nan; Zhilu Wu; Yaqin Zhao; Taifan Quan [2009] Robust H^∞ Power Control for CDMA Systems in User-Centric and Network-Centric Manners *ETRI Journal*, 31(4).

APPENDIX A

PROOF OF THE PARETO FRONT THEOREM

Theorem 4 claims the Pareto front of the power-rate image is upper boundary of parameterized by the mapping

$$p_\Sigma \mapsto \max \left\{ R_\Sigma(\mathbf{p}_C) : \mathbf{p}_C \in \mathcal{P}_C; p_\Sigma = \mathbf{1}^\top \mathbf{p}_C \right\} =: \Omega(p_\Sigma).$$

The proof shows the mapping $p_\Sigma \mapsto \Omega(p_\Sigma)$ is continuous and strictly increasing. As such, the graph of this function is its own Pareto front by Lemma 2. In more detail, let $p_{\min} := \mathbf{1}^\top \mathbf{p}_{\min}$ and denote the graph of $p_\Sigma \mapsto \Omega(p_\Sigma)$ as

$$\mathcal{G}(\Omega) := \left\{ \begin{bmatrix} p_\Sigma \\ \Omega(p_\Sigma) \end{bmatrix} : p_\Sigma \geq p_{\min} \right\}.$$

Let $\mathcal{Q} \subset \mathbb{R}^2$ denote the quadrant pointing to “less power and more rate”.

$$\mathcal{Q} := \left\{ \begin{bmatrix} -p_\Sigma \\ r_\Sigma \end{bmatrix} : p_\Sigma, r_\Sigma \geq 0 \right\}.$$

Because this graph $\mathcal{G}(\Omega)$ is its own Pareto front, the Contact Theorem (Theorem 1) requires any contact of this quadrant \mathcal{Q} located at a point on the graph to be precisely that point of contact:

$$\left\{ \begin{bmatrix} p_\Sigma \\ \Omega(p_\Sigma) \end{bmatrix} \right\} = \begin{bmatrix} p_\Sigma \\ \Omega(p_\Sigma) \end{bmatrix} + \mathcal{Q} \cap \mathcal{G}(\Omega).$$

Because this upper boundary is parameterized by continuous and strictly increasing function $p_\Sigma \mapsto \Omega(p_\Sigma)$, contact with the power-rate image (Definition 9)

$$\mathfrak{N}(\mathcal{P}_C) = \left\{ \begin{bmatrix} \mathbf{1}^\top \mathbf{p}_C \\ R_\Sigma(\mathbf{p}_C) \end{bmatrix} : \mathbf{p}_C \in \mathcal{P}_C \right\}$$

must still be the single element:

$$\left\{ \begin{bmatrix} p_\Sigma \\ \Omega(p_\Sigma) \end{bmatrix} \right\} = \begin{bmatrix} p_\Sigma \\ \Omega(p_\Sigma) \end{bmatrix} + \mathcal{Q} \cap \mathfrak{N}(\mathcal{P}_C).$$

The Contact Theorem (Theorem 1) applies again to yield that point on the graph $\mathcal{G}(\Omega)$ must be a Pareto point with respect to the power-rate image $\mathfrak{N}(\mathcal{P}_C)$. Consequently, the graph $\mathcal{G}(\Omega)$ is the Pareto front of the power-rate image $\mathfrak{N}(\mathcal{P}_C)$. The remainder of this appendix is devoted to showing Ω is continuous and increasing.

Lemma 5 *Let X and Y be compact topological spaces. Let $h : X \times Y \rightarrow \mathbb{R}$ be continuous. Define*

$$\Omega(\mathbf{y}) := \max\{h(\mathbf{x}, \mathbf{y}) : \mathbf{x} \in X\}.$$

Then $\Omega : Y \rightarrow \mathbb{R}$ is well-defined and continuous.

Proof: Because $h(\circ, \mathbf{y})$ is continuous on the compact set X , the maximum is well defined. Suppose $\{\mathbf{y}_n\}$ is a sequence in Y converging $\mathbf{y} \in Y$. For each $n = 1, 2, \dots$ define $\mathbf{x}_n \in X$ as a maximizer: $h(\mathbf{x}_n, \mathbf{y}_n) = \Omega(\mathbf{y}_n)$. By compactness of X , $\{\mathbf{x}_n\}$ contains a convergent subsequence. By relabeling, let $\mathbf{x}_n \rightarrow \mathbf{x} \in X$. The corresponding subsequence of $\{\mathbf{y}_n\}$, also relabeled, still converges as $\mathbf{y}_n \rightarrow \mathbf{y} \in Y$. Because h is continuous on $X \times Y$,

$$\lim_{n \rightarrow \infty} h(\mathbf{x}_n, \mathbf{y}_n) = h(\mathbf{x}, \mathbf{y}).$$

Consequently, the sequence $\{\Omega(\mathbf{y}_n)\}$ is a convergent sequence with limit

$$\lim_{n \rightarrow \infty} \Omega(\mathbf{y}_n) = \lim_{n \rightarrow \infty} h(\mathbf{x}_n, \mathbf{y}_n) = h(\mathbf{x}, \mathbf{y}).$$

By definition,

$$\lim_{n \rightarrow \infty} \Omega(\mathbf{y}_n) = h(\mathbf{x}, \mathbf{y}) \leq \Omega(\mathbf{y}).$$

Select any $\mathbf{x}_* \in X$ that is a maximizer

$$h(\mathbf{x}_*, \mathbf{y}) = \Omega(\mathbf{y}).$$

By definition,

$$\Omega(\mathbf{y}_n) \geq h(\mathbf{x}_*, \mathbf{y}_n).$$

Taking the limit on both side produces

$$\lim_{n \rightarrow \infty} \Omega(\mathbf{y}_n) \geq \lim_{n \rightarrow \infty} h(\mathbf{x}_*, \mathbf{y}_n) = h(\mathbf{x}_*, \mathbf{y}) = \Omega(\mathbf{y}).$$

Combine both inequalities to get

$$\Omega(\mathbf{y}) \leq \lim_{n \rightarrow \infty} \Omega(\mathbf{y}_n) \leq \Omega(\mathbf{y})$$

or that $\Omega(\mathbf{y}_n)$ converges to $\Omega(\mathbf{y})$. ///

Lemma 6 Let $p_{\min} := \mathbf{1}^\top \mathbf{p}_{\min}$. Define $\Omega : [p_{\min}, \infty) \rightarrow \mathbb{R}_+$ as

$$p_\Sigma \mapsto \max \left\{ R_\Sigma(\mathbf{p}_C) : \mathbf{p}_C \in \mathcal{P}_C; p_\Sigma = \mathbf{1}^\top \mathbf{p}_C \right\} =: \Omega(p_\Sigma).$$

Then Ω is continuous.

Proof: The feasible power vectors $\mathbf{p}_C \in \mathcal{P}_C$ are parameterized as

$$\mathbf{p}_C = \mathbf{p}_{\min} + (I - F)^{-1} \mathbf{p}_K; \quad p_K \in \mathbb{R}_+^L.$$

Let $\mathcal{U}_K \subseteq \mathbb{R}_+^L$ consisting of all power vectors \mathbf{u}_K with unit network power:

$$\mathbf{1} = \mathbf{1}^\top (I - F)^{-1} \mathbf{u}_K.$$

Observe that \mathcal{U}_K is closed and bounded because $(I - F)$ is invertible. Equivalently, \mathcal{U}_K is compact. Let $p_{\max} > p_{\min}$. Define $\phi : [p_{\min}, p_{\max}] \times \mathcal{U}_K \rightarrow \mathcal{P}_C$ as

$$\phi(p_\Sigma, \mathbf{u}_K) := \mathbf{p}_{\min} + (p_\Sigma - p_{\min})(I - F)^{-1} \mathbf{u}_K.$$

Because $R_\Sigma \circ \phi$ is continuous on the compact domain $[p_{\min}, p_{\max}] \times \mathcal{U}_K$, Lemma 5 determines that

$$p_\Sigma \rightarrow \max \{ R_\Sigma(\phi(p_\Sigma, \mathbf{u}_K)) : \mathbf{u}_K \in \mathcal{U}_K \}$$

must be continuous. Observe that ϕ parameterizes each p_Σ -slice of the feasible power vectors:

$$\begin{aligned} \mathbf{1}^\top \phi(p_\Sigma, \mathbf{u}_K) &= \mathbf{1}^\top \mathbf{p}_{\min} + (p_\Sigma - p_{\min}) \mathbf{1}^\top (I - F)^{-1} \mathbf{p}_K \\ &= p_{\min} + (p_\Sigma - p_{\min}) \\ &= p_\Sigma \end{aligned}$$

for $p_{\min} \leq p_\Sigma \leq p_{\max}$. Consequently,

$$\begin{aligned} \Omega(p_\Sigma) &= \max \left\{ R_\Sigma(\mathbf{p}_C) : \mathbf{p}_C \in \mathcal{P}_C; p_\Sigma = \mathbf{1}^\top \mathbf{p}_C \right\} \\ &= \max \{ R_\Sigma(\phi(p_\Sigma, \mathbf{u}_K)) : \mathbf{u}_K \in \mathcal{U}_K \} \end{aligned}$$

or that $\Omega[p_{\min}, p_{\max}] \rightarrow \mathbb{R}_+$ must be continuous. Because p_{\max} is arbitrary, $\Omega[p_{\min}, \infty) \rightarrow \mathbb{R}_+$ must also be continuous. ///

Lemma 7 Let $p_{\min} := \mathbf{1}^\top \mathbf{p}_{\min}$. Define $\Omega : [p_{\min}, \infty) \rightarrow \mathbb{R}_+$ as

$$p_\Sigma \mapsto \max \left\{ R_\Sigma(\mathbf{p}_C) : \mathbf{p}_C \in \mathcal{P}_C; p_\Sigma = \mathbf{1}^\top \mathbf{p}_C \right\} =: \Omega(p_\Sigma).$$

Then Ω is strictly increasing.

Proof: Set $\tilde{p}_\Sigma > \mathbf{1}^\top \mathbf{p}_{\min}$. Let \mathbf{p}_{\max} be any maximizing vector of

$$\max \left\{ R_\Sigma(\mathbf{p}_C) : \mathbf{p}_C \in \mathcal{P}_C; \tilde{p}_\Sigma = \mathbf{1}^\top \mathbf{p}_C \right\}.$$

Compactness of the intersection of the feasible power vectors \mathcal{P}_C with the linear constraint coupled with the continuity of R_Σ guarantees existence of at least one \mathbf{p}_{\max} . Set $\tilde{\gamma}_X := \gamma_M(\mathbf{p}_{\max})$ and

$$\tilde{F} = G_S^{-1} \tilde{\Gamma}_X G_I; \quad \tilde{\Gamma}_X = \text{diag}(\tilde{\gamma}_X).$$

Because $\tilde{\gamma}_X \geq \gamma_X$, the spectral radius of \tilde{F} cannot exceed the spectral radius of F . By Theorem 3, the feasible power vectors $\tilde{\mathbf{p}}_C \in \mathbb{R}_+^L$ exceeding this new SINR constraint $\tilde{\gamma}_X \leq \gamma_M(\tilde{\mathbf{p}}_C)$ belong to the cone

$$\tilde{\mathbf{p}}_C \in \tilde{\mathcal{P}}_C := \tilde{\mathbf{p}}_X + (I - \tilde{F})^{-1} \mathbb{R}_+^L$$

with vertex

$$\tilde{\mathbf{p}}_X = (I - \tilde{F})^{-1} G_S^{-1} \tilde{\Gamma}_X \mathbf{p}_N.$$

By Theorem 3, this vertex is the unique solution to the equality $\tilde{\gamma}_X = \gamma_M(\tilde{\mathbf{p}}_C)$ for $\tilde{\mathbf{p}}_C \in \tilde{\mathcal{P}}_C$. Thus, $\mathbf{p}_{\max} = \tilde{\mathbf{p}}_X$ and $\gamma_M(\tilde{\mathbf{p}}_X) = \tilde{\gamma}_X$. That is, $\gamma_M(\tilde{\mathbf{p}}_X) \leq \gamma_M(\tilde{\mathbf{p}}_C)$ with equality if and only if $\tilde{\mathbf{p}}_X = \tilde{\mathbf{p}}_C$. Consequently, $R_\Sigma(\tilde{\mathbf{p}}_X) \leq R_\Sigma(\tilde{\mathbf{p}}_C)$ with equality if and only if $\tilde{\mathbf{p}}_X = \tilde{\mathbf{p}}_C$. Because $\tilde{\mathbf{p}}_X$ is the vertex of $\tilde{\mathcal{P}}_C$, $\mathbf{1}^\top \tilde{\mathbf{p}}_X \leq \mathbf{1}^\top \tilde{\mathbf{p}}_C$ with equality if and only if $\tilde{\mathbf{p}}_X = \tilde{\mathbf{p}}_C$. Select any $\Delta \tilde{p}_C > 0$. The preceding inequalities force

$$R_\Sigma(\tilde{\mathbf{p}}_X) < \max \left\{ R_\Sigma(\tilde{\mathbf{p}}_C) : \tilde{\mathbf{p}}_C \in \tilde{\mathcal{P}}_C, \tilde{p}_\Sigma + \Delta \tilde{p}_C = \mathbf{1}^\top \tilde{\mathbf{p}}_C \right\}.$$

By construction, $\tilde{\mathcal{P}}_C \subset \mathcal{P}_C$ so that

$$R_\Sigma(\tilde{\mathbf{p}}_X) < \max \left\{ R_\Sigma(\mathbf{p}_C) : \mathbf{p}_C \in \mathcal{P}_C, \tilde{p}_\Sigma + \Delta \tilde{p}_C = \mathbf{1}^\top \mathbf{p}_C \right\}.$$

Consequently, the mapping

$$p_\Sigma \mapsto \max \left\{ R_\Sigma(\mathbf{p}_C) : \mathbf{p}_C \in \mathcal{P}_C; p_\Sigma = \mathbf{1}^\top \mathbf{p}_C \right\}$$

is a strictly increasing function. ///

REPORT DOCUMENTATION PAGE				Form Approved OMB No. 0704-01-0188	
<p>The public reporting burden for this collection of information is estimated to average 1 hour per response, including the time for reviewing instructions, searching existing data sources, gathering and maintaining the data needed, and completing and reviewing the collection of information. Send comments regarding this burden estimate or any other aspect of this collection of information, including suggestions for reducing the burden to Department of Defense, Washington Headquarters Services Directorate for Information Operations and Reports (0704-0188), 1215 Jefferson Davis Highway, Suite 1204, Arlington VA 22202-4302. Respondents should be aware that notwithstanding any other provision of law, no person shall be subject to any penalty for failing to comply with a collection of information if it does not display a currently valid OMB control number.</p> <p>PLEASE DO NOT RETURN YOUR FORM TO THE ABOVE ADDRESS.</p>					
1. REPORT DATE (DD-MM-YYYY) September 2016		2. REPORT TYPE Final		3. DATES COVERED (From - To)	
4. TITLE AND SUBTITLE Wireless Power Control for Tactical MANET: Power-Rate Bounds				5a. CONTRACT NUMBER	
				5b. GRANT NUMBER	
				5c. PROGRAM ELEMENT NUMBER	
6. AUTHORS Sarah Lauff Jeffery C. Allen David F. Schwartz				5d. PROJECT NUMBER	
				5e. TASK NUMBER	
				5f. WORK UNIT NUMBER	
7. PERFORMING ORGANIZATION NAME(S) AND ADDRESS(ES) SSC Pacific 53560 Hull Street San Diego, CA 92152-5001				8. PERFORMING ORGANIZATION REPORT NUMBER TR 3034	
9. SPONSORING/MONITORING AGENCY NAME(S) AND ADDRESS(ES) SSC Pacific Naval Innovative Science and Engineering (NISE) Program 3560 Hull Street San Diego, CA 92152-5001				10. SPONSOR/MONITOR'S ACRONYM(S)	
				11. SPONSOR/MONITOR'S REPORT NUMBER(S)	
12. DISTRIBUTION/AVAILABILITY STATEMENT Approved for public release.					
13. SUPPLEMENTARY NOTES This is a work of the United States Government and therefore is not copyrighted. This work may be copies and disseminated without restriction.					
14. ABSTRACT This technical report is an accumulation of work performed in 2015 and 2016 under SSC Pacific's Naval Innovative Science and Engineering (NISE) Program. This research on Wireless Power Control has provided key information on power-rate trade-offs, gain matrices, quality-of-service issues, and the performance of various wireless power control algorithms.					
15. SUBJECT TERMS wireless power control algorithms; distributed control; mobile networks; RF propagation; 3-D urban environment; matrix inequalities; time-delay compensation scheme					
16. SECURITY CLASSIFICATION OF:			17. LIMITATION OF ABSTRACT	18. NUMBER OF PAGES	19a. NAME OF RESPONSIBLE PERSON
a. REPORT	b. ABSTRACT	c. THIS PAGE			Sarah Lauff
U	U	U	U	112	19B. TELEPHONE NUMBER (Include area code) (619) 553-3004

INITIAL DISTRIBUTION

84300	Library	(1)
85300	Archive/Stock	(1)
55250	J. C. Allen	(1)
55360	S. Lauff	(1)
55360	D. F. Schwartz	(1)

Defense Technical Information Center
Fort Belvoir, VA 22060-6218 (1)

Approved for public release.



SSC Pacific
San Diego, CA 92152-5001